Modelling additive transport in metal halide lamps

Please check the document version of this publication:

• A submitted manuscript is the version of the article upon submission and before peer-review. There can be important differences between the submitted version and the official published version of record. People interested in the research are advised to contact the author for the final version of the publication, or visit the DOI to the publisher's website.
• The final author version and the galley proof are versions of the publication after peer review.
• The final published version features the final layout of the paper including the volume, issue and page numbers.

Link to publication

Modelling Additive Transport in Metal Halide Lamps

PROEFSCHRIFT

ter verkrijging van de graad van doctor
aan de Technische Universiteit Eindhoven,
op gezag van de Rector Magnificus, prof.dr.ir. C.J. van Duijn,
voor een commissie aangewezen door het College voor Promoties
in het openbaar te verdedigen
op woensdag 2 april 2008 om 16.00 uur

door

Mark Louwrens Beks

geboren te Bellingwedde

Dit proefschrift is goedgekeurd door de promotoren:

prof.dr. J.J.A.M. van der Mullen
en
prof.dr.ir. M. Haverlag

Copromotor:
prof.dr.ir. G.W.M. Kroesen

Summary

In 1912 Charles Steinmetz was granted a patent for a new light source. By adding small amounts of sodium, lithium, rubidium and potassium to a mercury lamp he was able to modify the light output from "an extremely disagreeable colour" to "a soft, brilliant, white light". Much later, at the New York world trade fair in 1964 General Electric was the first to introduced a commercial lamp based on the same principle. The light emitting metallic elements are introduced as components of halide salts. Hence, they are called metal halide lamps.

The physics behind discharge lamps of this type, however, is still a matter of active investigation. One well-known phenomenon is that, when operated vertically, the metal halides in the lamp tend to demix; the concentration of metal halides in the gas phase is much greater at the bottom of the lamp.

Demixing, or segregation as it is also called, has a negative impact on the lamp's efficacy. It is currently avoided by using lamp designs with very small or very large aspect ratios. Gaining more insight into the process of demixing would allow a broader range of lamp designs with still better luminous efficacies.

The demixing is caused by a competition between convection and diffusion. The centre of the lamp must be hot to produce as much light as possible. The walls must stay relatively cool to avoid them weakening and releasing the mercury vapour. Thus, large temperature gradients are present in the lamp, driving convective flows. In the hot centre the molecules are dissociated into atoms. The atoms are smaller and more mobile than the molecules. The atoms are dragged up by the convective currents while diffusing outward. Because of their larger mobility, however, the atoms do not reach the top of the lamp. The result is a larger concentration of metal additives at the walls and at the bottom of the lamp than at the centre and the top of the lamp.

This thesis describes the process of demixing in a self consistent and quantitative manner using state-of-the-art computational methods. The competition between convection and diffusion is studied using a variety of models built with the plasma modelling toolkit Plasimo. Using Plasimo allows for the construction of models in a modular fashion. Partial models are used to study the convec-

tive flow as a result of the temperature gradients, the chemical composition as a function of temperature and pressure, and the radiation transport on the lamp. A grand model is formed by combining modules for ray tracing, elemental diffusion, convective flow and the temperature equation. The model result is validated against experiments done by colleagues: Experiments which have been carried out in Eindhoven, at the Argonne National Laboratories in the USA, and in the International Space Station. Cross validation with theoretical work has also been performed.

Axial demixing is shown to be the result of the competition between axial convection and radial diffusion. This competition is best expressed by the dimensionless Peclet number. When the Peclet number is approximately equal to unity, axial segregation is strongest. The degree of axial segregation is best expressed by the dimensionless segregation depth τ. The largest value of τ depends on the element under study and on the position in the discharge where the molecules dissociate to form ions.

Contents

Chapter 1

Introduction

High Intensity Discharge (HID) lamps are very efficient light sources in widespread use today. They are used when a high luminous flux is required from a compact, point-like, source. Examples are street lighting, greenhouse lighting, automotive headlights and light sources for projection systems. The first HID lamp was created in 1860 by J. T. Way. He enclosed a carbon arc lamp in an atmosphere containing mercury vapour [1]. Many modern HID lamps still contain small amounts of mercury, with the exception of high pressure sodium and xenon lamps.

Lamps with a mercury pressure of several bars are used in street lighting. The high pressure causes self absorption of the resonance radiation. This will suppress the UV radiation of the famous 253.7 nm line corresponding to the $6^3P_1 \rightarrow 6^1S_0$ transition resulting in more radiation in the visible range. At very high pressures bremsstrahlung and molecular radiation from Hg_2 molecules give radiation across a broad spectrum. High pressure mercury lamps containing saturated mercury vapour at a pressure of 200 bar are used in data projection systems, for example [2, page 37-41].

HID mercury lamps operated at lower pressures than the aforementioned 200 bar emit light with a bluish tint. In 1912 Charles Steinmetz was granted a patent [3] for a new light source base. By adding small amounts of sodium, lithium, rubidium and potassium he was able to modify the light output from "an extremely disagreeable colour" to "a soft, brilliant, white light". It was not until much later that a commercially viable lamp was produced along the same principles. General Electric first introduced a commercial Metal Halide (MH) lamp at the New York trade fair in 1964. Modern lamps of this type are

still produced today. The light emitting metallic elements are introduced as components of halide salts. Hence, they are called metal halide lamps. These salts have a higher vapour pressure than the pure metal form. At the wall the metal-halides molecules are present in bound form, limiting corrosion of the walls. The pure metal would attack the quartz or ceramic walls, thereby reducing the lifetime of the lamps. In the centre of the plasma the molecules are dissociated. The atoms are partially ionised. Collisions of free electrons and atoms excite the atoms to higher levels. The subsequent decay gives the desired radiation.

Modern metal halide lamps contain a rich cocktail of metals to produce the desired colour output. The MasterColor® ceramic metal halide lamp produced by Philips, for example, contains sodium, thallium, calcium, dysprosium, holmium, and thulium iodides [4] The CHM-T® lamps produced by GE, contain a similar mixture.

The physics behind discharge lamps of this type is still a matter of active investigation. One well known phenomenon [5, 6, 7] is that, when operated vertically, the metal halides in the lamp tend to demix; the concentration of metal halides in the gas phase is much greater at the bottom of the lamp. This effect is not present under all conditions, and some lamp designs are more severely affected than others. The demixing can be observed directly from the light output; a demixed lamp shows a blue white mercury discharge at the top of the lamp and a much brighter and whiter discharge from the additives at the bottom of the lamp [8]. An example of this is shown in figure 1.1c. Demixing, or segregation as it is also called, has a negative impact on the lamp's efficacy and beam uniformity. It is currently avoided by using lamp designs with very small or very large aspect ratios. Gaining more insight into the process of demixing could possibly allow a broader range of lamp designs with still better luminous efficacies.

1.1 The Cost 529 reference lamp

Commercial MH lamps come in a wide variety of shapes and sizes. To better facilitate the comparison of experiments and models from different researchers a reference lamp has been defined [9]. This lamp is called the cost 529 reference lamp, after the European Union project which led to its development. It has a relatively simple geometry. The inner burner is a straight cylinder 21 mm high and 8 mm in diameter. The electrodes are 18 mm apart. The models in this thesis are all based on the cost lamp. Experiments on lamps of this type have

been performed by Käning et al to study molecular continuum radiation [10]. The atomic line radiation and the atomic state distribution structure has been studied by Nimalasuriya et al [11]. Lamps of this type have also been studied under microgravity conditions in the international space station [12] and under simulated hypergravity in a centrifuge [13] by Nimalasuriya and Flikweert et al. A photograph and a schematic drawing are shown in figure 1.1.
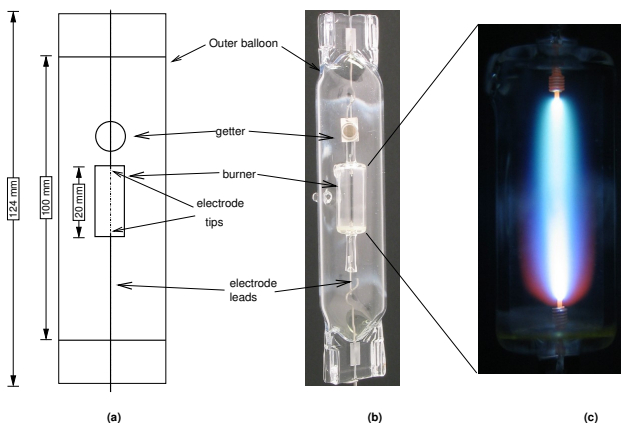
Figure 1.1: a. Reference lamp schematic drawing from the design paper specifications [9]. b. Photo of the lamp turned off. c. Photo of the inner burner with the lamp turned on. Segregation is clearly visible as discharge is fainter and tinted bluish towards the top of the burner. Photos by L. Baede. The purpose of the getter is to remove impurities.

1.2   Segregation

The additives in metal halide lamps are dosed in the form of iodide salts. Under operating conditions these salts melt and form a salt pool in the bottom corner of the lamp. Above the salt pool the additives form a saturated molecular vapour. The molecules spread throughout the lamp from the vapour near the salt pool by diffusion and convection. As they move away from the walls toward the hotter inner regions of the discharge they dissociate to form atoms. These atoms are the prime radiating species and responsible for most of the light

output. As will be shown in this thesis, the uneven distribution of additives in the lamp is determined by the competition between the processes of convection and diffusion. It is useful to differentiate between axial and radial segregation as the former is present only in conjunction with convection, whereas the latter is enhanced in the absence of convection.

1.2.1   Radial segregation

Radial segregation occurs under the influence of diffusion. It is most pronounced in the absence of convection, as shown by experiments in the international space station [12, 14]. In the absence of convection, the flux of molecules towards the centre of the discharge must be equal to the flux of atoms in the opposite direction. The atoms, however, diffuse much more readily through the background gas of mercury atoms than the molecules. In order to maintain the same flux in both directions the gradient in the partial pressure of the molecules must be larger than that of the atoms. The result is that the partial pressure of the atoms at the walls is lower than that of the molecules. The partial pressure of the ions in the very centre of the discharge is even lower than that of the atoms, due to the effect of ambipolar diffusion.

1.2.2   Axial segregation

Axial segregation only occurs in the presence of convection. Convection occurs due to the large temperature gradients in the lamp. These large temperature gradients are present because of design restrictions. The walls must stay cool enough to avoid damage to the walls whilst the centre must be hot enough to partially ionise the additives and excite the radiative species. In practice, this means temperatures of 1200 K to 1500 K for the walls, and 5000 K to 7000 K in the centre. The applications often require small lamps, the Philips CDMR-i 25W ® lamp, for example, has an inner diameter of only 4 mm. The large temperature gradients result in large density gradients. By virtue of the law of Archimedes, the heavy cooler plasma near the walls pushes up the hotter lighter plasma in the centre. By taking the lamps to the international space station the convective flow is stopped and the axial segregation disappears [12, 14]. By placing the lamps in a centrifuge the convective flows are enhanced [13]. Enhancing the convective flows does not necessarily increase the amount of axial segregation. If the convective flows are high enough the lamps become homogeneously mixed. High convective flows reduce both the axial and radial convection.

There is an optimum degree of convection at which axial segregation is most pronounced [5]. Axial segregation also occurs because of the difference in diffusion coefficients between the atoms and molecules. The atoms diffuse outward towards the walls while being dragged up by the background mercury gas. The molecules diffuse towards the centre while being dragged down. The molecules diffuse inward at a slower rate than the atoms diffuse outward. The net result is that the additives are concentrated at the bottom of the lamp and never reach the top of the lamp. If the convective fluxes are of the same magnitude as the diffusive fluxes axial segregation is most pronounced. If the convective fluxes are much smaller in magnitude than the diffusive fluxes only radial segregation is observed. If they are much faster the atoms will not have enough time to diffuse outward while dragged up by the hot mercury atoms in the centre of the discharge and thus the atoms will reach the top of the lamp.

In this thesis it will be shown that the conditions under which axial segregation is most pronounced can be predicted by a simple scaling law. In particular, the Peclet number, when defined as the ratio between axial convection and radial diffusion, is shown to give a accurate prediction of the degree of axial segregation.

In the field of fluid dynamics the ratio of the rate of convection to the rate of diffusion of a quantity is described by the dimensionless Peclet number[15, page 85]. In the case of axial segregation of additives the defining rates are the rates of axial convection and radial diffusion. Typical time scales for convection are L/V_z, with L the length of the inner burner and V_z the axial bulk velocity on the axis halfway between the two electrodes. The typical time scale for radial diffusion is given by R^2/D, with R the inside radius of the inner burner, D the effective diffusion coefficient of the additive. Taking the inverse of the time scales to obtain typical rates and dividing the two yields a Peclet number:

$$Pe = \frac{V_z R^2}{DL}.$$ (1.1)

It is this Peclet number that is indicative of the conditions for axial segregation. In the context of this thesis it is referred to as "*the*" Peclet number.

1.3 Numerical models

The distribution of additives is studied by the use of numerical models built with the modelling platform PLASIMO [16]. The primary objective of these models is to gain understanding of the processes leading to axial and radial segregation.

The focus on the distribution of additives differentiates this work from the work of, for example Flesch[2, chapter 4] or Benilov [17, 18] where the focus lies on plasma electrode interaction.

The additives are spread over the lamp by convection and diffusion. The diffusion coefficients in turn depend on the temperature and on the density of other species. The convection flow depends on the density gradients and the volume forces acting on these density gradients. To calculate the distribution of additives over the lamp one needs to calculate the temperature distribution and the chemical composition of the lamp. To calculate the chemical composition it is assumed that the species present are in local chemical equilibrium. This, together with the assumption that all species may be described with a single temperature, forms the assumption of local thermal equilibrium. The temperature follows from a simple energy balance equation, with electrical power put into the lamp through ohmic dissipation and lost through radiation and the conduction of heat.

The models are formed by a set of coupled differential equations; one for the temperature, one for each element other than mercury, one for the potential distribution and, except in the microgravity simulations, a partial differential equation for each velocity component and the pressure. Additionally, the chemical composition is calculated by a non-linear set of equations and the radiation source term is calculated by the method of ray tracing. The differential equations are discretized using the finite volume method. This method is well suited to conservation equations, and all differential equations in the model are cast in this form. The resulting coupled set of equations are solved with the method of successive substitution starting with an educated guess for the initial conditions. The model is said to have converged if the maximum of the relative difference between two successive solutions for each equation and for each position on the grid is below a threshold value, usually 1×10^{-8}.

The numerical models are used to answer one central question: *Under which circumstances and to what extent do the additives in a model-lamp segregate?* To this end calculations are done for many different conditions. By varying the acceleration, the pressure, the composition and the cold spot vapour pressure the influence of different aspects of the plasma in creating the right conditions for segregation are studied. The results are classified by examining the output. Besides the distribution of additives, this also includes the temperature, the velocity and the density of the radiative species. The following processes will be studied to examine their role in creating the conditions for segregation: convection, diffusion, chemical composition and radiation.

1.4   Thesis outline

In this thesis the process of demixing is studied through numerical modelling. Starting as much as possible from first principles a basic set of equations is derived in chapter 2 to describe the lamp. These equations are discretized on a control volume grid and solved with the plasma modelling toolkit PLASIMO.

Some early results of this model, describing the pressure dependent additive distribution in a lamp containing sodium iodide and mercury are also given in this chapter. In chapter 3 the model is extended to cover the effect of the electrodes protruding into the plasma. In chapters 4 and 5 the model is modified to allow for the modelling of a lamp with dysprosium tri-iodide additive instead of sodium additive. Chapter 4 discusses the changes made to cover the more complex chemistry of the dysprosium tri-iodide containing lamp and also compares results with the earlier sodium containing lamp and a pure mercury lamp. In so doing, the effect of the lamp chemistry on the segregation of additives is studied. This chapter also introduces the Peclet number to compare results with different additives. Chapter 5 discusses the changes made to cover the spectral "grass-fields" of dysprosium atoms and ions and discusses the effect of the choice of data set on the degree of contraction predicted by the model. These changes were necessary to compare with experiments carried out by T. Nimalasuriya [19, 11, 12, 20, 21] and A. J. Flikweert [22, 13]. This chapter also focuses on the effect of radiation on the other properties of the discharge. Chapters 6 and 7, compare the results of the model with dysprosium additives with experiments carried out in the international space station (chapter 6) and in a centrifuge (chapter 7). Finally, in chapter 8 simple analytical expressions are derived to allow predictions to be made without the complicated numerical models which predominate in most of this thesis. In the final chapter general conclusions are drawn based on the conclusions at the end of each chapter.

Chapter 2

Theoretical framework

Abstract. Convection and diffusion in the discharge region of a metal halide lamp are studied using a computer model built with the plasma modelling package Plasimo. A model-lamp containing mercury and sodium iodide is studied. The effect of the total lamp pressure on the degree of segregation of the light emitting species is examined and compared to a simpler model with a fixed temperature profile. Significant differences are observed, justifying the use of the more complete approach.

This chapter is based on the publication: *"Demixing in a metal halide lamp, results from modelling", M L Beks, A Hartgers and J J A M van der Mullen in J. Phys. D: Appl. Phys. 39 4407-4416.* This publication's primary focus is on the underlying theory. Additionally, results are also given for a lamp filled with a mixture of sodium iodide and mercury. An appendix has been added to discuss underlying assumptions in the model which were left under-examined in the original publication.

2.1 Introduction

Metal Halide (MH) lamps are small high pressure discharge devices providing high luminous output across a broad spectrum of the visible range. They typically consist of an inner burner the size of a cigarette filter, surrounded by a larger protective outer wall. The inner burner is made from polycrystalline alumina or quartz and is filled with noble gasses, mercury (about 10 mg) and salt additives (several mg). Under operating conditions the mercury in the inner burner evaporates raising the pressure to several tens of bars. The salt additives, such as sodium, scandium and dysprosium iodide, are present in very low concentrations in the gas phase, yet it is these minority species that provide most of the light output. To gain a better understanding of the physics of these lamps one needs, therefore, to consider the lamp chemistry and the transport of the minority species throughout the discharge.

Commercially viable MH lamps were first demonstrated in 1963 [23]. A drawing of a lamp from the patent GE filed in 1961 is given in figure 2.1. A review on metal halide development is given by Sugiara [24]. The physics of discharge lamps is discussed in a more recent review by Lister et al [25].

A well known [5, 6, 7] phenomenon in MH lamps is that, when operated vertically, the metal halides in the lamp tend to demix; the concentration of metal halides in the gas phase is much greater at the bottom of the lamp. This effect is not present under all conditions, and some lamp designs are more severely affected than others. The demixing can be observed directly from the light output; a demixed lamp shows a blue white mercury discharge at the top of the lamp and a much brighter and whiter discharge from the additives at the bottom of the lamp [8]. Demixing, or axial segregation as it is also called, has a negative impact on the lamp's efficacy.

Demixing is the result of a competition between convection and diffusion [5]. One may manipulate the convection by means of controlling the lamp pressure, lamp geometry, or the gravity conditions under which the lamp is operated. The operating pressure may be increased by increasing the amount of mercury in the lamp, changing the gravity conditions was done by taking the lamp on parabolic flights [22], and in the international space station [12].

We seek to examine demixing in the lamp through the use of a computer model of the discharge in the inner burner of an MH lamp. In particular, we wish to examine the competition between convection and diffusion by adjusting the total lamp pressure. Increasing the lamp pressure will increase the convection speed and effect the convection pattern, as will be shown by our model.
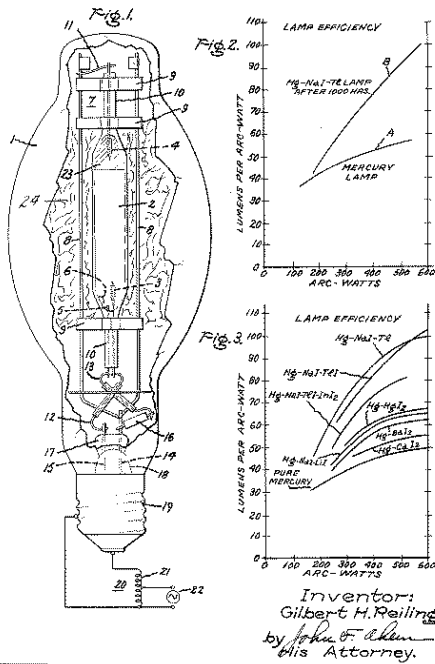
Figure 2.1: 1966 patent on the Metal Halide lamp

.

2.2   The segregation curve

In 1975 Fischer [5] proposed a model based on the interaction between diffusive
and convective fluxes to give a quantitative description of the axial segregation
in the lamp. Fischer examined the limiting cases of zero and infinite convection
velocity and came to the conclusion that, in both cases, the segregation vanishes.
The segregation is at a maximum when radial diffusive fluxes are equal to the

axial convective fluxes. The segregation parameter $\bar{\lambda}$ [1]

$$\bar{\lambda} = \frac{1}{p_0}\frac{dp}{dz} \qquad\qquad (2.1)$$

as a function of the total lamp pressure is minimal at low pressures, highest at intermediate pressures and decreases again at high pressures. A simple model based on an assumed parabolic temperature profile and long aspect ratios was published in [5]. More advanced models have since been made [7, 26].

We seek to build a numerical model that uses less assumptions on the nature of the discharge, calculating more of the lamp properties from first principals than earlier models. This model should calculate all essential properties self consistently. This involves, amongst others, calculating the convection and diffusion of species throughout the discharge region, calculating the emission and absorption of light, and accurately describing the energy balance in the lamp. To build this model we have at our disposal the plasma simulation package Plasimo [27, 28] developed at the Eindhoven University of Technology by a succession of graduate students and researchers over the past 15 years.

2.3   Theory

The question of demixing is basically one of particle transport. What is the concentration of each species at each position in the lamp? MH lamps contain a complex mixture of ions, atoms and molecules. The discharge can be regarded as a multi-fluid mixture. Each fluid of this multi-fluid mixture is described by the well known Boltzmann Transport Equation (BTE).

$$\frac{\partial f_i(\vec{x},\vec{v})}{\partial t} + \vec{v}_i \cdot \nabla f_i(\vec{x},\vec{v}) + \vec{F}_i/m_i \cdot \nabla_v f_i(\vec{x},\vec{v}) = \left(\frac{\partial f_i(\vec{x},\vec{v})}{\partial t}\right)_{coll}, \qquad (2.2)$$

with $f_i(\vec{x},\vec{v})$ the density of species i with velocity $\vec{v}$ at position $\vec{x}$. The density is defined such that the number of particles of type i in a volume element $d^3x d^3v$ in phase space centred around the point $(\vec{x},\vec{v})$ is given by $f_i(\vec{x},\vec{v})d^3x d^3v$. The right hand term $\left(\frac{\partial f_i(\vec{x},\vec{v})}{\partial t}\right)_{coll}$ is a source term for interactions with all other species. In this context a species is an electron, or a particular state of a molecule, atom

---

[1]In later chapters, the dimensionless quantity τ is introduced to characterise the degree of segregation.
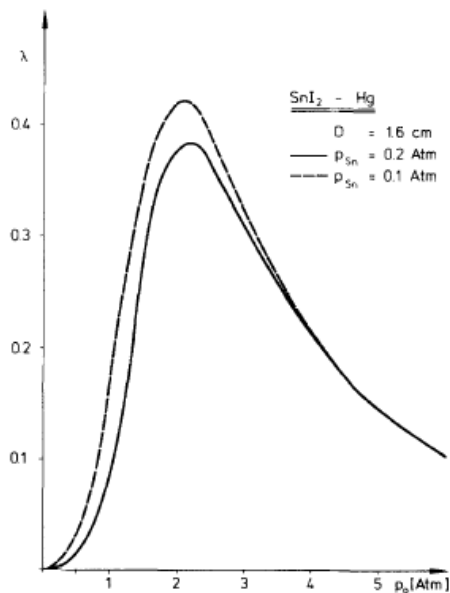
FIG. 5. Pressure dependence of the segregation parameter
in an Sn-I-Hg plasma.

Figure 2.2: The segregation curve from Fischer's 1975 article [5] showing the segregation parameter as defined by (2.1) as a function of the total lamp pressure. Note that Fischer uses λ for the segregation parameter.

or ion. In principle, each excited state of each molecule needs to be treated as a separate species.

The notation ∇_v is used for the derivatives of f with respect to the velocity. Volumetric external forces are represented by $\vec{F}$. In principle, (2.2) together with Maxwell's equations for the elector-magnetic fields and a modified form of (2.2) for photons, forms a complete description of the plasma. In practice, a great number of simplifications are possible.

In the collision term in equation (2.2) great complexity is hidden. Collisions are assumed to be instantaneous, hence collisions cause particles to be instantaneously transported to remote parts of phase space. One usually separates

collisions into elastic and inelastic processes. See the classical texts [29] for a discussion on the elastic collision term and [30] for the general formulation of the inelastic collision term.

For the purpose of examining transport processes in MH lamps a description in terms of quantities averaged over velocity space suffices. Additionally, we do not need to treat all species independently. Many species are short lived. It will be shown that we may infer the local density of species from the local elemental composition and temperature.

We examine the first three velocity moments of the distribution function:

The particle density

$$n_i(\vec{r}, t) = \int f_i d\vec{v},$$

particle flux

$$\vec{\Gamma}_i(\vec{r}, t) = n_i \vec{u}_i = \int f_i \vec{v} d\vec{v}$$

and the internal energy density

$$\frac{3}{2} k_B n_i T_i(\vec{r}, t) = \frac{1}{2} m_i \int (\vec{v} - \vec{u}_i)^2 f_i d\vec{v}.$$

Integrating (2.2) over velocity space one obtains the continuity equation:

$$\frac{\partial n_i}{\partial t} + \nabla \cdot \vec{\Gamma}_i = S_i, \tag{2.3}$$

with S_i a source term from all inelastic collisions.

Integrating (2.2) multiplied with the velocity results in the force balance:

$$\frac{\partial}{\partial t}(\rho_i \vec{u}_i) + \nabla \cdot (\rho_i \vec{u}_i \vec{u}_i) = -\nabla \cdot \mathbf{P}_i + n_i \vec{F}_i + \sum_j \vec{R}_{ij} + S_i^m, \tag{2.4}$$

with ρ_i the mass density $m_i n_i$, S_i^m a momentum source term from inelastic collisions, $\vec{R}_{ij}$ the friction force from other particle fluxes:

$$\vec{R}_{ij} = \int m_i \vec{u}_i \left(\frac{\partial f_i}{\partial t}\right)_{coll}^j d\vec{v}_i$$

and $\mathbf{P}_i$ the pressure tensor

$$\mathbf{P}_i = \rho_i \langle (\vec{v} - \vec{u}_i)(\vec{v} - \vec{u}_i) \rangle.$$

Likewise, multiplication with the square of the velocity and integration yields the energy balance equation:

$$\frac{\partial \rho_i e_i}{\partial t} + \frac{1}{2}\frac{\partial \rho_i u_i^2}{\partial t} + \nabla \cdot (\rho_i e_i \vec{u}_i) + \frac{1}{2}\nabla \cdot \left(\rho_i u_i^2 \vec{u}_i\right) + (\nabla \vec{u}_i) : \mathbf{P}_i + \nabla \cdot \vec{q}_i - n_i \vec{F}_i \cdot \vec{u}_i = S^E,$$
(2.5)

with e_i the thermal energy per unit mass, $\vec{q}$ the heat flux and S^E the source term from of all inelastic collisions. This source term contains ionisation, excitation and, in the case of charged particles, Ohmic dissipation.

The resulting equations from the expansion in terms of the velocity moments cannot be solved because the equations are coupled and each equation depends on the next moment. In order to solve the system we truncate it with the energy equation and assume a Maxwellian energy distribution function. Equations (2.3), (2.4) and (2.5) can be further developed by looking at particle transport in MH lamps on three different levels:

1. plasma component species,

2. elemental fluxes and

3. bulk flow.

We will use the moments of the BTE as building blocks to describe transport on each of these levels. As will be shown shortly, different approximations and approaches may be used for each level. We will follow the approach in [31] and [32]. An overview is given in table 2.1.

2.3.1 Particle Balance

On the species level, the continuity equation is given by (2.3). Elements are neither created nor destroyed in a low temperature plasma. We introduce the concept of elemental densities n_α to make use of this property. The elemental density is defined as the abundance of a particular element regardless of its state. Thus the density of a particular element is given by the density of the species multiplied with the number of atoms of the element in each species.

In general, we will use Greek subscripts for elements and Latin subscripts for species. To distinguish the elemental density of a specific element from the density of free atoms we will use braces. The elemental density of hydrogen in water, for example, is given by:

$$n_{\{H\}} = 2n_{H_2O} + n_{OH^-} + 2n_{H_2} + n_H + 2n_{H_2O_2} + \cdots$$

In general the elemental density is given by:

$$n_\alpha = R_{i\alpha} n_i,$$

with $R_{i\alpha}$ the stoichiometric coefficient of element α and species i.

The elemental fluxes Γ_α, are similarly defined in terms of the species fluxes:

$$\vec{\Gamma}_\alpha = \sum_i R_{i\alpha} n_i \vec{u}_i. \tag{2.6}$$

Since elements are neither created nor destroyed, the continuity equation for elements is sourceless:

$$\nabla \cdot \Gamma_\alpha = 0.$$

Similarly, for the bulk density $\rho = \sum_i \rho_i$ we have,

$$\nabla \cdot \rho \vec{u} = 0,$$

where the bulk velocity has been defined as

$$\vec{u} = \rho^{-1} \sum_i \rho_i \vec{u}_i,$$

and the average density ρ as $\rho = \sum_i \rho_i$.

2.3.2 Force Balance

The large temperature gradients in the plasma give rise to large density gradients. Together with gravitational forces, these density gradients result in convection on the bulk level. Additionally, dissociation and ionisation result in strong gradients on the species level. Separate force balances will be derived for each level, starting with the species level, then proceeding to the element level, and finally returning to the bulk flow. As we seek a quasi steady state solution the time derivative will be ignored.

Species

We now return to equation (2.4). On the species level the dominating force is the friction with other species, and, in the case of charged particles, the force exerted by the electric field. These forces are balanced by the partial pressure gradient. Viscous and gravitational forces may be disregarded. This in contrast to the bulk flow, where the electric and friction forces cancel out. The electric

force due to quasi-neutrality and the friction forces due to Newton's Third Law. This leaves gravitational and viscous forces as dominating forces.

We further approximate the friction forces by disregarding thermophoretic forces and assuming a dominant background species, so that

$$\sum_j \vec{R}_{ij} \approx \frac{p_i}{D_i} \left(\vec{u} - \vec{u}_i \right),$$

with D_i an effective diffusion coefficient.

We define the deviation from the bulk velocity as

$$\vec{u}_i' = \vec{u}_i - \vec{u} \tag{2.7}$$

.

With use of the continuity equation, and some rearranging we obtain:

$$\left(\rho_i \vec{u}_i \cdot \nabla \right) \vec{u}_i = -\nabla p_i + \frac{\rho_i}{M_i} \vec{F}_i + \frac{p_i}{D_i} \left(\vec{u} - \vec{u}_i \right).$$

We use the ideal gas law and neglect the inertial term to obtain:

$$\vec{u} - \vec{u}_i = -D_i \frac{\nabla p_i}{p_i} + \frac{D_i q_i}{kT} \vec{E}. \tag{2.8}$$

The electric field in the lamp is the result of an externally applied field and the ambipolar field generated by charged species in the plasma. Using the current density $\vec{j} = \sum_i n_i q_i \vec{u}_i$ and equation (2.8)

$$\vec{j} = -\sum_i \mu_i \nabla p_i + \sigma \vec{E},$$

with $\mu_i = \frac{D_i q_i}{kT}$ the mobility, and σ the electrical conductivity $\sigma = \sum_i \mu_i n_i q_i$. To describe the electric field generated by the charged particles in the plasma we introduce the ambipolar field $\sigma \vec{E}_{amb} = \sum_i \mu_i \nabla p_i$. Under the assumption that the conductivity is determined by the electrons. Substitution into (2.8) results in

$$\vec{u}_i - \vec{u} = D_i \left(\frac{-\nabla p_i}{p_i} + \frac{q_i \nabla p_e}{q_e p_e} + \frac{q_i \vec{j}}{\sigma kT} \right). \tag{2.9}$$

2.3.3   Elemental Diffusion

If local thermal equilibrium (LTE) in the discharge may be assumed, the problem of particle diffusion may be greatly simplified. The assumption of LTE in the plasma yields a particle density which is dependent only on the local temperature, pressure and elemental composition. Therefore, one need only solve transport equations for the elemental composition, instead of solving the transport for each component species. This greatly reduces the number of differential equations that need to be solved.

Essentially, we will treat the transport of elements by examining the flux of components species in each cell and their contribution to the net flux of elements. We then retrieve information on the local concentrations of component species by calculating the local equilibrium composition. We define the elemental partial pressure p_α as

$$p_\alpha = n_\alpha kT$$

Substitution of equation (2.9) and rearranging the terms results in:

$$\vec{\Gamma}_\alpha = \quad \frac{p_\alpha}{kT}\vec{u} - \sum_i R_{i\alpha}\frac{D_i}{kT}\left(\frac{p_i}{p_\alpha}\nabla p_\alpha + p_\alpha\nabla\left(\frac{p_i}{p_\alpha}\right)\right)$$

$$+ \sum_i R_{i\alpha}\frac{\mu_i}{\sigma}\frac{p_i}{kT}\cdot\sum_j \mu_j\left(\frac{p_j}{p_\alpha}\nabla p_\alpha + p_\alpha\nabla\left(\frac{p_j}{p_\alpha}\right)\right). \tag{2.10}$$

A complete derivation may be found in [32].

We introduce the elemental mobility

$$\mu_\alpha = \frac{\sum_i R_{i\alpha}\mu_i p_i}{p_\alpha}, \tag{2.11}$$

and define an elemental pseudo diffusion coefficient

$$D_\alpha = \frac{\sum_i R_{i\alpha}D_i p_i}{p_\alpha} - \mu_\alpha\frac{\sum_i \mu_i p_i}{\sigma} \tag{2.12}$$

and a pseudo convective velocity

$$\vec{c}_\alpha = \vec{u} + \frac{\mu_\alpha p_\alpha}{\sigma}\sum_i \mu_i\nabla\left(\frac{p_i}{p_\alpha}\right) - \sum_i R_{i\alpha}D_i\nabla\left(\frac{p_i}{p_\alpha}\right). \tag{2.13}$$

Using these definitions, it is possible to express the elemental flux as given by equation ((2.6)) as a conservation equation equation for the elemental pressure:

$$\nabla\cdot\vec{\Gamma}_\alpha = \nabla\cdot\left(\frac{D_\alpha}{kT}\nabla p_\alpha + \frac{p_\alpha}{kT}\vec{c}_\alpha\right) = 0. \tag{2.14}$$

Bulk flow

The bulk flow follows from substituting (2.4) into the definition of the bulk flow in equation (2.7). The result is:

$$\frac{\partial}{\partial t}\left(\rho\vec{u}\right) + \sum_i \nabla \cdot \rho_i \left(\vec{u}'_i \vec{u}'_i + 2\vec{u}'_i \vec{u} + \vec{u}\vec{u}\right) = \sum_i \left(-\nabla \cdot \mathbf{P}_i + \frac{\rho_i}{m_i}\vec{F}_i\right)$$

After some rearranging one may obtain the Navier Stokes equation:

$$\frac{\partial}{\partial t}\left(\rho\vec{u}\right) + \nabla \cdot (\rho\vec{u}\vec{u}) = -\nabla \cdot \mathbf{P} + \sum_i \frac{\rho_i}{m_i}\vec{F}_i, \tag{2.15}$$

with $\mathbf{P}$ the pressure tensor $\sum_i \left(\mathbf{P}_i + \rho_i \vec{u}'_i \vec{u}'_i\right)$. As stated before, all forces other than gravity on the right hand side of (2.15) cancel out.

The pressure tensor may be split into a scalar pressure multiplied with the unity tensor and a viscosity tensor. We follow the approach found in numerous textbooks, see for example [33, p. 183]. The pressure p is defined as

$$p = \frac{1}{3}\sum_i \rho_i \left\langle (\vec{v}_i - \vec{u}_i)^2 \right\rangle. \tag{2.16}$$

The viscosity tensor $\mathbf{\Pi}$ follows from the relation

$$\mathbf{\Pi} = \mathbf{P} - p\mathbf{I}, \tag{2.17}$$

with $\mathbf{I}$ the unity tensor. In the case of a Newtonian fluid $\mathbf{\Pi}$ is related to the dynamic viscosity μ by :

$$\Pi_{jk} = \mu(\Gamma_{jk} - \frac{2}{3}(\nabla \cdot \vec{u})\delta_{jk}) \tag{2.18}$$

$$\Gamma_{kj} = (\frac{\partial u_j}{\partial x_k} + \frac{\partial u_k}{\partial x_j}), \tag{2.19}$$

with the subscripts j and k denoting the tensor and vector components. In the case of an incompressible flow (2.15) can be further simplified to

$$\frac{\partial}{\partial t}\left(\rho\vec{u}\right) + \nabla \cdot (\rho\vec{u}\vec{u}) = -\nabla p + \nabla \cdot (\mu\nabla\vec{u}) + \sum_i \frac{\rho_i}{m_i}\vec{F}_i. \tag{2.20}$$

2.3.4   Energy Balance

In principle, one could derive energy balances for species, elements and the bulk separately as in the previous sections. However, frequent collisions between particles in a high pressure plasma ensure that all heavy species have the same temperature. The only species that could possibly need to be described by a separate temperature are the electrons. We now give a simple order-of-magnitude estimation of the possible deviation between the electron and heavy particle temperature.

Local Thermal Equilibrium

Metal halide lamps are typically operated at high pressure. Under operating conditions the atomic mercury density is on the order of $10^{25}\mathrm{m}^{-3}$ and the electron electron density reaches $10^{22}\mathrm{m}^{-3}$ in the centre of the discharge. The cross section for elastic momentum transfer between electrons and mercury is on the order of $10^{-19}\mathrm{m}^2$. The resulting collision frequency ν_{eh} is $10^{12}\mathrm{s}^{-1}$. From Mitchner and Kruger[33]. The power density required to sustain a difference between the electron and heavy particle temperature of ΔT is given by:

$$P = 2n_e(m_e/m_h)\nu_{eh}(3/2)k\Delta T. \tag{2.21}$$

Estimating the power density to be $10^8\mathrm{W\,m}^{-3}$ one arrives at an estimate $\Delta T \approx 100\ K$. Additional processes serve only to further limit the maximum sustainable temperature difference. Thus, we may conclude that an LTE approach is justified and we need only consider one temperature balance for all species.

2.3.5   Temperature Balance

In the LTE approach all species have the same temperature. Summation of (2.5) and subtraction of the force balance results in [33]

$$\frac{\partial \rho e}{\partial t} + \vec{u}\nabla\left(\rho e\vec{u}\right)\left(\rho e + p\right)\nabla \cdot \vec{u} = -\nabla \cdot \vec{q} + \mathbf{P} : \nabla\vec{u} + \vec{J}\cdot\vec{E} - Q_{rad}, \tag{2.22}$$

with Q_{rad} the net radiated power and $\vec{q}$ the total heat flux. The summation is over all species in the plasma. This includes excited states of atoms and ro-vibrationally excited states of molecules.

   Equation (2.22) may be rewritten in terms of the temperature by subtracting the mass conservation equation multiplied by $\frac{1}{2}\rho v^2$ and using the ideal gas law.

Table 2.1: Overview of the conservation equations on the three different levels of species, elements and bulk.

balance	species	element	bulk
density	chemical equilibrium	$\nabla \cdot \Gamma = 0$ (2.14)	$\nabla \cdot \rho v = 0$
momentum	-	drift diffusion equation	Navier Stokes (2.15)
energy	-	-	temperature balance (2.23)

The result is:

$$\nabla \cdot (c_V \vec{u} \nabla T) + \mathbf{P} : \nabla \vec{u} + \nabla \cdot \vec{q} + p \cdot \nabla \vec{u} = \sigma E^2 - Q_{rad}, \qquad (2.23)$$

with c_V the volumetric heat capacity. The heat capacity is given by summation of the internal energy per species over all species in the plasma $c_V = \sum_i n_i E_i / T$.

Obtaining the equation for the heat flux from the BTE would require an additional moment. Instead, we close the system of equations by describing the heat flux as

$$\vec{q} = -\lambda_i \nabla T + \sum_i \rho_i \vec{u}_i h_i,$$

with h_i the enthalpy of species i.

To summarise, we may now form a complete description of the discharge region by solving force balance equations (2.14) and (2.15) on, respectively the elemental and bulk levels, together with the energy balance (2.23). From the resulting temperature and elemental pressures the species densities may be obtained by assuming local chemical equilibrium. Thus, the number of coupled differential equations is greatly reduced. An overview of the equations that need to be solved in our model is also given in table 2.1.

2.4 Model Description

We build our model using the plasma simulation platform Plasimo. Plasimo uses a finite volume method to discretise partial differential equations. Such methods are well suited to conservation equations. One of the basic building blocks in Plasimo is the generalised conservation equation or Φ equation in the form

$$\nabla \cdot (f_\phi \rho \vec{u} \phi) - \nabla \cdot (\lambda_\phi \nabla \phi) = S_\phi, \qquad (2.24)$$

with f_ϕ a convection coefficient, λ_ϕ a diffusion coefficient and S_ϕ the source term for the conserved quantity ϕ.

We solve the conservation equations (2.14) , (2.15) and (2.23) cast into the form of (2.24) on a two dimensional cylindrical grid. Plasimo allows one to build many different models depending on the modules selected. We describe the choices made for the transport coefficients and energy source terms.

2.4.1 Transport coefficients

For the electrical conductivity we use [33]

$$\sigma_e = \frac{n_e e^2}{m_e \bar{\nu}_{eh}},$$

with $\bar{\nu}_{eh}$ the average momentum transfer collision frequency for electrons colliding with heavy particles.

The diffusion coefficient is calculated from the binary diffusion coefficients D_{ij}

$$D_i = \left(\sum_{j \neq i} (p_i/p) / D_{ij} \right)^{-1}. \tag{2.25}$$

The binary diffusion coefficients, in turn, are given by [30] (page 486)

$$D_{ij} = \frac{3}{16} \frac{(kT)^2}{p m_{ij} \Omega_{ij}^{(1,1)}}, \tag{2.26}$$

with m_{ij} the reduced mass of the system of the two interacting particles (i, j) and $\Omega_{ij}^{(1,1)}$ the corresponding binary collision integral. The definition of the collision integrals is also given in [30] on page 482. We use the Langevin polarisability model for collisions between charged and neutral species, shielded Coulomb interactions for collisions between charged particles and the hard sphere model for collisions between neutral particles. See also [34, chapter 9] for the description of the use of collision integrals in Plasimo.

The thermal conductivity is the result of energy transport by the particles and enthalpy transport by reactions in the plasma. These are commonly referred to as, respectively the frozen and reactive contributions.

$$\lambda = \lambda_f + \lambda_r. \tag{2.27}$$

The frozen contribution is given by [33]

$$\lambda_f = \sum_i \left(\frac{n_s}{\sum_j n_j M_{ij}} \right) \lambda_i, \tag{2.28}$$

where M_{ij} is related to the reduced mass of the species m_{ij} and their energy averaged cross sections σ_{ij} by:

$$M_{ij} = \left(\frac{2m_{ij}}{m_i} \right) \frac{\sigma_{ij}}{\sigma_{ii}}.$$

The term λ_i represents the thermal conductivity for the pure gas. The reactive contribution is given by the approach of Butler and Brokaw[35].

2.4.2 Lamp Chemistry

We calculate local species densities by assuming local chemical equilibrium. This is done by solving a system of particle balances and constraints. A full description is found in [31, chapter 2].

2.4.3 Temperature source terms

The Ohmic dissipation in the plasma is calculated by assuming that the electric field has a component in the axial direction only. The current through the plasma is fixed at 0.8 Ampere.

Ray tracing is used to calculate the energy emitted and absorbed by radiation at a number of discrete points in the plasma. For a complete description see [31]. We make use of the cylindrical symmetry to reduce the complexity of the problem.

2.4.4 Solution procedure

The non-linear equations are solved by successive substitution using under-relaxation. The order of the solution procedure is as follows:

1. Calculate the Ohmic dissipation,

2. Update bulk flow using the SIMPLER algorithm,

3. Calculate elemental diffusion coefficients and pseudo-convection vectors,

4. Update the elemental density.

5. Calculate the species densities,

6. Calculate the net radiated power Q_{rad} in equation (2.23),

7. Calculate other source terms and coefficients in (2.23),

8. Update the temperature.

The solution is considered converged if the residue is below 10^{-8}, where the residue ξ is defined as

$$\xi = max_{i,j,N} \left| \frac{\Delta\Phi_{i,j}^N}{\Phi_{i,j}^N} \right|, \tag{2.29}$$

with $\Phi_{i,j}^N$ the solution of equation N at grid point (i,j).

2.4.5   Geometry and grid

We construct a model of a lamp using a straight cylinder with flat ends measuring 20 mm in length and 8 mm in diameter. The diameter is identical to that of the COST-529 reference lamp [9]. The length is chosen to be the distance between the electrodes of that same lamp. We use a structured two dimensional cylindrically symmetric grid and the finite volume method to discretise all equations. The grid has 34 grid lines in the axial direction and 18 lines in the radial direction. The grid cells are more closely spaced near the walls to accommodate the high temperature gradients there. A cold spot is defined to be on the lower 4 mm of the cylinder wall. Electrode regions 2 mm in diameter are defined on the cylinder ends (see figure (2.3)).

2.4.6   Boundary conditions

The temperature equation 2.23 is solved with homogeneous Neumann conditions on the axis and Dirichlet conditions on the wall. The wall is held to 1500 K everywhere except for the cold spot where it is held at 1200 K and the electrode regions, where a temperature of 2900 K is imposed. For the elemental pressure we impose the condition that the flux through the wall is zero, with the exception of the cold spot where the pressure is fixed at 1016 Pa. For the velocity we impose no-slip conditions on the walls. The radial velocity through the axis is zero for reasons of symmetry. Similarly, a homogeneous Neumann condition is imposed on the axis for the axial velocity.
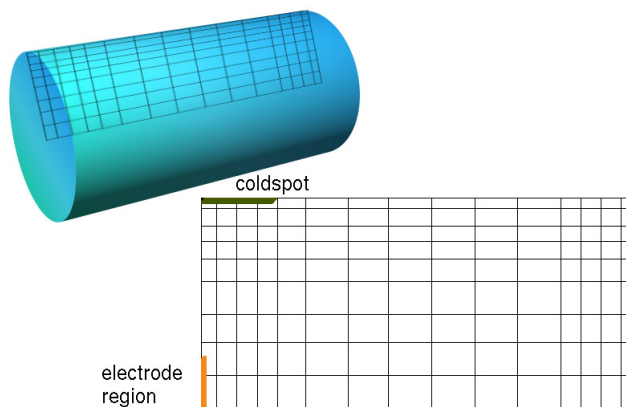
Figure 2.3: Schematic view of the grid and geometry used in the model. The actual model is not as coarse as the depicted grid with 34 axial and 18 radial positions.

2.5 Results

We ran the model with a number of pressures ranging from 9 to 40 bar. The model output consists among others, of the elemental pressures, the temperature and the bulk velocity. An example of the elemental pressure distribution is shown in figure 2.4.

As a measure for segregation we looked at the elemental pressure along the axis. This was fitted to an exponential decay with a least squares approach. The fit function is

$$p_\alpha(z) = p_0 e^{-\bar{\lambda}z}. \tag{2.30}$$

The fit parameter $\bar{\lambda}$ is the average segregation along the axis and is taken to represent the segregation in the entire lamp. The model results do not, of course, fit equation (2.30) exactly. It is used to quantitatively compare results for different pressures. An example illustrating this procedure is shown in figure 2.5.

We compared the results thus obtained with a model based on the model by Fischer [5]. That is, we constructed a model with the same underlying assumptions as [5], with the geometry of the more advanced model. For the temperature a parabolic profile is used with a maximum of 5800 K and a wall
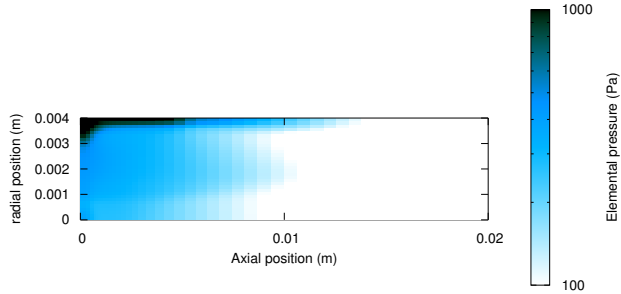
Figure 2.4: The elemental pressure of sodium at a total lamp pressure of 14 bar. The pressure is greatest at the cold spot, where a pressure of 1016 Pa is imposed, and falls of rapidly in radial and axial directions. Note that the axial direction is along the abscissa.

temperature of 1000 K. Furthermore, equation (2.14) is also solved, with the same boundary conditions as the more advanced model. The result of this comparison is shown in figure 2.6.

The results from the more advanced model are strikingly similar to the model with the fixed temperature profile, considering the differences between them. The maximum segregation is reached at a slightly larger pressure with the advanced model and the segregation recedes less quickly in the advanced model though. These difference are significant, however, justifying the additional computational expense of the more advanced model.

2.5.1   Axial velocity

We now return to the results of the more advanced model to study the convective flow. One of the driving forces behind the segregation is the bulk flow. The bulk flow exhibits a typical convective cell as show in figure 2.7. To get a picture of the magnitude of the velocity we present the axial velocity along the axis for several pressures in figure 2.8. From these results it is clear that while the velocity continues to increase with increasing pressures the relationship is not linear, the increase saturates at higher pressures.

The location where the convection speeds are greatest also moves from the
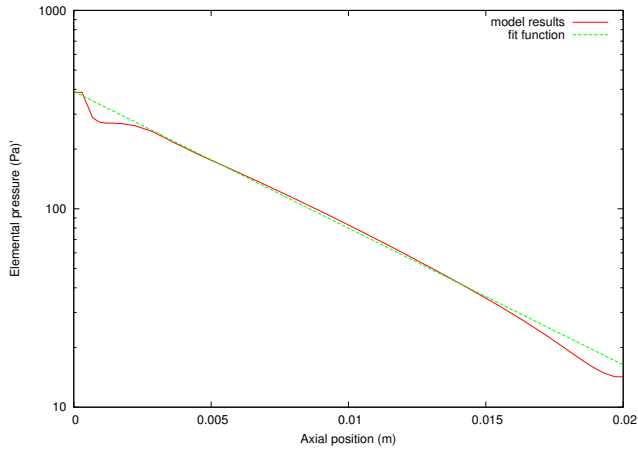
Figure 2.5: The elemental pressure at 14 bar along the axis of the discharge. Also shown is a fit to a constant segregation parameter as defined by (2.30), in the axial direction, used to calculate the average segregation.
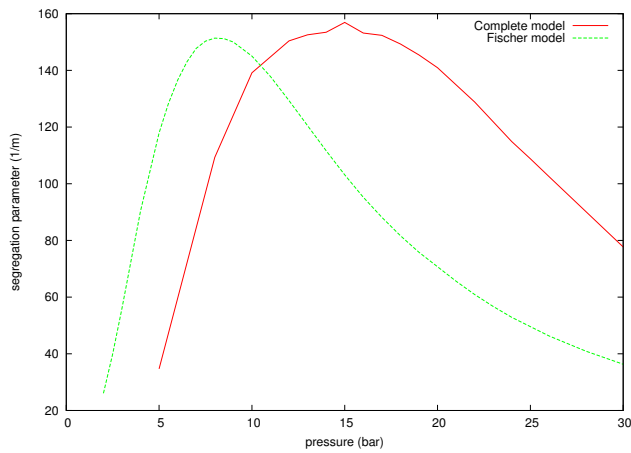
Figure 2.6: Segregation parameters for different pressures for both the Fischer model and the more advanced model.
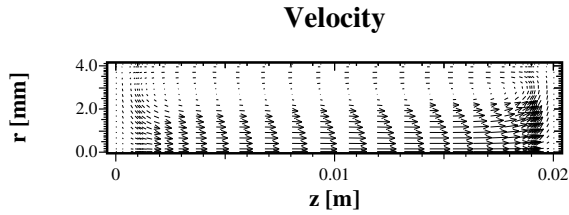
Velocity

Figure 2.7: Convective flow in the lamp at a total pressure of 20 bar. Note that the axial direction is along the abscissa, with gravity toward the left of the figure.
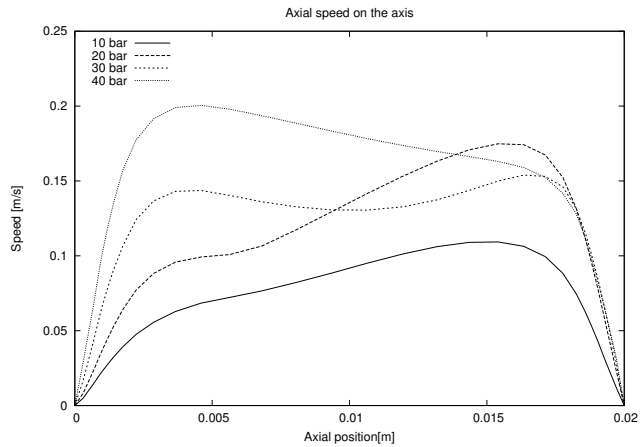
Figure 2.8: The velocity in the axial direction, on the axis of the discharge. The velocity first increases with increasing pressure but reaches a saturation point for higher pressures. Also noticeable is the change in the shape of the profile.

top of the lamp at low pressures to the bottom of the lamp at high pressures.

2.5.2 Temperature

The bulk flow is driven by the temperature gradients in the lamp. This is to be expected as the denser plasma descents, pushing hotter plasma along the axis up against the top of the lamp. Figure 2.9 shows the temperature for three different pressures. In general, the top of the lamp is hotter than the bottom, as can be expected as a result of convection in the lamp. Additionally, the centre of the arc is somewhat cooler lower down in the arc, while the maximum temperature is constant. The arc is also more constricted near the top electrode, as is show in figure 2.10. At higher pressures this difference is more pronounced. Increasing the lamp pressure decreases the arc constriction, as can be seen in figure 2.11. This may be expected as increasing the pressure increases the heat transported to the walls by convection, thus flattening the temperature profiles.

2.5.3 Diffusion

Segregation in the lamp is also driven by radial diffusion. Figure 2.12 shows the total elemental diffusive flux for sodium near the wall in the direction of the wall for different pressures. From this figure it becomes clear that the diffusive flux decreases for increasing pressure, thereby also contributing to decreased segregation at higher pressures.

2.6 Conclusion

A model has been built of the arc discharge in a vertically burning metal halide lamp. The model can be used for parameter studies to study discharge characteristics such as the temperature, convection speed and transport of light producing species in the lamp. A study has been made on the influence of the total lamp pressure on the degree of segregation of sodium. Results from this numerical experiment are along the lines of earlier work [5].

Comparison of model results with experimental results is needed to further verify the model. To this end, a model using Dysprosium Iodide (DyI_3) is needed. Additionally, metal halide lamps typically have electrodes protruding into the discharge region. The model will be expanded to include the effects of these protruding electrodes on the discharge region.

(a) 10 bar

(b) 20 bar

(c) 30 bar
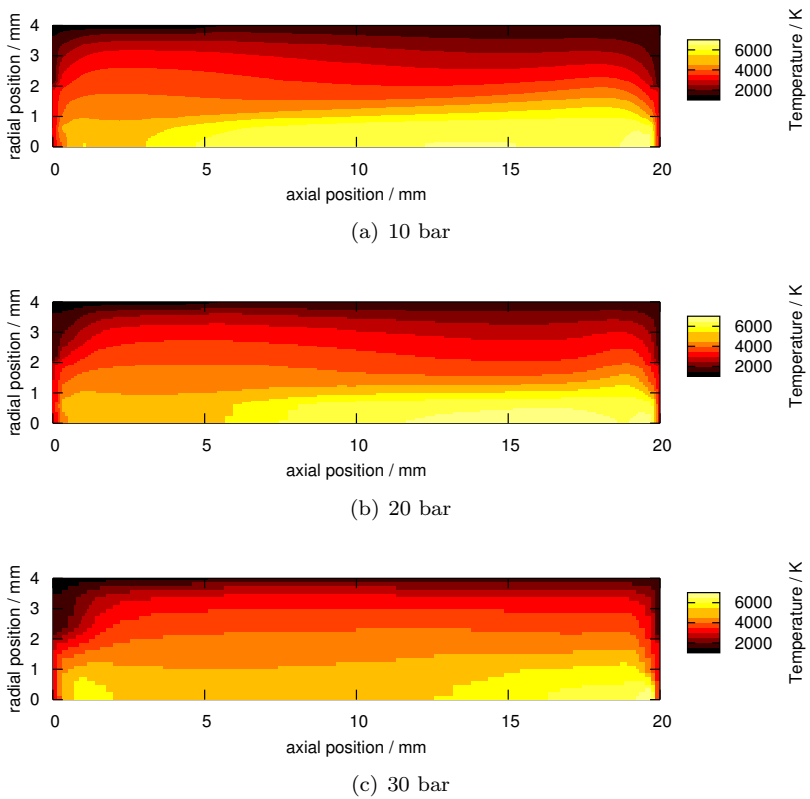
Figure 2.9: The temperature at different total lamp pressures. Note that the areas with the highest temperatures are near the top and bottom of the lamp.
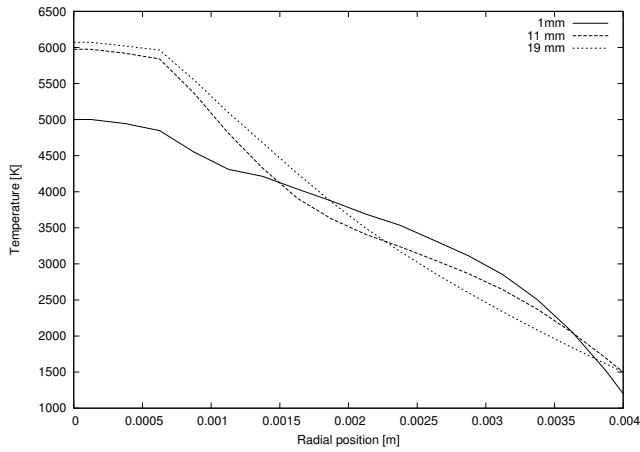
Figure 2.10: Radial temperature profiles at 10 bar for three different axial positions; at 1mm, 11mm and 19mm above the bottom electrode.
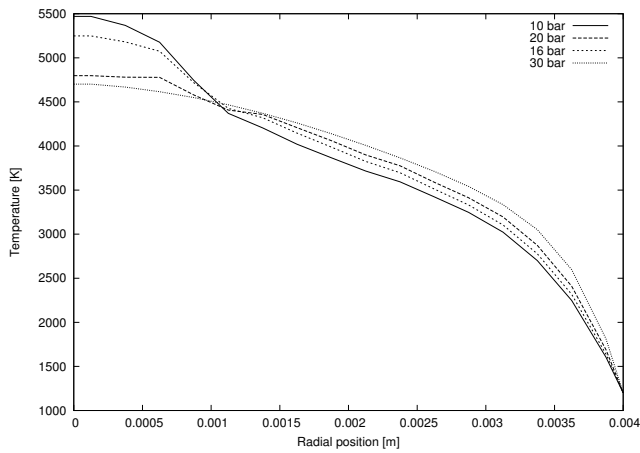
Figure 2.11: Temperature profiles at different pressures 5 mm above the bottom electrode.
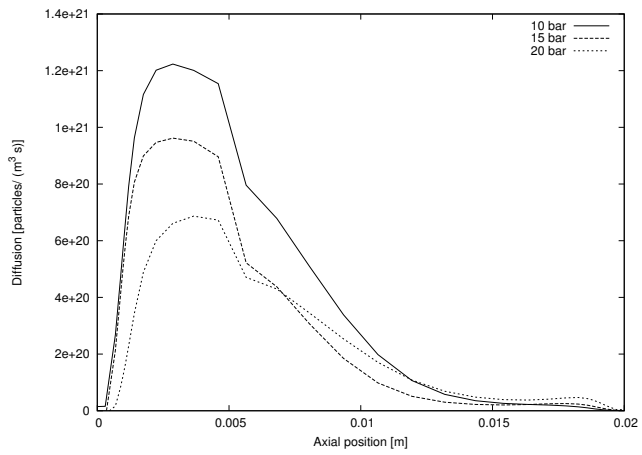
Figure 2.12: Total sodium elemental diffusive flux 1 mm from the wall in the direction toward the wall for three different pressures.

2.A   Addendum

In constructing the model a number of assumptions have been made that require closer examination. This addendum to the original publication will discuss these assumptions. In addition to the assumption of LTE, discussed in section 2.3.4 the following assumptions are made in the model:

1. the flow is laminar,

2. a steady state solution exists and

3. the solution is rotationally symmetric.

2.A.1   Laminar flow

The flow in the model lamp remains laminar due to its small dimensions and the high viscosity of the plasma. To study the laminarity of the flow a full fledged stability analysis is required to look for instabilities and possible bifurcations in the convection pattern. As the flow is strongly non-Boussinesq such a study is non-trivial and beyond the scope of this work. A rough estimate of the laminarity of the flow can be obtained by looking at the dimensionless Reynolds and Grashof numbers and compare these with studies on differentially heated convective cells.

The well-known Reynolds number $Re = \rho V L/\mu$ gives the ratio of inertial to viscous forces. If the Reynolds number is large the flow becomes turbulent. Typical values for the dynamic viscosity, as calculated by the Wilke [36] formula, vary from 5×10^{-4}Pa s in the centre to 2×10^{-4}Pa s near the walls. The lamp has a radius of 4 mm and a height of 20 mm. The density depends on the pressure and the temperature. In a lamp with a pressure of 40 bar the density is between 16 kg/m^3 and 20 kg/m^3 along the centre. The velocity is greatest along the centre, with the velocity reaching 0.2 m/s. Taking 1 cm as a typical length scale, a viscosity of 5×10^{-4}Pa s, a density of 20 kg/m^3 and a velocity of 0.2 m/s one obtains $Re = 80$. This value is well below the values required for a transition to turbulence. For turbulent flow a Reynolds number in the order of 10^3 would be required.

For comparison with results from literature, the Grashof number $Gr = \frac{\rho a_g \Delta T}{\mu^2 T}$ is more useful. The Grashof number gives the ratio of buoyancy to viscous forces. With the previous estimates for the density and using $\Delta T/T = 0.8$ one arrives at $Gr = 600$. Comparing this with studies on differentially heated

cavities by Paolucci [37] suggests that the Grashof number is at least an order of magnitude too low for turbulent and unsteady convective flow.

2.A.2 Time dependent behaviour

Turbulence is not the only possible reason that the solution may not be steady-state. The model-lamp is operated by providing a square wave voltage across the electrodes at 400 Hz. The amplitude is adjusted to provide a constant power input. The frequency of 400 Hz has been chosen precisely to provide a stable light output[9]. Helical instabilities can be induced in MH lamps however [38, 39]. The subject of helical stabilities is also beyond the scope of this work. When comparing with experiments care should be taken not to compare with lamps which show helical instabilities.

2.A.3 Arc bending

The subject of helical instabilities is closely related to arc bending. Both of these lead to deviations from rotational symmetry. X-ray fluorescence measurements on COST lamps do not show significant arc bending or deviations from rotational symmetry [21]. Experiments under hypergravity conditions discussed in chapter 7 do show deviations from rotational symmetry when the centrifuge is operated at high speeds. Consequently, the model has not been compared with results which show deviations from rotational symmetry.

2.A.4 The choice of grid

To solve the differential equations a coarse two dimensional grid is used. The grid has 34 axial and 18 radial positions. The use of such a coarse grid is possible because the flow is laminar and the size of the features studied are large in comparison with the size of the lamp. Grid stretching is used to reduce the size of the cells near the walls where the gradients in the temperature and the elemental pressure are larger. Plasimo uses a hybrid scheme as described by Patankar [15, page 88]. Using this scheme allows reasonable results even with coarse grids. Chapter 7 further examines the discretisation errors in the model.

Chapter 3

Protruding electrodes

Abstract. Convection and diffusion in the discharge region of a metal halide lamp are studied using a computer model built with the plasma modelling package Plasimo. A model lamp containing mercury and sodium iodide is studied. Recently, the underlying program architecture in Plasimo has been overhauled to allow non-rectangular computational domains. We used this new feature to model the effects of the electrodes protruding into the plasma. The effects of the total lamp pressure on the degree of segregation of the light emitting species are examined and compared to the earlier model with flat electrodes. Significant differences are observed, justifying the use of the more complete approach.

3.1 Introduction

In 1912 Charles Steinmetz was granted a patent [3] for a new light source. By adding small amounts of sodium, lithium, rubidium and potassium he was able to modify the light output from "an extremely disagreeable colour" to "a soft, brilliant, white light". It was not until much later, however, that a commercially viable lamp was produced along the same principles. In 1964 General Electric introduced a metal halide lamp at the world trade fair in New York.

Modern Metal Halide (MH) lamps today operate under the same principles. They typically consist of a small inner burner about a centimetre in diameter and a centimetre or more in length surrounded by a larger protective outer wall. The inner burner is made from polycrystalline alumina or quartz and is filled with noble gasses, mercury (about 10 mg) and salt additives (a few mg). Under operating conditions the mercury in the inner burner evaporates raising the pressure to several tens of bar. The advantages of metal halide lamps remain much the same as in Steinmetz' original patent; they combine high luminous output across a broad spectrum of the visible range with good efficacies as compared with other light sources.

The physics behind discharge lamps of this type, however, is still a matter of active investigation. One well known [5, 6, 7, 26] phenomenon still under investigation is that, when operated vertically, the metal halides in the lamp tend to demix; the concentration of metal halides in the gas phase is much greater at the bottom of the lamp. This effect is not present under all conditions, and some lamp designs are more severely affected than others. The demixing can be observed directly from the light output; a demixed lamp shows a blue white mercury discharge at the top of the lamp and a much brighter and whiter discharge from the additives at the bottom of the lamp [8]. Demixing, or axial segregation as it is also called, has a negative impact on the lamp's efficacy.

Previously [40] we published a description of a model to examine demixing as a function of lamp pressure. In this model the lamp geometry was simplified to a straight cylinder with flat ends. Recently, the simulation platform used to construct this model, Plasimo, has been modified to allow computation on polygonal domains with orthogonal sides. This architecture change allows for the simulation of more complicated geometries, such that the effects of the electrodes protruding into the plasma can be included in the model. Using a more advanced model, we re-examine the results from the previous model, in particular the effect of the total lamp pressure on segregation. For the sake of simplicity this study is limited to a lamp containing mercury and sodium iodide. Input data for these species is readily available from public sources. Adding

more elements, such as scandium or dysprosium would add to the complexity of the model without adding much to our understanding of the basic processes involved. Ultimately, though the authors believe it will be possible to use the same approach for commercial lamps such as a NaI-ScI-Hg lamp.

3.2   Demixing

By design, metal halide lamps have high temperature gradients. The get sufficient ionisation, the central axis temperature must be high (at least 5000 K), and the material of which the walls are made cannot sustain temperatures higher than 1500 K, (about 1200 K for quartz lamps). These high temperature gradients give rise to natural convection. Also by design, the metals in the discharge are bound by iodide atoms into molecules near the walls. This protects the walls from excessive corrosion [3]. Towards the centre of the lamp these molecules dissociate. Thus, strong density gradients are found in both molecules and atoms. The density gradients give rise to diffusion. The molecules, however, have larger collisional cross sections with the background mercury vapour than the atoms. Thereby, diffusion results in a greater concentration of additives near the wall. The convection of the background gas redistributes the additives in vertical direction. At moderate convection speeds the effect is axial segregation; the additives are trapped in a convection cell at the bottom of the lamp. At higher convection speeds the additives are more uniformly distributed throughout the lamp. Therefore, there is an optimum convection speed at which the axial segregation is greatest [5]. The convection speeds can be influenced by the total lamp pressure. Higher lamp pressures result in higher convection speeds. The geometry also effects convection patterns. This article will look further into these effects.

3.3   Geometry of the problem

Metal Halide lamps come in various shapes and sizes. To be able to compare results of experiments done on metal halide lamps and to compare the results from models to the experiments a reference lamp has been defined within the framework of the European project COST-529[9]. We base our models on this lamp geometry.

The model has a distance between the electrodes of 2 cm. The length of the inner burner is 3 cm. The diameter is 0.8 cm. We assume that the discharge is

axially symmetric. The models thus use a two dimensional rotationally symmetric grid. In the previous publication [40] we modelled the area of the discharge between the electrodes, along the full radius of the lamp. New improvements to the code allows us to model the influence of the electrodes protruding into the plasma. Figure 3.1 gives a schematic view of the relation between the grids and the discharge.
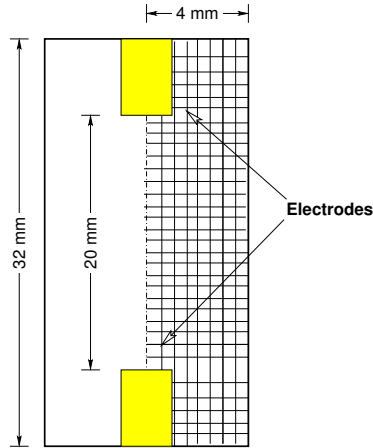
Figure 3.1: Schematic of the grid with respect to the inner burner.

3.4   Structured Meshes

Structured finite volume meshes have the advantage of allowing one to solve partial differential equations on relatively coarse grids, as compared with finite difference or finite element methods. Additionally, they are well suited to the solving of equations representing conserved quantities as the discretisation does not violate the conservation of these conserved quantities. Plasimo [28] uses structured finite volume methods to discretise equations, which are usually formulated as a conservation equation. More complicated geometries are handled by using ortho-curvilinear grids. The ortho-curvilinear grid generation cannot, however, handle sharp corners. Using slightly blunt corners is also not an option as the grid generated will be detriment to the numerical stability of the solution.

For the sake of a stable solution adjacent finite volume cells may not vary greatly in size and aspect ratio. For this reason, the underlying program architecture of the grid has been modified to allow computation on polygonal domains with orthogonal sides. Additionally, the new program architecture makes calculation on one and three dimensional grids possible in the future. This is done by using modern programming techniques to abstract out such concepts as the computational domain. In this article we will focus on the underlying physics and the results of the model.

3.5 Basic equations

Besides the geometry little has been changed with respect to the model presented in [40]. We still assume local thermal equilibrium (LTE). The lamp is operated at a DC power of 100 W using a mixture of mercury and sodium iodide. Contrary to the previous model, the lamp is controlled by adjusting the voltage to achieve a power input of 100W, whereas the previous model imposed a current. The sodium iodide content is controlled by a cold spot temperature of 1200 K. The mercury content is varied to achieve total pressures ranging from 8 to 22 bar. In this section a short overview of the basic equations is given.

3.5.1 Energy balance

All modules come together in the energy balance to calculate the plasma temperature. The temperature, in turn, strongly influences the transport coefficients, composition, flow and radiation. The temperature is given by

$$\nabla \cdot (C_p \vec{u} \nabla T) - \nabla \cdot (\lambda_c \nabla T) = P - Q_{rad}, \tag{3.1}$$

where C_p is the heat capacity at constant pressure, $\vec{v}$ the bulk velocity, λ_c the thermal conductivity, Q_{rad} the net radiated power and P the Ohmic dissipation. Viscous source terms are neglected.

To obtain boundary conditions, a cold spot temperature of 1200 K is assumed, with the cold spot located in the bottom corner of the lamp. The electrodes are assumed to have a surface temperature of 2900 K and the rest of the wall a temperature of 1500 K.

The term Q_{rad} is the result of 2D ray-tracing. We solve the equation for the radiation intensity [41]

$$\frac{dI_\nu}{ds} = j_\nu - \kappa I_\nu, \tag{3.2}$$

with j_ν the local emission coefficient and κ the local coefficient for absorption along rays passing through the discharge as depicted in figure 3.2.

The net radiated power is given by [41]:

$$Q_{rad} = \int_\nu \left(4\pi j_\nu - \int_{4\pi} \kappa I_\nu d\Omega \right) d\nu, \qquad (3.3)$$

with ν the frequency. We discretise 3.3 by regarding the difference between the radiative flux at the surfaces of each finite volume cell along the path of each probe line. The radiative flux Φ_ν^ε per frequency point through a surface with area A and normal direction n is given by

$$\Phi_\nu^\varepsilon = A I_\nu \vec{n} \cdot d\vec{\Omega}, \qquad (3.4)$$

where $d\vec{\Omega}$ is the solid angle around the ray. The net radiated power per frequency point $Q_{rad,\nu}$ for a grid cell where the ray enters at position s and leaves at position $s + ds$ is given by [41]:

$$Q_{rad,\nu} = \frac{1}{V} \left(\Phi_\nu^\varepsilon(s + ds) - \Phi_\nu^\varepsilon(s) \right), \qquad (3.5)$$

where V is the volume of the cell. The net radiated power is given by summation of $Q_{rad,\nu}$ over all rays and frequency points in each cell.

3.5.2 Particle transport

Since we assume LTE, the particle densities may be described by the local temperature, pressure and elemental composition.

To describe the local elemental composition we introduce the elemental pressure p_α for the element α:

$$p_\alpha = \sum_i R_{i\alpha} p_i, \qquad (3.6)$$

with p_i the partial pressure of the species i, and $R_{i\alpha}$ the stoichiometric coefficient [40].

We solve a conservation equation for the elemental pressure

$$\nabla \cdot \left(\frac{D_\alpha}{kT} \nabla p_\alpha + \frac{p_\alpha}{kT} \vec{c}_\alpha \right) = 0,$$

with an effective diffusion coefficient

$$D_\alpha = p_\alpha^{-1} \sum_i R_{i\alpha} D_i p_i$$

side–on view   top–view

a   b   c
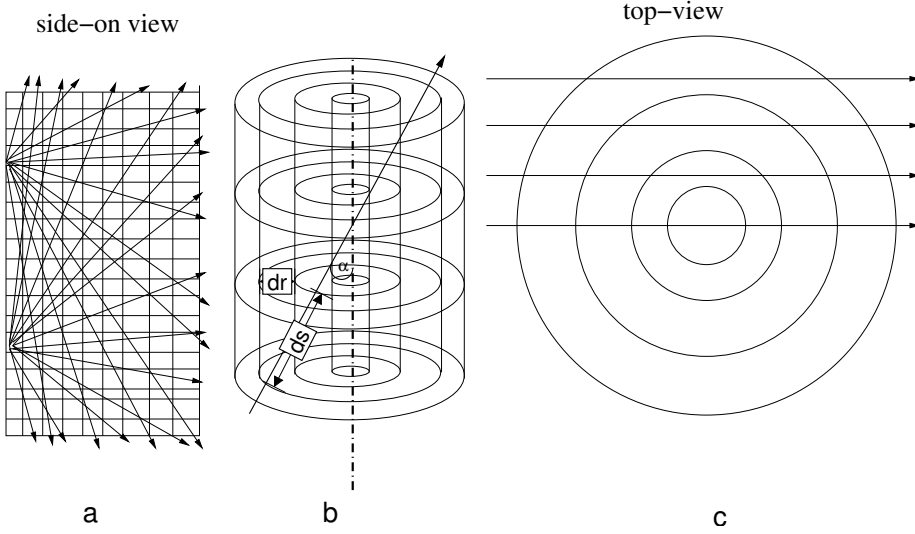
Figure 3.2: Ray tracing through a cylinder making use of radial symmetry. Rays intersect the cylinders at different angles with the horizontal plane. Seen from the top the symmetry can be used to arrange the rays in a set of parallel lines, but seen from the side rays with different angles to the horizontal plane are required.

and a pseudo convective velocity

$$\vec{c}_\alpha = \vec{u} + \sum_i R_{i\alpha} D_i \frac{q_i}{q_e} \frac{\nabla p_e}{p_e} - \sum_i R_{i\alpha} D_i \nabla \left(\frac{p_i}{p_\alpha} \right). \qquad (3.7)$$

The diffusion coefficient of species i through the dominant background mercury vapour is denoted as D_i. The ion charge is given by q_i and the charge of the electrons by $q_e = -e$.

To fix the boundary conditions we assume the existence of a cold spot at the bottom corner of the lamp, where the elemental pressure is given to be 1016 Pa. Everywhere else the flux through the wall is zero.

3.5.3 Ohmic heating

The power to the plasma is supplied by Ohmic heating. In the model with the old grid using flat electrodes ohmic heating was simulated by assuming an axial electric field $E(z)$ and a negligible radial field. The electric field in the axial direction $E(z)$ is related to the current by:

$$I = 2\pi \int_0^R \sigma(z,r)E(z)r\,dr,\tag{3.8}$$

with $\sigma(z,r)$ the electrical conductivity. The electric field is thus given by

$$E(z) = I\left(2\pi \int_0^R \sigma(z,r)r\,dr\right)^{-1}.$$

The position dependent volumetric power dissipated by Ohmic heating is given by $\sigma(z,r)E^2$.

In the current model we solve the Poisson equation in the form:

$$\nabla \cdot (\sigma \nabla \Phi) = 0,\tag{3.9}$$

with Φ the potential. The boundary conditions are formed by constant Dirichlet conditions on the electrodes and homogeneous Neumann conditions on the walls. An initial guess of 100 V is used for the potential difference across the electrodes. This potential difference is adjusted to obtain a net input power of 100 W.

In an area of 0.5 mm around the electrodes the conductivity is adjusted to compensate for non-LTE effects. This is necessary since the electron density near the electrodes will deviate significantly from the values expected from chemical equilibrium. Not correcting for these effects would effectively couple all the electrical energy in the first layer of cells near the electrodes, overestimating the temperature in these cells, while underestimating temperature elsewhere.

3.5.4 Transport properties

The transport properties are calculated from collision integrals and using the concentration of the relevant species and the temperature. For more details see [42] and chapter 6.

3.5.5   Bulk flow

The bulk flow follows from the Navier Stokes equation:

$$\nabla \cdot (\rho \vec{u}\vec{u}) = -\nabla p + \nabla \cdot (\mu \nabla u) + \rho \vec{a}_g, \qquad (3.10)$$

with p the pressure, $\vec{u}$ the velocity, $\vec{a}_g$ the acceleration due to gravity, μ the dynamic viscosity and ρ the density of the plasma.

3.6   Results

To compare the results with the previous model with flat electrodes the new model with protruding electrodes was tried with a number of different lamp pressures. The calculated temperatures and temperature gradients do not differ much in magnitude between the old and the new grids. The profiles, however do differ. This influences the convection patterns in the lamp and, thereby, influences axial segregation.

The convection speed also depends on the lamp pressure. We ran the model for a variety of lamp pressures ranging from 9 to 22 bar. We will now discuss the outcome of the model in terms of the temperature, flow patterns and sodium demixing.

3.6.1   Temperature

Two examples of the resulting temperature from a calculation are given in figure 3.3. As expected, the temperature is much higher at the axis (6000 K) than along the wall. The temperature is highest near the top and bottom electrodes where the ohmic dissipation is greatest. Additionally, the temperature is higher at the top of the lamp, due to the transport of heat by natural convection. This is more clearly evident in figure 3.4 showing the temperature along the axis between the electrodes. Increasing the lamp pressure increases convection, thereby increasing the asymmetry between the top and the bottom of the lamp. This also becomes apparent by comparing results at 22 bar (also shown in figure 3.3) with results at 9 bar. Comparing the result with the model with flat electrodes shows that the new model produces more realistic results near the electrodes. The model with the older grid showed artifacts near the bottom electrode, and to a lesser degree near the top electrode.

(a) 9 bar

(b) 22 bar

$\vec{g}$
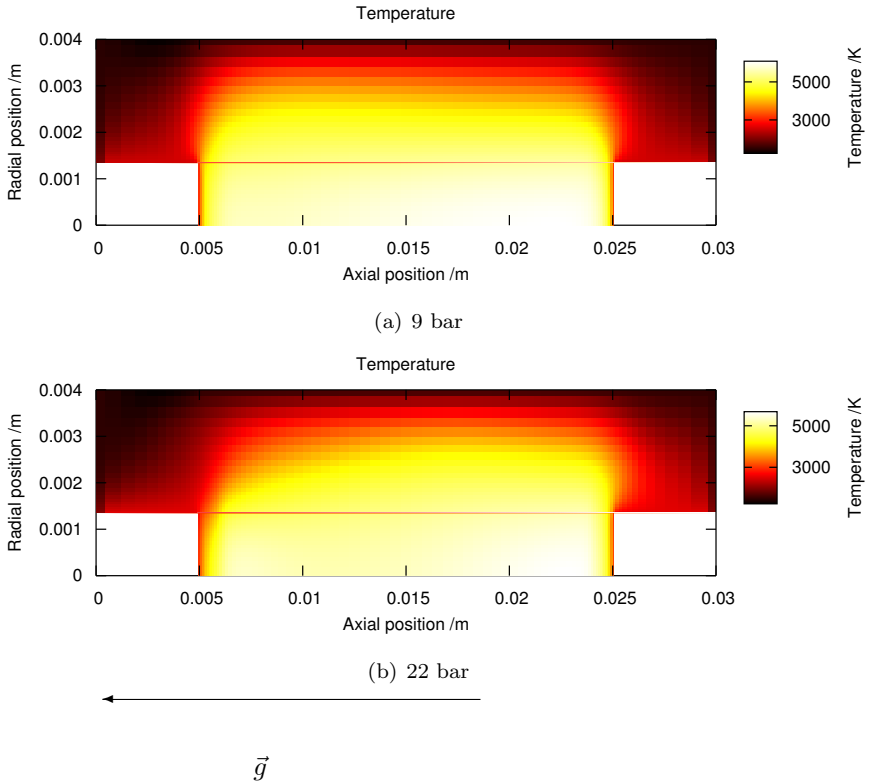
Figure 3.3: Temperature distribution at 9 bar and 22 bar lamp pressure. The axis temperature is much greater than the wall temperature. The area near the electrodes is hottest. Comparison the two figures shows that increasing the pressure makes the discharge more asymmetric in the axial direction.

3.6.2 Bulk Flow

The protruding electrodes also effect the flow pattern. This is shown in figure 3.6. In particular, the flow velocity towards the top of the lamp is lower in the model with protruding electrodes. Possibly, the electrodes hinder convection in the lamp.
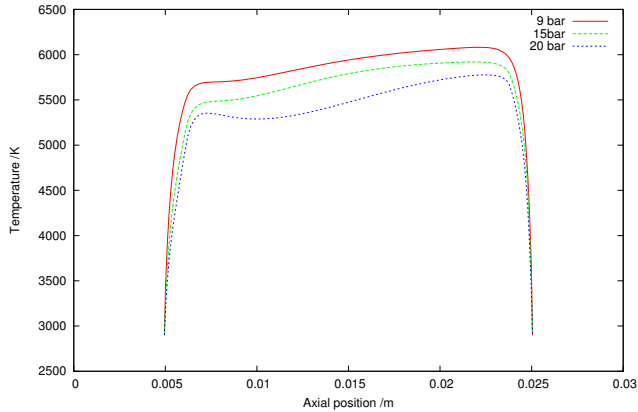
Figure 3.4: Temperature along the axis, for different pressures.

3.6.3 Demixing

Given the results shown previously, it is not surprising that the demixing of sodium is also effected by the protruding electrodes. The axial segregation tends to be greater in the model with protruding electrodes. This can be deduced from figure 3.7.

Aside from a small area around the electrodes, the elemental pressure along the axis decays exponentially as a function of the axial position. This is also shown in figure 3.7.

Fitting an exponential curve through the results results in a measure for the degree of axial segregation. Plotting this decay constant, or segregation parameter, as a function of the lamp pressure results in figure 3.8. As lamp pressure is also related to convection, this curve shows the effect of convection on the degree of segregation. As is evident from this curve, increasing the convection beyond a certain point leads to better mixing, as does decreasing it. The optimal middle is what lamp designers should avoid. The flat electrode models shows a small but significant shift in the pressure for which segregation is greatest. Additionally, the degree of segregation is larger in the model with the protruding electrodes than in the model with the flat electrodes.
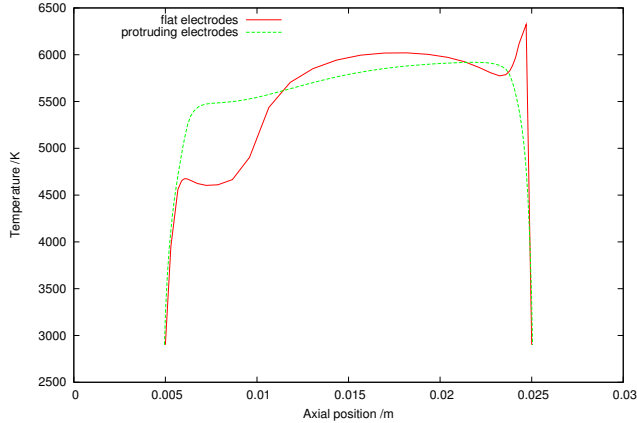
Figure 3.5: Temperature along the axis compared to the model with flat electrodes previously published in [40] at 15 bar lamp pressure.

3.6.4   Iodine

The demixing of iodine is much less pronounced than that of sodium. Figure 3.9 shows how iodine is spread throughout the lamp. Iodine ionises less easily than sodium. Additionally, the iodine atoms are larger, leading to larger elastic cross sections.

3.7   Discussion

The model presented in chapter 2 has been extended to model protruding electrodes. Having the electrodes protrude into the plasma creates a "dead zone" outside of the discharge with relatively low temperatures. The hottest zones are to be found close to the electrodes and on the axis between the electrodes. For this first study with protruding electrodes, fairly thick electrodes were used which extend far (3 mm) into the plasma. The actual geometry described in [9] calls for electrodes extending only 1 mm into the lamp. This geometry is used in the later chapters of this thesis. Measurements by Baede [43] on a sample of 29 reference lamps, however, indicate that the actual electrode distance varies from 14.7 mm to 16.5 mm. The average of the sample was 15.7 mm with a
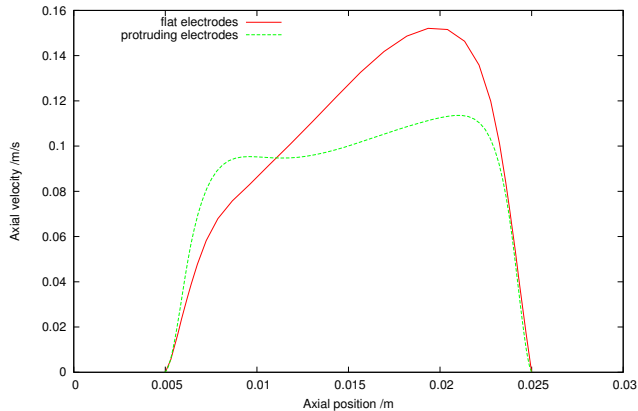
Figure 3.6: Axial velocity along the axis at 15 bar total lamp pressure with the flat electrode model [40] and the model with protruding electrodes compared. The model with protruding electrodes shows a much flatter profile. The convection velocities near the electrodes are higher, and the axial velocity at the centre is lower.

variance of 0.2 mm.

The additive distributions do not differ greatly from those calculated in chapter 2, but the difference is significant enough to justify the extra effort. The electric field calculation was also improved in this chapter. In chapter 2 the electric field was assumed to be axially directed. This one-dimensional electric field was then calculated by imposing the current that flows between the electrodes. This publication calculated the potential distribution from Poisson's equation. As with the ballasts used in experiments, a certain power dissipation is imposed. In this publication a value of 100 W was used. The voltage across the electrodes is iteratively adjusted to match this power dissipation. This change in the model also facilitates comparison with experiments.

Figure 3.7: Elemental pressure along the axis at 15 bar total lamp pressure. The iodine shows almost no axial segregation.
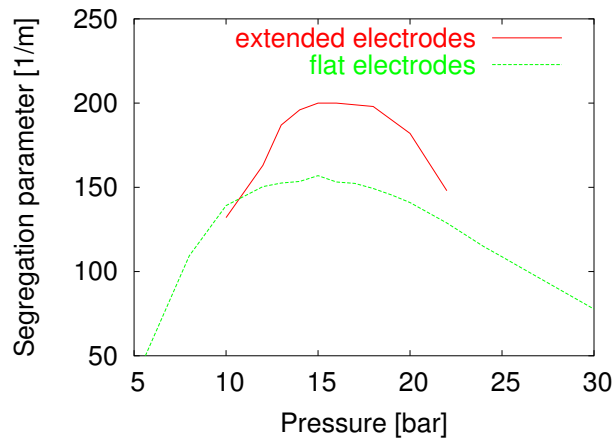
Figure 3.8: The segregation parameter as a function of total lamp pressure.
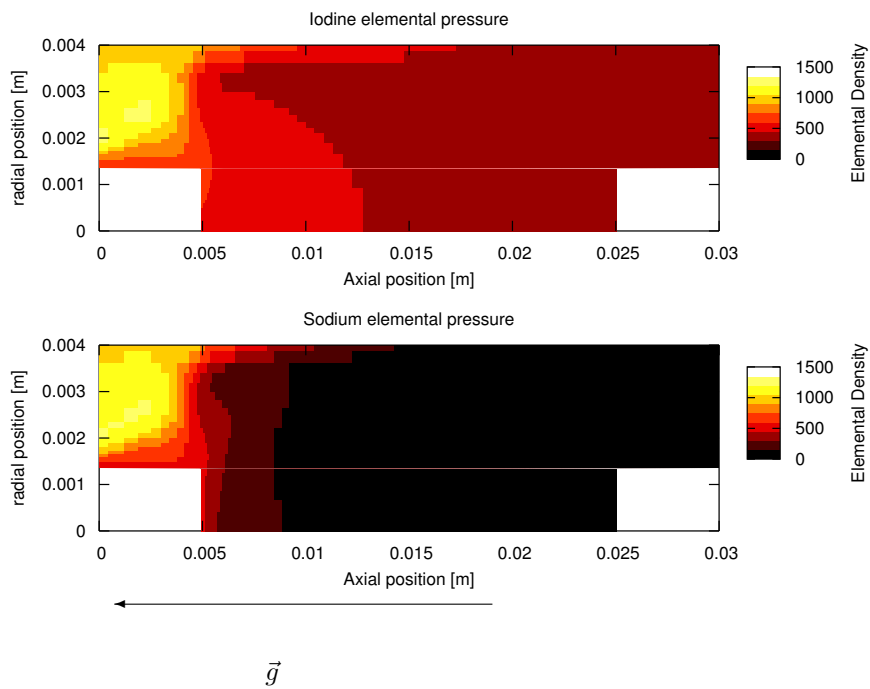
Figure 3.9: Sodium and iodine elemental pressures at 15 bar pressure.

Chapter 4

Extending the model, DyI_3 chemistry

Abstract.
The distribution of additives in a metal halide lamp is examined through numerical modelling. A model for a lamp containing sodium iodide additives has been modified to study a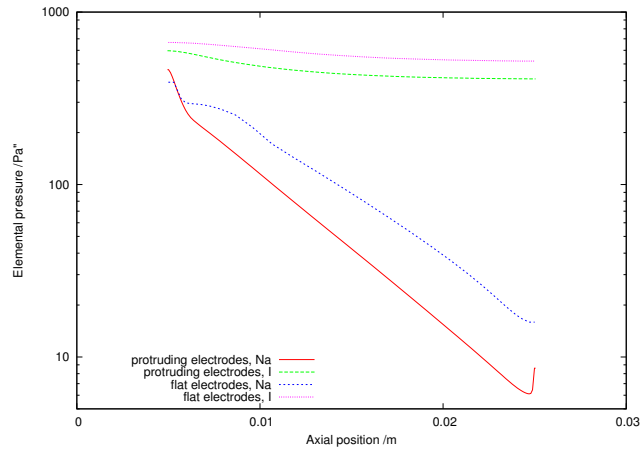 discharge containing dysprosium tri-iodide salts. To study the complex chemistry the method of Gibbs minimisation is used to decide which species have to be taken into account. The results from the model with dysprosium additives are compared with earlier results from the lamp containing sodium additives and a simulation of a pure mercury lamp. Under the right conditions convection currents in the lamp can cause axial demixing. These conditions depend on the ratio of axial convection and radial diffusion as expressed by the Peclet number. At a Peclet number of unity axial segregation is most pronounced. At low Peclet numbers radial segregation is at its strongest, while axial segregation is not present. At large Peclet numbers the discharge becomes homogeneously mixed. The degree of axial segregation at a Peclet number of unity depends on the temperature at which the additive under consideration fully dissociates. If the molecules dissociate very close to the walls no molecules are transported by the convective currents in the lamp, and hence axial segregation is limited. If they dissociate further away from the walls, in the area where the downward convective currents are strongest, more axial segregation is observed.

This chapter has been submitted to J. Phys D. as "A model for additive transport in metal halide lamps containing mercury and dysprosium tri-iodide" with the co-authors M. Haverlag and J. J. A. M. van der Mullen

4.1 Introduction

In chapter 2 we presented a study that describes how segregation results from the competition between convection and diffusion. For this we used a model that was constructed by means of the modelling platform Plasimo[16]. This model gives a self-consistent calculation of the competition between convection, diffusion, the LTE chemistry, the electric field and the radiation transport. It was found in chapter 2 that increasing the pressure increases convective flows in the lamp. With high enough pressure, segregation disappears since the high convective flows lead to better mixing of the species over the discharge. At low pressures axial segregation is not present, though radial segregation will still be present, since this is driven by diffusion. The model can be used to predict the range of pressures that should be avoided when designing a lamp. A disadvantage of this model was that the electrodes were approximated by two flat planes.

In chapter 3 we improved the model by taking the shape of the electrodes into account. This model with electrodes protruding into the lamp was run for a series of conditions and it was found that the electrodes influence convection patterns in the lamp. The changes in the convection also has effects on the distribution of additives and the pressure at which the demixing is most pronounced.

Both chapters 2 and 3 were based on MH lamps consisting of a mixture of Hg and NaI. To compare the model results with experiments the authors have extended the model to work with dysprosium iodide. The primary reason for this is that we wish to compare results with the measurements in [21], which uses the technique of X-Ray Fluorescence (XRF) to measure the elemental densities. This technique works with heavy elements such as mercury and dysprosium but not with sodium.

The chemical composition of a plasma containing DyI_3 is more complex than a similar discharge containing NaI. The reason is that more intermediate species such as DyI_2 and DyI are present in the former. Although it would be possible to expand the approach used in chapters 2 and 3, adding more species, and thus more relations, would drastically slow down the calculation. Additionally, the molecules are more complex, resulting in increased complexity when calculating the partition functions. The method used in chapters 2 and 3 is based on the equations of Guldberg-Waage and Saha, as outlined in [31, chapter 2]. Applying this method for more complex molecular mixtures leads to the demand to calculate complicated partition functions. To circumvent this demand we applied the Gibbs Minimisation (GM) method, which allows for

the use of databases of thermodynamical properties of species to calculate the chemical composition of the plasma. We used an external commercial program to generate lookup tables filled with species densities for different combinations of the total pressure, elemental abundancy and temperature. Fortunately, it was found that the number of species that have to be dealt with is limited. Besides the electrons, whose density is calculated from charge neutrality, only eight species are present in significant concentrations in the discharge.

Another difference between an MH lamp with dysprosium iodide additives with an MH lamp with sodium iodide as additive is that the spectrum of dysprosium is much more complex. The spectra of dysprosium contains a "grass field" of lines, with [44] listing 900 lines. In the case of sodium a mere 19 lines are sufficiently prominent. This issue is discussed in chapter 5.

This chapter will focus on the differences in the lamp chemistry and present results comparing a lamp containing sodium with the same lamp containing dysprosium.

4.2 Chemistry

Assuming local chemical equilibrium means that the plasma composition is determined by the local temperature, pressure and relative abundance of elements. In the case of a vapour consisting of dysprosium, iodide and mercury a number of molecules can be formed. Additionally, the neutral atoms may ionise. In contrast to the previous studies in chapters 2 and 3 the LTE chemistry in the present study is described by Gibbs Minimisation (GM) rather than by the previous method using the Guldberg-Waage law of mass action and Saha balances (GWS). For an ideal gas mixture the two approaches are equivalent [45, chapter 3,4] as the former may be derived from the latter. The GM approach is more general as it can also be used for non-ideal gases, liquids and multi-phase mixtures. More importantly, for the GM approach one does not need to calculate partition functions but one may use derived thermodynamic properties. Tabulated data for the thermodynamic properties of species are widely available, along with software (both commercial and open source) to use such data with the GM approach. Using such (semi-) empirical data rather than calculating the partition function for each species reduces the complexity of the problem. This is of special interest since the dysprosium containing species have a large number of possible states, which makes calculating the partition function complex and time consuming.

Tabulated data for the relevant thermochemical properties of particular

species can come from a wide variety of sources. For example, the heat capacity at constant pressure can be used to determine the chemical potential [46]. This is because the heat capacity at constant pressure C_p is given by $C_p = \left(\frac{\partial H}{\partial T}\right)_p$. The entropy is also related to the heat capacity as $C_p = T\left(\frac{\partial S}{\partial T}\right)_p$. Hence, the Gibbs energy G can be found by integrating C_p and adding a reference value at a given reference temperature. We will give a short sketch of the GM approach without going into great detail. More details on specific algorithms and sources of data are given in [47].

The principle of GM follows from the principle of maximum entropy $dS \geq 0$ under the constraint of constant pressure and temperature. For the transfer of heat at constant pressure the inequality :

$$dH - TdS \leq 0,$$

holds, with H the enthalpy and S the entropy of the system. It is convenient to introduce the Gibbs energy G such that

$$G = H - TS. \tag{4.1}$$

The criteria for spontaneous reactions at constant pressure and temperature is given by

$$dG_{T,p} \leq 0. \tag{4.2}$$

The local species densities can be found by determining the minimum value for G under the constraints

$$n_i \quad \geq \quad 0 \ \ \forall i, \tag{4.3}$$

$$\sum_i R_{i\alpha} kT n_i \quad = \quad p_\alpha \ \forall \alpha \ \ \text{(elemental abundance)}, \tag{4.4}$$

$$\sum_i kT n_i \quad = \quad p \ \ \text{(Daltons' law)}, \tag{4.5}$$

$$\sum_i n_i q_i \quad = \quad 0 \ \ \text{(charge neutrality)}. \tag{4.6}$$

The total Gibbs function of the system is calculated from the individual species as

$$G(T, p, n) = \sum_i n_i \mu_i, \tag{4.7}$$

with μ_i the chemical potential. By solving equation (4.2) under the constraints of (4.3) to (4.6) we find the local densities of all species in the plasma.

The chemical potential could be calculated from the partition function of the species but the usual approach is to parametrise the chemical potential as a function of temperature. We use Chemapp$^{\text{TM}}$ to solve (4.7) under the given constraints to generate a lookup-table of densities for different combinations of the temperature, pressures and elemental compositions. Chemapp$^{\text{TM}}$ parametrises the chemical potential using the fit function [48, 49]

$$\mu(T) = \sum_{i=-1}^{3} c_i T^i + aT \log T + \sum_{i=1}^{6} b_i T^{d_i} \tag{4.8}$$

with a, b_i, c_i and d_i species dependent and range dependent parameters.

An example of the result for an elemental Dysprosium pressure of 100 Pa, an elemental Iodine Pressure of 300 Pa and a total pressure of 2 MPa is shown in figures 4.1, 4.2 and 4.3 respectively showing the species containing dysprosium, mercury and iodine. Based on this data the choice was made to limit the model to the following species: Hg, Hg$^+$, Hg$_2$, Dy, Dy$^+$, DyI$_2$, DyI$_3$, I$_2$ and electrons.

4.3 Particle transport

Since we assume the presence of LTE, the particle densities may be described by the local temperature, pressure and local elemental composition with the GM method described in the previous section. The local elemental composition is determined by the vapour pressure at the cold spot and the competing processes of convection and diffusion which distribute the salt components throughout the lamp.

4.3.1 Radial segregation

To understand the process driving axial segregation one first needs to examine radial segregation. The additive molecules in the plasma diffuse from the wall into the centre of the plasma where they dissociate to form free atoms. These are partially ionised. The lighter and smaller atoms diffuse back toward the wall more readily through the background mercury gas than the molecules diffuse in the opposite direction.

We assume, for the purpose of this discussion, that the diffusion is given by

Figure 4.1: Selected species densities containing dysprosium calculated for a mixture containing mercury, dysprosium and iodine elements. Species densities for species containing mercury and iodine are shown in figures 4.2 and 4.3 respectively to avoid clutter. The elemental dysprosium pressure is 100 Pa, the elemental iodine pressure 300 Pa and the total pressure 2 MPa. The temperature is between 1000 K and 7000 K. The density of DyI is very low compared to other dysprosium containing species, so this species is not taken into consideration in the model.

Fick's law[1] Thus the flux of species i $\vec{\Gamma}_i$ is given by

$$\vec{\Gamma}_i = -D_i \nabla p_i, \qquad (4.9)$$

with D_i the diffusion coefficient and p_i the partial pressure of species i. In the absence of convection, the flux of atoms towards the walls must equal the flux

---

[1]Note that, in general, the diffusion of species in the plasma does not obey Fick's law and the numerical model does not assume this as discussed in chapter 2.
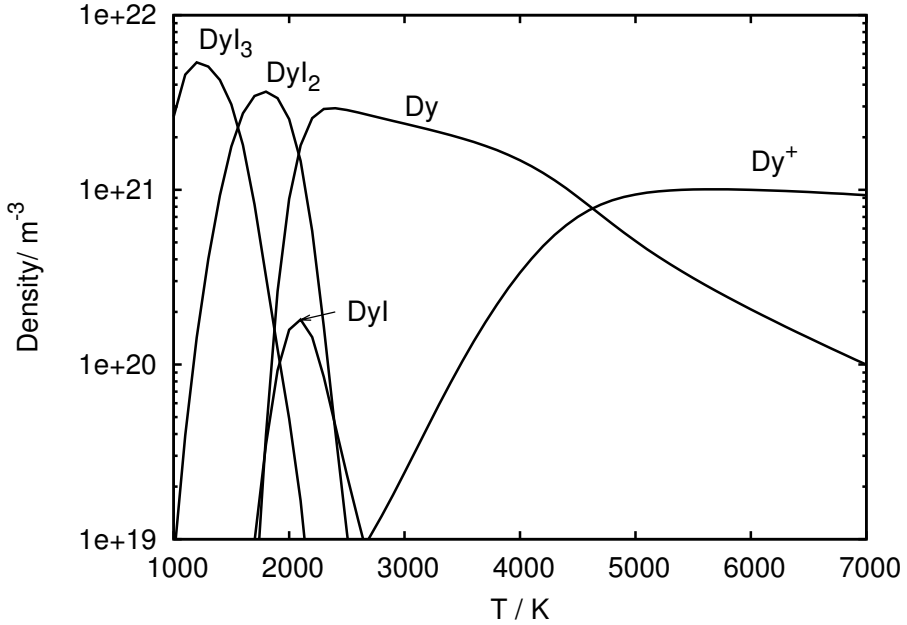
Figure 4.2: Selected species densities containing mercury, calculated for a mixture containing mercury, dysprosium and iodine elements. Species densities for species containing dysprosium and iodine are shown in figures 4.1 and 4.3 respectively to avoid clutter. Just as in figure 4.1 the elemental dysprosium pressure is 100 Pa, the elemental iodine pressure 300 Pa and the total pressure 2 MPa. The temperature is between 1000 K and 7000 K. The density of HgI and HgI$_2$ is very low compared to other mercury species. These species have not been taken into account in the model.

of molecules away from the walls multiplied with the stoichiometric coefficient. Substitution of this equality into (4.9) results in

$$R_{mol,element} D_{mol} \nabla p_{mol} = -D_{atom} \nabla p_{atom}, \qquad (4.10)$$

with $R_{mol,element}$ the stoichiometric coefficient. Rearranging the above leads to

$$\nabla p_{atom} = -\left(\frac{R D_{mol}}{D_{atom}} \right) \nabla p_{mol}. \qquad (4.11)$$
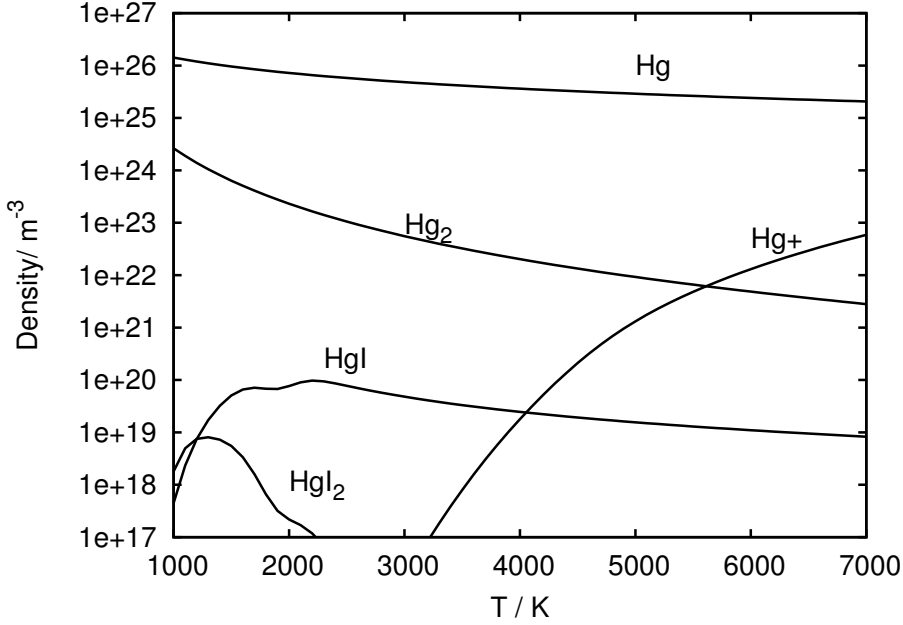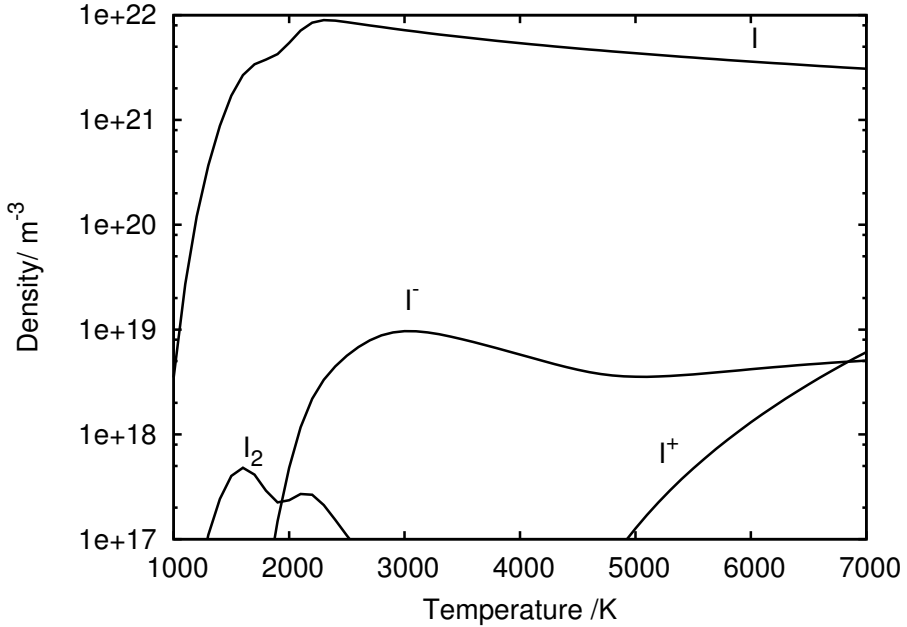
Figure 4.3: Selected species densities containing iodide only, calculated for a mixture containing mercury, dysprosium and iodine elements. Species densities for species containing dysprosium and mercury are shown in figures 4.1 and 4.2 respectively to avoid clutter. Just as in figures 4.1 and 4.2 the elemental dysprosium pressure is 100 Pa, the elemental iodine pressure 300 Pa and the total pressure 2 MPa. The temperature is between 1000 K and 7000 K. The density of I_2 is very low compared to other iodine species in this example since there is no excess iodine. These species not been neglected in the model, however, since the model does have a large amount of excess iodine. Iodine ions are not taken into account in the model since their densities are much lower than the other ion densities.

Since $D_{\mathrm{atom}} > D_{\mathrm{mol}}$ a larger gradient of the molecular partial pressure can be supported ($\nabla p_{\mathrm{atom}} < \nabla p_{\mathrm{mol}}$). Thus, radial segregation occurs, with more of the additive in the form of molecules near the walls than in the form of atoms in the centre of the discharge. The stoichiometric coefficient is also of importance, however, as each DyI_3 molecule transports three iodine atoms as it

diffuses towards the wall. Thus the radial iodine segregation is limited.

4.3.2 Axial segregation

The large temperature gradients in the lamp drive natural convection. The convection of the buffer gas drags the additives down along the walls and up again through the centre of the discharge. Because the atoms diffuse outward more readily than the molecules diffuse inward the additives stay at the bottom of the discharge. This effect is known as axial segregation.

However, if the convection currents are large enough homogeneous mixing is achieved. At intermediate convection speeds axial segregation is observed but radial segregation is decreased.

4.3.3 Elemental pressure

A convenient quantity to describe the elemental composition is the elemental pressure p_α . The elemental pressure p_α contains the contribution of the partial pressures of all molecular, atomic and ionic species containing a particular element α. It is defined as follows:

$$p_\alpha = \sum_i R_{i\alpha} p_i. \qquad (4.12)$$

This quantity is convenient because the total pressure is nearly constant over the lamp. Therefore, the elemental pressure is also constant if the lamp is homogeneously mixed. Additionally, a conservation equation can derived for the elemental pressure [32, 40].

The conservation equation for the elemental pressure is as follows:

$$\nabla \cdot \left(\frac{D_\alpha}{kT} \nabla p_\alpha + \frac{p_\alpha}{kT} \vec{c}_\alpha \right) = 0, \qquad (4.13)$$

with an effective diffusion coefficient D_α [40]

$$D_\alpha = p_\alpha^{-1} \sum_i R_{i\alpha} D_i p_i \qquad (4.14)$$

and a pseudo convective velocity c_α [40].

To fix the boundary conditions of (4.13) we assume the existence of a cold spot at the bottom corner of the lamp. The elemental pressure in the cold spot

is fixed. For all other boundaries, we assume that the flux of elements through the wall is zero.

For the lamp containing DyI_3 the elemental pressure is derived from the x-ray induced fluorescence measurements[21]. This technique can be used to determine the elemental density of mercury, dysprosium and iodide. We use the measured density near the cold spot combined with the cold spot temperature of 1100 K to arrive at a cold spot pressure of 517 Pa for dysprosium and 4268 Pa for iodine. Note that there is a lot of excess iodine, with iodine not three times but more than eight times as abundant. This is because the dysprosium migrates into the quartz walls.

For the lamp containing sodium iodide a cold spot vapour pressure of 1216 Pa has been assumed for both sodium and iodide. X-ray induced fluorescence measurements cannot be used to determine the elemental sodium pressures because the setup used in [21] is not suitable for the relatively low energy photons emitted from sodium.

Accurate determination of the vapour pressures presents a challenge in studying metal halide lamps. This is because in situ measurements are difficult to perform. Additionally, the vapour pressure is very sensitive to the temperature of the cold spot. Another hindrance is that the relative abundance of metals and halides varies over the life time of the lamp as the metals are absorbed by the walls leading to excess iodide.

4.4   Model

The distribution of elements is calculated by the model described in chapters 2 and 3. This model solves conservation equations to obtain the temperature, velocity and additive distribution in the lamp. A schematic view of the geometry and grid used is given in figure 4.4.

4.4.1   Ohmic heating

The power to the plasma is supplied by Ohmic heating. We solve the Poisson equation in the form:

$$\nabla \cdot (\sigma_{el} \nabla \Phi) = 0, \tag{4.15}$$

with Φ the potential. From the potential Φ we can derive the electric field $\vec{E} = -\nabla \Phi$ and the current density $\vec{J} = \sigma_{el} \vec{E} = -\sigma_{el} \nabla \Phi$. The following boundary conditions are employed:
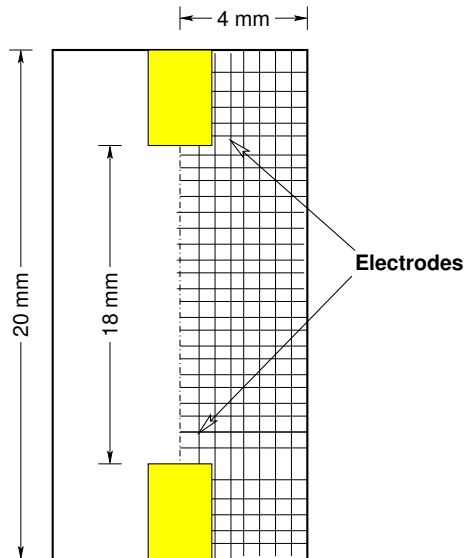
Figure 4.4: Schematic view of the geometry of the problem (not to scale) and the finite volume grid used. The actual grid used is less coarse than suggested in this figure. The computation grid has 66 cells in the axial and 28 cells in the radial direction.

1. There is no current through the walls, resulting in a homogeneous Neumann boundary condition ($\frac{\partial \Phi}{\partial n} = 0$).

2. One electrode is kept at zero potential, which leads to a Dirichlet condition $\Phi = 0$ at that electrode.

3. The potential of the other electrode is initially put at 100 V. This value is adjusted during the iteration process and determined by the fact that the power dissipated in the discharge equals 135 W. This is equivalent to the actual lamp power of 150 W of which 15 W is consumed by electrode losses and 135 W by ohmic dissipation of the discharge.

4.5 Results

With this model dedicated to mixtures containing dysprosium iodide, we are now capable of calculating the properties of a discharge with a dysprosium chemistry as well as comparing these calculations with experiments. The comparison with experiments is the focus of chapters 6 and 7 In the following we will compare with the results of a lamp containing sodium iodide and a lamp containing pure mercury without additives. We will refer to the lamp containing sodium iodide and the lamp containing dysprosium iodide as the sodium and the dysprosium MH lamp, respectively.

We ran the dysprosium MH model with a total mercury filling of 20 mg, and a power input of 135 W using effective transitions calculated from data in [44] as described in chapter 5 and a dysprosium cold spot vapour pressure from [21]. The results from this model were compared with the sodium MH model with the same mercury filling and power input but with 19 sodium transitions and a cold spot vapour pressure of 1016 Pa for both sodium and iodide. The model run was also repeated with the same mercury filling and input power but without additives to simulate a pure mercury lamp. To further compare the model results with previous results with a sodium lamp in chapter 3 the dysprosium MH model was run at various mercury fillings ranging from 3 mg to 20 mg to find the pressure at which the axial segregation is most pronounced.

4.5.1 Additive distribution

The prime quantity of interest in this study is the distribution of additives over the lamp. In previous publications we examined axial demixing as a function of pressure. It was found in chapter 3 that lamps containing sodium iodide shows the most demixing at pressures between 15 and 20 bar, corresponding to a mercury of filling of approximately 20 mg. Under these conditions dysprosium MH lamps show less axial demixing, as is shown in figure 4.5. The elemental pressure of dysprosium drops steeply near the electrodes and is constant for most of the length of the discharge, whereas the sodium elemental pressure decreases along the length of the discharge. The radial elemental pressure profiles are shown in 4.6. Note that the elemental dysprosium pressure shows a strong dip near the axis, as was also reported in measurements [21]. The sodium discharge does not show this central dip.

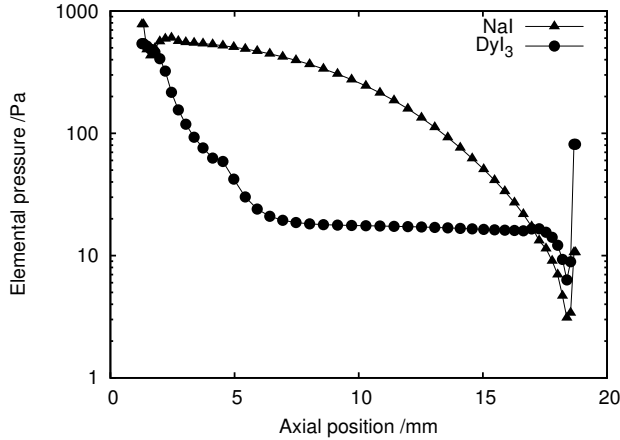To quantify the degree of axial demixing we introduce the dimensionless

Figure 4.5: Elemental pressure of the metal additive along the axis of a sodium MH lamp, compared to a dysprosium MH lamp. Both lamps have a total mercury filling of 20 mg and are driven with 135 W of power. From these results it is also apparent that the elemental pressure does not always decrease exponentially along the axis.

segregation depth τ:

$$\tau = \frac{1}{V} \int_V \tau_L dV, \tag{4.16}$$

with τ_L given by

$$\tau_L = \frac{L}{p_\alpha} \left(\frac{\partial p_\alpha}{\partial z} \right), \tag{4.17}$$

and L the total length of the discharge. This quantity is called the segregation depth in analogy with the optical depth. If the segregation depth is much smaller than unity ($\tau << 1$) the plasma is homogeneously mixed. The situation with $\tau >> 1$ corresponds to a situation with large axial segregation.

Figure 4.7 shows τ as a function of the total lamp pressure for both the dysprosium and the sodium models. Dysprosium MH lamps show the largest τ value at approximately 7 bar, a lower pressure than the sodium containing discharges. Additionally, the maximum τ value of the dysprosium MH lamp is smaller than that of the sodium MH lamp. This difference in the location of the maximum τ value is due to diffusion coefficients shown in figure 4.8. The
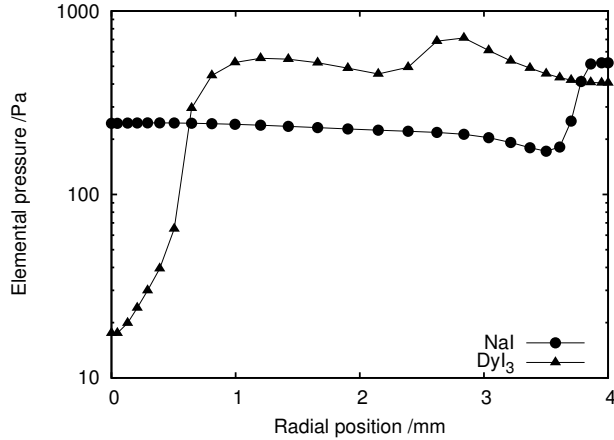
Figure 4.6: Midplane elemental pressure of the metal additive in a sodium MH lamp, compared to a dysprosium MH lamp. Note the strong central dip in the dysprosium MH lamp.

sodium atoms are smaller and diffuse more readily than the dysprosium atoms. This means that greater convection is needed to obtain the same ratio between convection and diffusion.

To quantify the ratio between axial convection and radial diffusion we introduce the Peclet number Pe:

$$Pe = \frac{R^2 V_z}{L D_\alpha},\tag{4.18}$$

with R the radius of the discharge and V_z the axial convection speed. The effective diffusion coefficient D_α from equation (4.14) is evaluated on the axis halfway between the electrodes, as is the axial convection speed. Figure 4.9 shows the average axial segregation as a function of the Peclet number. The Peclet number at which τ has a maximum is the same for dysprosium and sodium. This shows that the Peclet number provides a useful scaling law. The two curves are different in that the maximum τ value is smaller in dysprosium than in sodium. The reason for this difference is examined in the next section.
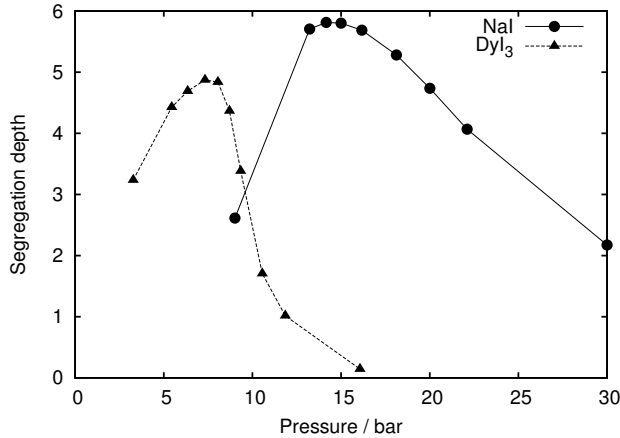
Figure 4.7: Dimensionless segregation depth as a function of lamp pressure for a dysprosium MH lamp compared with sodium MH lamp results from chapter 3.

4.5.2 Convection

The convection patterns in the lamps studied are also altered by the additives. This is demonstrated in figure 4.10 which shows the axial convection through the midplane 4.10. The mercury lamp shows a slightly larger convection speed than the sodium lamp due to the hotter centre. The reason for this hotter centre is the less effective radiative cooling of the mercury plasma due to the absence of strong radiators. The dysprosium causes the arc to contract, leading to an even hotter centre, and thus even stronger convection. Figure 4.11 shows the axial convection compared to the location of the molecules, atoms, and ions in the dysprosium MH lamp. Note that the area with downward convection contains mostly molecules. The transition to atoms occurs in a position where the net flow is towards the top of the lamp. The point of transition is also the point where the gradients of the partial pressures of atoms and molecules are largest. In a sodium lamp, as shown in figure 4.12, the transition from molecules to atoms is much closer to the walls. This means that the downward flow near the walls contains more atoms than in the dysprosium discharge. Molecules are not present in the upward flow. Thus, axial segregation is more pronounced in the sodium containing discharges than in the dysprosium containing discharges.
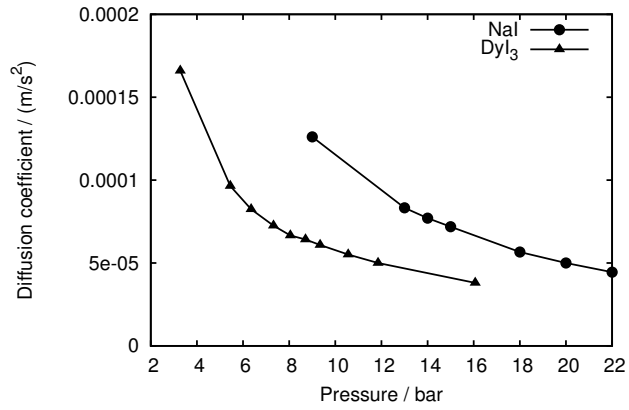
Figure 4.8: Diffusion coefficient on the axis halfway between the two electrodes for dysprosium and sodium atoms compared.

This difference explains the difference in the segregation depth at the same Peclet number found in figure 4.9.
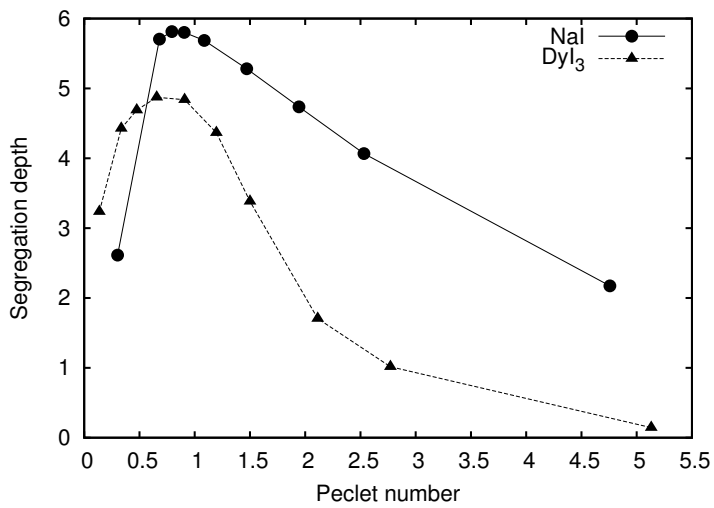
Figure 4.9: Dimensionless segregation depth as a function of the Peclet number for a dysprosium MH lamp compared with sodium MH lamp results in chapter 3.
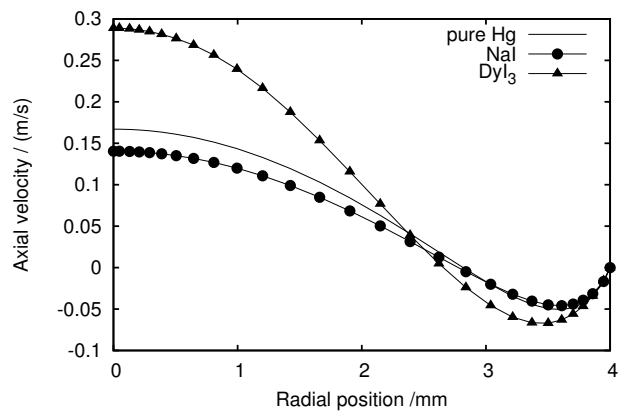
Figure 4.10: Axial convection through the plane halfway between the two electrodes. The difference between the lamps containing dysprosium and the lamp containing sodium is substantial. The lamp containing pure mercury has a slightly higher convection speed than the sodium lamp due to the hotter centre.
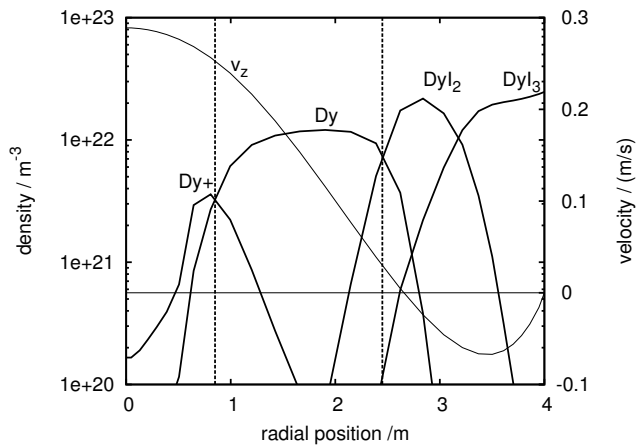
Figure 4.11: The transition from molecules to atoms and from atoms to ions in a dysprosium MH lamp compared with the axial velocity. The relevant transitions are indicated with the dotted vertical lines. Note that transition from molecules to atoms occurs in the upward directed flow.
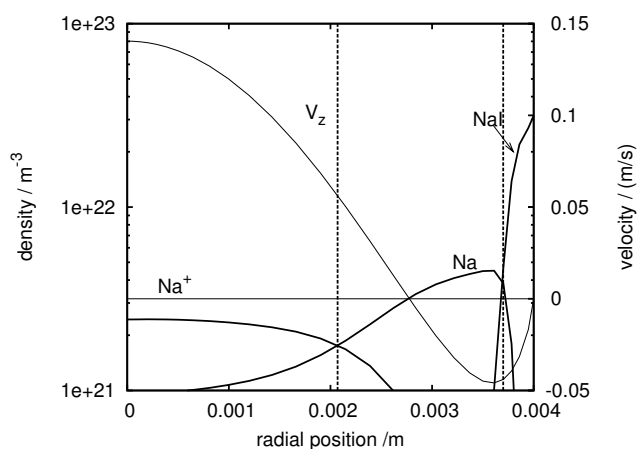
Figure 4.12: The transition from molecules to atoms and from atoms to ions in a sodium MH lamp compared with the axial velocity. The transitions are indicated with the dotted vertical lines. Note that the transition from molecules to atoms is closer to the wall than in the dysprosium MH lamp.
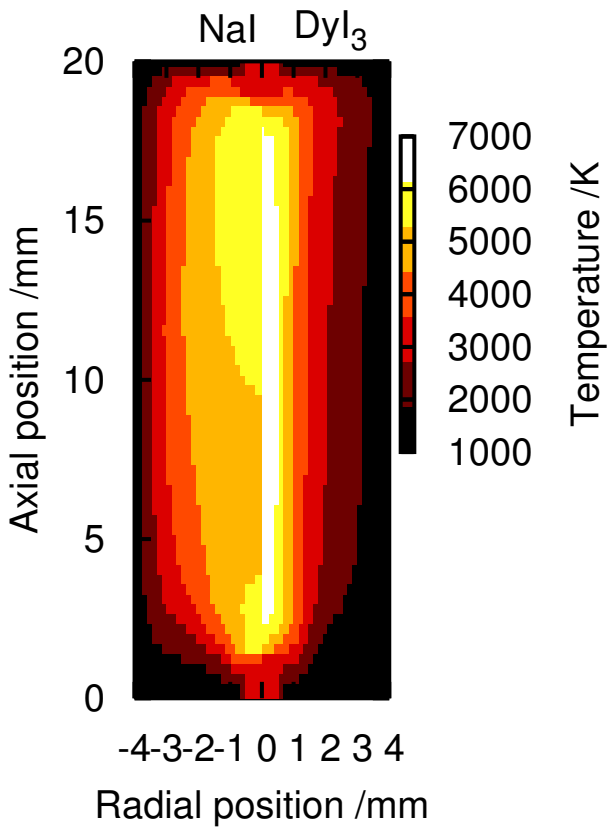
Figure 4.13: The temperature of a dysprosium MH lamp compared with a sodium MH lamp. Both lamps have a total mercury filling of 20 mg and are driven with a power of 135 W.
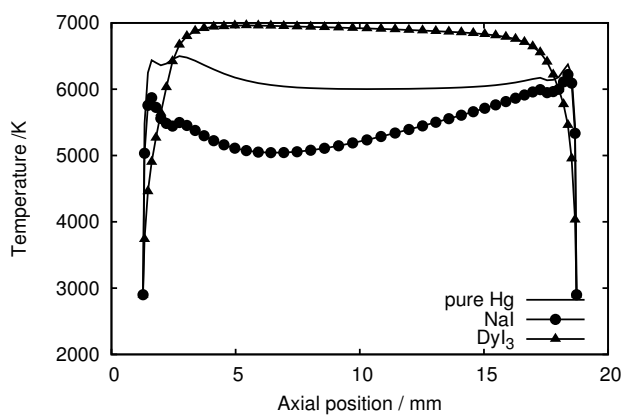
Figure 4.14:   Temperature on the axis of a pure mercury lamp, a sodium MH lamp and a dysprosium MH lamp compared. All lamps have a total mercury filling of 20 mg and are driven with a power of 135 W.
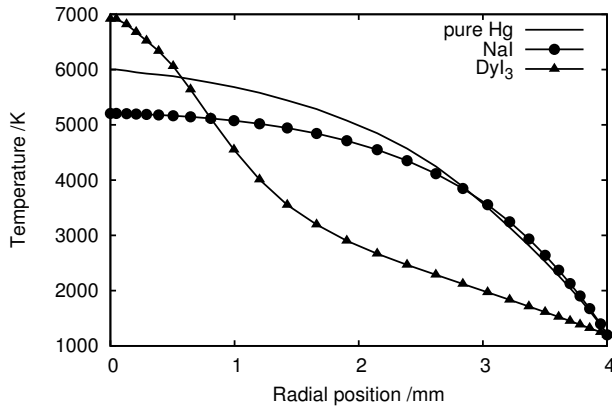
Figure 4.15: Comparison of the temperature midplane between the two electrodes for a pure mercury lamp, a sodium MH lamp and a dysprosium MH lamp. All lamps have a total mercury filling of 20 mg and are driven with a power of 135 W.

4.5.3 Temperature

All quantities in the LTE model are connected to the temperature distribution. The convection speed, in particular is driven by the large temperature difference between the wall and the hot centre. The dysprosium lamp shows less axial segregation than the sodium lamp. This has an effect on the axial temperature profile shown in 4.14. The temperature of the dysprosium MH lamp varies little along the axis while the sodium containing discharge is much hotter at the top than at the bottom. This is because little to no sodium is present near the top electrode. Thus, in the sodium containing discharge, the temperature near the top electrode approaches that of a pure mercury discharge. Additionally, the presence of dysprosium causes the arc to contract. This is because a lot of radiation is released just off-centre where most excited atoms are present. The centre contains few atoms and the mercury ions push the dysprosium ions out of the centre, leading to the strong central dip shown in figure 4.6. The central temperature must be higher than in a pure mercury lamp to still allow sufficient current to pass through the plasma. For comparison, the temperature of a pure mercury discharge is also shown in figure 4.14.

The midplane radial temperature profiles in figure 4.15 show the contraction most clearly. The pure mercury lamp has a parabolic temperature profile. The sodium MH lamp is slightly flattened, and the dysprosium MH lamp shows strong contraction. The dysprosium MH lamp shows the hottest central temperature, followed by the pure mercury lamp and the sodium MH lamp has the lowest central temperature.

4.6 Conclusions

Using PLASIMO a model of an MH lamp based on a mixture of dysprosium iodide and mercury has been built. The chemical composition has been calculated using the Gibbs minimisation approach. From this chemical composition the dominant species have been determined. Comparison with earlier results shows that the pressure for which the axial demixing is most pronounced is lower in lamps containing dysprosium than in lamps containing sodium additives. This is because the dysprosium atoms move less easily through the background mercury gas and have lower diffusion coefficients than the sodium atoms. The maximal axial segregation of the dysprosium lamps is slightly smaller than the of the sodium containing discharges. The reason for this is that the temperature required to fully dissociate the dysprosium tri-iodide molecules is higher than the temperature to dissociate the sodium iodide molecules. Additionally, the dysprosium additives cause strong contraction in the arc. Thus, the molecules dissociate further away from the walls with molecules not only dragged down by convective flows near the walls, but also pushed upwards.

The temperature profiles of a lamp containing dysprosium additives differ much from the temperature profiles of a lamp containing sodium. This is because of radiative cooling of atomic dysprosium, just off-centre. The central part of the discharge contains little to no dysprosium and is thus less effectively cooled. To allow enough current through the lamp the central temperature must be greater than in a pure mercury lamp. Another difference occurs from the depletion of additives near the top of the sodium containing lamp. The part of the discharge devoid of additives approaches the temperature of a pure mercury discharge.

The Peclet number, defined as the ratio of axial convection to radial diffusion may be used to predict the conditions under which axial segregation is greatest. Radial segregation plays a central role in the development of axial segregation. The position at which the molecules dissociate to form atoms has an important influence on the degree of segregation. When molecules dissociate in the part of the lamp where the convection current moves downward the axial segregation is more pronounced than when they dissociate further from the walls, into the radial position where the convective flows are towards the top of the lamp.

Chapter 5

Radiation

Abstract. The radiation emitted by a lamp containing mercury and dysprosium additives is studied. Dysprosium has a spectral "grass field" with hundreds of lines, which are mostly optically open under the conditions studied. Mercury emits radiation on a small number of lines which may be optically open, closed or in between, depending on the exact conditions. We introduce effective transitions for the radiation emitted by the dysprosium additive. These effective transitions are used in combination with ray tracing to model the radiation transport of resonant and partially absorbed mercury lines. The errors introduced by using effective transitions instead of simulating all known transitions is studied through a number of simple case studies. The effective dysprosium transitions are then used in a self consistent model of a metal halide lamp. The choice of data set has a significant impact on the result. Using the data from Gorschkov et al leads to stronger arc contraction than using the more recent data from Wickliffe et al. The distribution of additives is also effected by the choice of input data.

5.1 Introduction

In chapter 2 we presented a study that describes axial segregation in Metal Halide lamps. One of the findings was that increasing the pressure increases convective flows in the lamp. When the convective flows are strong enough the elements become homogeneously mixed, both radially and axially. At low pressures axial demixing is avoided, but radial demixing is still present. The model can be used to predict the range of pressures that should be avoided when designing a lamp. A disadvantage of the model presented in chapter 2 was that the electrodes are approximated by two flat planes.

In chapter 3 we improved the model by taking the shape of the electrode into account. This model with penetrating electrodes was run for a series of conditions and it was found that the electrodes influence convection patterns in the lamp. By changing the convection patterns the competition between convection and diffusion is also changed, and thus also the degree of segregation in the lamp. Not only the competition between convection and diffusion is determinative for the segregation in the lamp. The temperature profile also has some influence. However, this temperature profile is not only determined by the fluid transport processes, the radiation also has a large effect on this profile. Especially the correct treatment of radiation transport deserves attention.

For a part of the spectrum the plasma will be optically thick so that the generated emission is locally re-absorbed whereas for another part radiation can easily escape. For a correct description of both the optical thin and thick radiation we used the method of ray spacing [41].

The models in chapters 2 and 3 were based on MH lamps consisting on a mixture of Hg and NaI. The number of atomic lines in this plasma type is limited. This implies that the ray-trace method can be restricted to a limited number of frequency points.

To compare with experiments the authors have changed the model so that it will work with dysprosium iodide. The primary reason for this is that we wish to compare results with the measurements in [21], which uses, amongst others, the technique of X-Ray Fluorescence (XRF) to measure the elemental densities. This technique works with heavy elements such as mercury and dysprosium but not with sodium. A plasma containing dysprosium additives, however, is more difficult to model than one containing sodium for two reasons:

- A plasma with dysprosium additives has more intermediate molecular species, and these molecules are more complex. To overcome this difficulty we used lookup tables in conjunction with external chemical equi-

librium calculations to calculate the chemical composition of the plasma as described in chapter 4.

- Dysprosium atoms and ions have a large number of radiative transitions. The data set of Wickliffe, Lawler and Nave [44] lists over 900 lines and these represent only the most prominent transitions.

In this chapter we will focus on this last issue. Fortunately, the myriad of spectral lines from dysprosium atoms and ions are, for the relevant conditions, optically open. As will be shown, effective transitions can be used to model the radiative energy emitted by the plasma. This method allows a great reduction in the complexity of the calculation. Before further discussing the use of effective transitions we will first give a general overview of treatment of radiation transport in the model. Then we will investigate the validity of the use of effective transitions via simple test models. We will conclude with results from a full calculation employing these effective transitions for two different sources of data.

5.2   Model description

In this section we give a short overview of the treatment of radiation transport in the model and its interaction with the calculation of fluid properties. The model solves conservation equations to obtain the temperature, velocity and additive distribution in the lamp. More details are found in chapter 2. A schematic view of the geometry and grid used is given in figure 5.1.

5.2.1   Energy balance

All modules come together in the energy balance to calculate the plasma temperature. The temperature, in turn, strongly influences the transport coefficients, composition, flow and radiation. The temperature is given by

$$\nabla \cdot (C_p \vec{u} \nabla T) - \nabla \cdot (\lambda_c \nabla T) = P - Q_{rad}, \tag{5.1}$$

where C_p is the heat capacity at constant pressure, λ_c the thermal conductivity, Q_{rad} the net radiated power [1] and P the Ohmic dissipation. To obtain boundary conditions for equation 5.1 a cold spot temperature of 1100 K is assumed, with

---

[1]Note that in this work Q_{rad} is defined such that it is positive if more radiation is emitted than absorbed, contrary to the convention employed in [41].
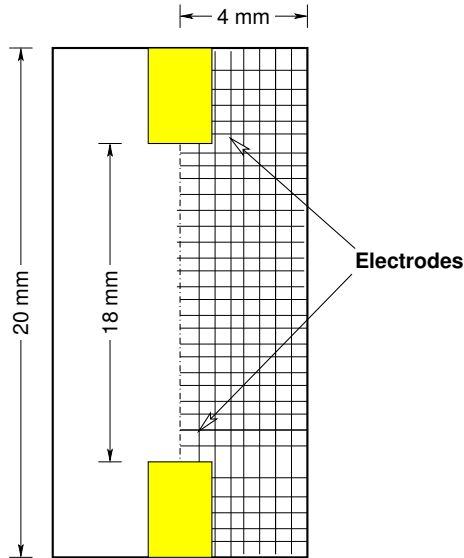
Figure 5.1: Schematic view of the geometry of the problem (not to scale) and the finite volume grid used. The actual grid used is less coarse than suggested in this figure. The computation grid has 66 cells in the axial and 28 cells in the radial direction.

the cold spot located in the bottom corner of the lamp. The electrodes are assumed to have a surface temperature of 2900 K and the rest of the wall a temperature of 1200 K.

5.3   Radiation transport

The term represented by Q_{rad} in (5.1) is the primary focus of this chapter. It is the net result of local emission and absorption at every point in the plasma. To calculate the net radiated power we need to consider the energy gained by absorption of light emitted elsewhere and the energy lost by light emitted locally at each point in the plasma. Since emission and absorption are strongly frequency dependent we also need to do this for a large number of different frequencies and integrate over frequency space.

The net radiated power is related to the radiation intensity I_ν by [41]:

$$Q_{rad} = \int_\nu \left(4\pi j_\nu(\nu, \vec{r}) - \int_{4\pi} \kappa(\nu, \vec{r}) I_\nu(\nu, \vec{r}) d\Omega \right) d\nu, \qquad (5.2)$$

with ν the frequency, $j_\nu(\nu, \vec{r})$ the local emission coefficient and $\kappa(\nu, \vec{r})$ the local coefficient for absorption along rays passing through the discharge. Note that the subscript ν is used to denote a quantity per unit of frequency.

The radiation intensity I_ν is determined by [41]

$$\frac{dI_\nu}{ds} = j_\nu - \kappa I_\nu. \qquad (5.3)$$

5.3.1 Ray tracing on a structured mesh

To solve equation (5.3) we use the method of ray tracing, as outlined in [41]. This method was originally implemented for discharges with two degrees of symmetry. The code has since then been modified to describe two dimensional plasmas with only rotational symmetry. We will briefly outline our ray tracing method following [41] and discussing the modifications implemented.

Radiation transport in plasmas is essentially non-local: every point in the plasma may absorb photons from any other point in the plasma. This stands in contrast with other fluid properties of which the transport can be handled locally. That is, these properties, such as the density or the temperature, depend only on the local value and the local gradients. The finite control volume method works well for such local properties: the temperature in a control volume, for example, is assumed to be influenced only by the control volumes in the direct neighbourhood. The plasma properties are defined on the nodal points. Transport, or fluxes, of conserved properties, take place through the surfaces of the cells.

The Ray Tracing Control Volume RTCV method describes the interplay between the local properties of the fluid and the non-local radiation by combining ray tracing for the radiation transport with finite control volumes on structured meshes for the fluid properties.

Ray tracing describes the intensity of the radiation by calculating this intensity along a series of probe lines through the plasma. This is done by integrating (5.3) along the probe lines. By clever use of the presence of symmetry the number of probe lines may be limited. The local emission and absorption along each segment of the ray is determined from the fluid property in the control volumes through which the ray passes. The RTCV method consists of a number of steps.

1. The choice of probe lines which follows from the symmetry of the problem. This step does not need to be repeated during the iterative solution procedure as long as the grid remains the same.

2. The integration of (5.3) along each probe line. The coefficients j_ν and κ along each segment of the probe line are given by the fluid properties in the control volume through which the probe line passes.

3. The calculation of the radiative fluxes through the boundaries of each control volume given the intensity and the solid angle carried by the rays. The net radiated power Q_{rad} follows from the difference in the radiative fluxes through the boundaries.

4. The calculation of fluid properties on the CV mesh given Q_{rad}. From this step new values of j_ν and κ follow.

5. Test for convergence, if convergence is not reached go back to step 2.

5.3.2 The choice of probe lines

The MH lamps under study are assumed to be rotationally symmetric. This rotational symmetry may be exploited in the choice of probe lines. In particular, the set of probe lines originating from a point may be re-arranged into a set of parallel lines, or chords, as shown in figure 5.2. The one dimensional code used a single parallel set of chords as the coefficients j_ν and κ are independent of the axial coordinate in the one dimensional case. To account for the dependence on the axial coordinate the code has been modified by using sets of parallel rays at multiple angles to the axis (21 different angles are used in practice) for each axial position in the grid. We chose an uneven number of angles with the axis so that we do not have rays parallel to the axis. A schematic representation is given in figure 5.4.

5.3.3 Integration along the probe lines

After choosing a suitable set of rays through the plasma the intensity is calculated by integrating (5.3) along these rays: [50, page 10]

$$I_\nu(\vec{r}, \vec{\Omega}) = \int_0^\infty j_\nu(\vec{r} - s\vec{\Omega}) \exp\left(-\int_0^s \kappa(\vec{r} - s'\Omega)ds'\right) s. \qquad (5.4)$$

The cylindrically symmetric control volume grid discretizes the plasma into concentric cylinders. The coefficients j_ν and κ depend on plasma parameters
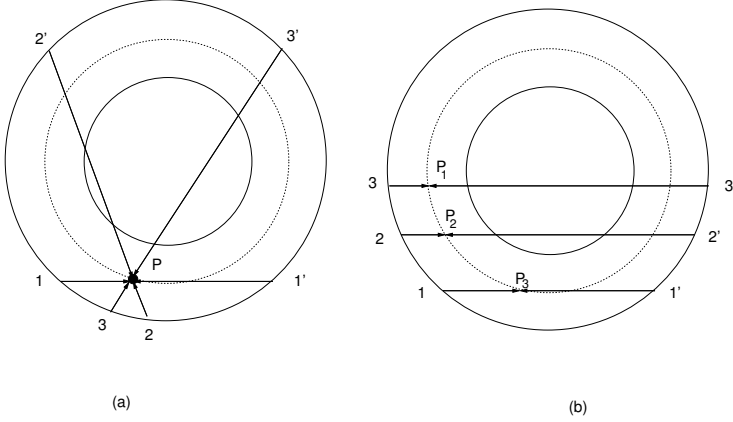
Figure 5.2: Ray tracing with rotational symmetry. Probe lines originating from a point P may be re-arranged into a set of of parallel lines through points P_1, P_2 and P_3.

defined on the nodal points and assumed to be constant for the entire volume of the cell. The rays intersecting these control volumes are discretized into segments. The length of the segment of probe line i passing through the control volume a distance r_j from the axis is denoted $\Delta s_{i,j}$. From simple geometrical considerations, as shown in figure 5.3, it follows that :

$$\Delta s_{i,j} = \begin{cases} \left(\sqrt{R_{i+1}^2 - r_i^2} \right) / \sin(\alpha) & i = j \\ \left(\left(\sqrt{R_{j+1}^2 - r_i^2} \right) - \left(\sqrt{R_j^2 - r_i^2} \right) \right) / \sin(\alpha) & i \neq j \end{cases} \quad (5.5)$$

with α the angle with the axis of the cylinder.

The increase in intensity I_ν is given by:

$$\Delta I_\nu = \left(\exp(-\kappa \Delta s) - 1 \right) \left(I_\nu - j_\nu / \kappa \right). \quad (5.6)$$

To calculate I_ν everywhere along the ray the code starts on the outside of the lamp where $I_\nu = 0$ and integrates through to the other side of the lamp adding ΔI_ν at each step.

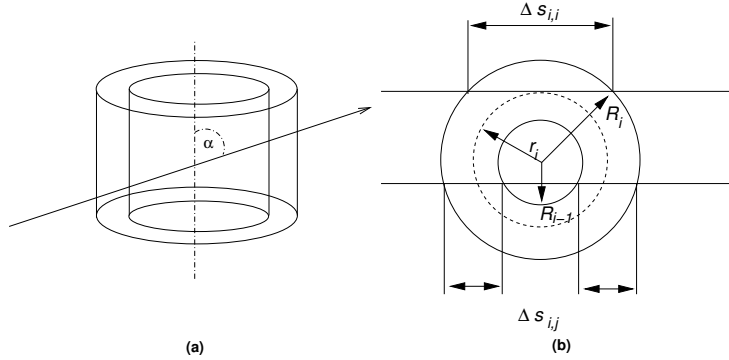Figure 5.3: The length of the line segment through a control volume cell. Figure (a) shows a three dimensional view of a single ray at an angle α to the axis. Figure (b) shows two rays, one passing through a control volume only once, and one crossing the same control volume twice.

5.3.4 Radiative fluxes

After integrating along each probe line the intensity I_ν along the probe lines is known. From this intensity the radiative fluxes through the walls of the control volume boundaries can be calculated. The radiative flux through the boundaries is given by the intensity and the surface area of the cell.

In general terms, the radiative flux through a surface with area A and normal $\vec{n}$ by a beam with solid angle $d\vec{\Omega}$ is given by [41]:

$$\Phi_\nu^\varepsilon = A\vec{n} \cdot d\vec{\Omega} I_\nu. \tag{5.7}$$

In the case of our cylindrical control volume grid the discretized form of the above equation becomes:

$$\Phi_\nu^\varepsilon = 2I_\nu \frac{dy}{rdr} \sin^2 \alpha \, d\alpha, \tag{5.8}$$

with dy the distance between chords in the plane, as shown in figure 5.4.

The term Q_{rad} follows from the difference in the flux of radiation on the cell boundary points:

$$Q_{rad,\nu} = \frac{1}{V} \left(\Phi_\nu^\varepsilon(s + ds) - \Phi_\nu^\varepsilon(s) \right), \tag{5.9}$$

with Φ^{ε}_{ν} the radiative flux and V the volume of the cell.

The current design of the RTCV code is a direct evolution from the original spherically symmetric ray tracing code by Van der Heijden [41]. In this, original design, the decision was made to calculate the radiative fluxes through the walls of the control volumes instead of directly calculating Q_{rad} on the nodal points from the intensity. In the case of point symmetry the approach of calculating the fluxes first and then the net radiated power is more accurate for reasons outlined in [41]. In principle, it is also possible to calculate Q_{rad} directly on the nodal points of the grid, as also outlined in [41]. This latter approach would, in some ways, be more flexible than the current method. Future plans include refactoring the current code to be more general in terms of the geometry of the problem.
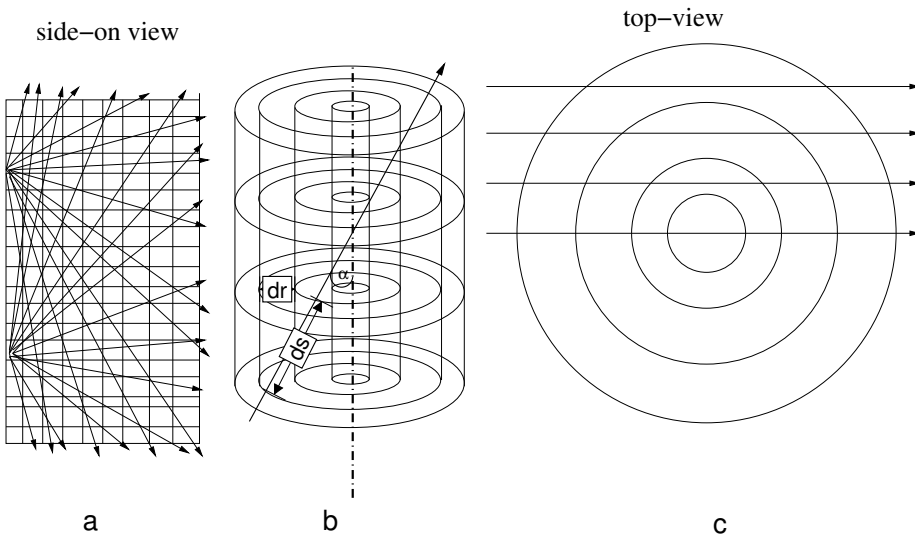
Figure 5.4: Schematic representation of ray tracing on the two dimensional cylindrically symmetric grid. Viewed from the top (c), the projections of the rays follow chords through the cylinder interspaced with distance dy. These chords are repeated at each axial grid position for a number of different angles with respect to the axis, as shown in the schematic of the side-view (a). The side view shows just two sets of rays for the central chord to minimise clutter. Also shown is a single ray passing through the concentric cylinders which make up the finite volume grid (b).

5.4 Ohmic heating

The power to the plasma is supplied by Ohmic heating $P = \sigma E^2$. We solve the Poisson equation in the form:

$$\nabla \cdot (\sigma \nabla \Phi) = 0, \qquad (5.10)$$

with Φ the potential ($\nabla \Phi = -\vec{E}$). The boundary conditions are formed by constant Dirichlet conditions of 100 V on one electrode and 0 V on the other electrode. The upper value of 100 V is adjusted in an iterative manner to arrive at an integrated power dissipation of 130 W. The current through the walls is zero. Thus on these boundaries a homogeneous Neumann boundary condition is used.

$$\vec{J} \cdot \vec{n} = \sigma \nabla \Phi \cdot \vec{n} = 0. \qquad (5.11)$$

In an area a distance of 0.5 mm around the electrodes the conductivity is adjusted to compensate for non-LTE effects. This is necessary since the electron density near the electrodes will deviate significantly from the values expected from chemical equilibrium. High temperature electrons travel to the electrodes, leading to electron temperatures and densities approaching those of the hot spot just in front of the electrode. Thus, the actual electrical conductivity will be close to the electron conductivity in the hot plasma near the cathodes, and not equal to the conductivity calculated by the assumption of LTE. Not correcting for the increased conductivity at the electrodes would effectively couple all the electrical energy in the first layer of cells near the electrodes, overestimating the temperature in these cells, while underestimating temperature elsewhere. A correction is made by imposing a minimal conductivity in a small area around the electrode of 40 Ohm/m. This value corresponds to the electrical conductivity at 4000 K.

5.5 Effective transitions

Adding dysprosium to a plasma results in a spectral "grass-field". We will investigate to what extent this myriad of lines can be approximated by a single formula describing the net radiated power how this will effect the temperature distribution and how this will lead to different temperature profiles and thus to different convection patterns and additive distributions. From previous studies we know that for dysprosium containing MH lamps a large part of the radiation is generated by dysprosium atoms (Dy I) and dysprosium ions (Dy II) lines and

that most of this radiation can freely escape from the plasma. Throughout this paper we will assume that within an atomic (or ionic) system the levels are populated according to Boltzmann. We will at first consider Dy I and Dy II as separate systems, and then study the result of the two combined. In particular, we will study the radiated power per particle (RPP) in each system. First we calculate the RPP using transition probability data from literature. This is done using two different literature sources: [44] and [51] and for the systems DyI and Dy II separately. We will show that the effect of literature source-selection on the plasma shape is substantial. To enable a more systematic study of the effect of the RPP and the impact of the different sets of transition probability sources analytical fit functions of these RPP will be presented.

To this end we examine the error made by approximating Q_{rad} by a limited number of optically thin transitions. This is done through three case studies:

1. a sphere at a uniform temperature containing dysprosium vapour,

2. a sphere containing both mercury and dysprosium at a uniform temperature and

3. a cylinder with a radially dependent temperature profile and an axially varying dysprosium concentration.

In the case of optically thin transitions, radiation presents a simple local energy loss term to the energy balance of the plasma. This is the case for a frequency ν if the optical depth at that frequency $\tau(\nu) = \int \kappa(\nu)ds$ is much smaller than unity. In this case, we may ignore absorption so (5.3) becomes

$$\frac{dI_\nu}{ds} = j_\nu = (h\nu/4\pi)n_u A_{ul}\phi_{ul,\nu}(\nu), \qquad (5.12)$$

with n_u the density of the upper state, A_{ul} the transition probability and $\phi_{ul,\nu}$ a normalised line broadening profile $\int_0^\infty \phi_{ul,\nu}d\nu = 1$.

In the following the ion and atoms systems are treated separately. If the emitting system has an internal Boltzmann energy distribution with temperature T, the density of the upper level is given by the Boltzmann balance for excitation [31]

$$n_u = \frac{n_S g_u}{Q_S} \exp\left(-\frac{E_u}{kT}\right), \qquad (5.13)$$

with n_S the density and Q_S the partition function of the atomic or ionic system. The partition function is given by

$$Q_S = \sum_p g_p \exp\left(-\frac{E_p}{kT}\right) \qquad (5.14)$$

with g_p the degeneracy of level p. The summation runs over all levels in the system. In theory, the number of levels is infinite. To calculate the partition function a cutoff is required. We simply limit the sum to the highest upper level from which a radiative transition is in the dataset.

5.5.1 Radiated power per particle

We will now examine the RPP in each system. The energy radiated is given by integrating over the frequency spectrum for all transitions.

$$Q_{rad} = \int \sum_u \sum_l (h\nu_{ul} n_u A_{ul} \phi_{ul,\nu}(\nu))\, d\nu. \tag{5.15}$$

If no radiation is absorbed this is equivalent to the summation over all transitions without line broadening. Making use of (5.13) we obtain

$$\frac{Q_{rad}}{n_S} = \sum_u \frac{g_u}{Q_S} \exp\left(-\frac{E_u}{kT}\right) \sum_l A_{ul} h\nu_{ul}. \tag{5.16}$$

This quantity is the RPP, which we will seek to replace with a simple approximation. We replace (5.16) with an effective transition, as given by

$$\frac{Q_{rad}(T)}{n_S} = A_{eff}\Delta E_{eff} \exp\left(-\frac{\Delta E_{eff}}{kT}\right). \tag{5.17}$$

The parameters ΔE_{eff} and A_{eff} are free fit parameters. We calculate the RPP for fixed system densities and temperatures between 1000 K and 7000 K using equation (5.16). The parameters ΔE_{eff} and A_{eff} are then determined by a least squares fit through the results. Results of using the double sum in (5.16) on data from [44] are shown in figure 5.5. The best fit of the single expression (5.17) for ΔE_{eff} and A_{eff} is also shown in the same figure. The corresponding values thus obtained are $A_{eff} = 1.21 \times 10^8$ Hz for the atoms and 1.43×10^8 Hz for the ions. The resulting effective energies are 2.279 eV for the atoms and 2.292 eV for the ions.

In the following subsections the case studies mentioned earlier will be studied. In the case studies the radiated power is determined by use of the effective transitions just derived and compared with results from the full set of data. All the case studies assume that the plasma is in LTE. Thus, the radiation emitted is fully determined by the elemental composition and temperature in the
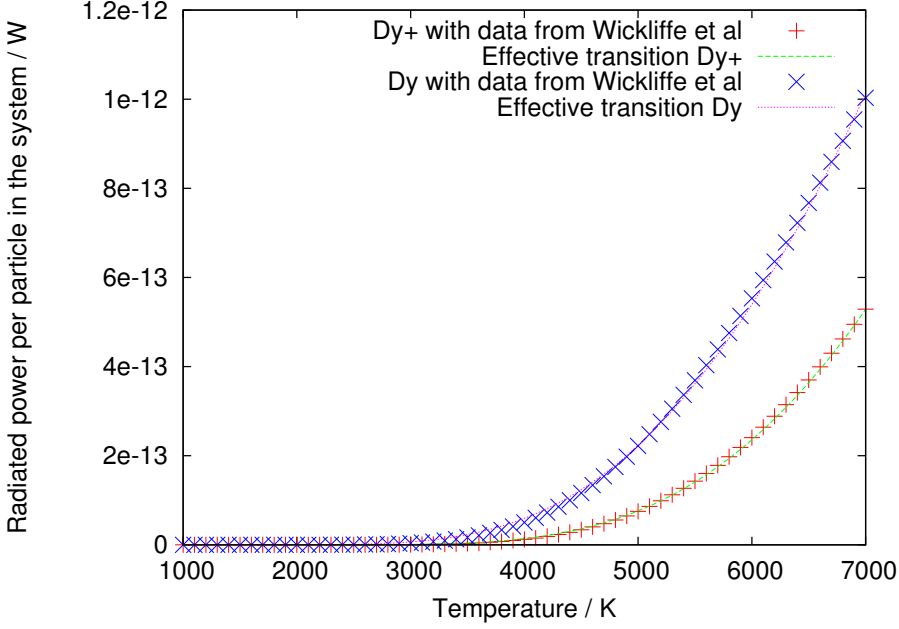
Figure 5.5: Radiated power per particle for both the dysprosium atom (Dy I) and dysprosium ion (Dy II) systems. To calculate the energy loss the densities of the ground state where fixed and a Boltzmann distribution of the excited states was assumed. The free parameters from equation (5.17) are determined by fitting this equation through the results. The result of this fit is also shown in figure 5.5. The resulting fit yields an effective transition probability of 1.21×10^8 Hz for the atoms and 1.43×10^8 Hz for the ions. The resulting effective energies are 2.279 eV for the atoms and 2.292 eV for the ions.

plasma. The distribution of dysprosium over the two systems is determined by the Saha balance,

$$\frac{n_e n_{Dy+}}{2 n_{Dy}} = \frac{Q_{Dy+}}{Q_{Dy}} \left(\frac{2\pi m_e kT}{h^2} \right)^{\frac{3}{2}} \exp\left(-\frac{E_i}{kT} \right), \qquad (5.18)$$

5.5.2 Sphere filled with dysprosium

The first case study is formed by regarding the radiation emitted by a sphere of dysprosium vapour at a uniform temperature, where the plasma may be regarded as optically thin. The total dysprosium pressure is fixed at 1000 Pa. The distribution over the ion and atom systems is determined by the Saha balance, with the partition function calculated from the atomic levels from [44]. The electron density is determined by assuming quasi-neutrality $n_e = n_{DyII}$. Only dysprosium atoms, singly ionised atoms, and electrons are considered. The densities thus obtained are shown in figure 5.6.

Figure 5.7 shows the radiation emitted in the first case study. This figure shows the RPP calculate two ways, by use of (5.16) and with (5.17). As expected, the agreement between the two approaches is excellent. Effectively, this case study is the inverse of the procedure which determines the coefficients for the effective transitions.

5.5.3 Sphere with dysprosium and mercury

Using these results in a plasma containing other radiative species is, however, slightly more problematic. Other species, such as mercury, may absorb radiation emitted by dysprosium. To examine the possible error, results are compared again in a second case study for a sphere containing mercury as well as dysprosium. We again look at a sphere of uniform temperature with a volume of 1cm^3 containing dysprosium and mercury. The elemental abundance of mercury is 1,000 times that of a dysprosium . The total pressure is chosen at 10 bar. One dimensional ray tracing is used to calculate the energy loss term for temperatures from 1000 K to 7000 K. Full ray tracing is done on all lines, but for the optically open lines only three frequency points are chosen. The ion densities are given by the Saha balance. The resulting net radiated power is shown in figure 5.8. The match between the effective transition approach and the full data set is again very good at higher temperatures.

5.5.4 Cylinder with dysprosium and mercury

In metal halide lamps the temperature is far from constant. To examine a situation closer to that of a metal halide lamp a third case study will be performed. A parabolic temperature profile

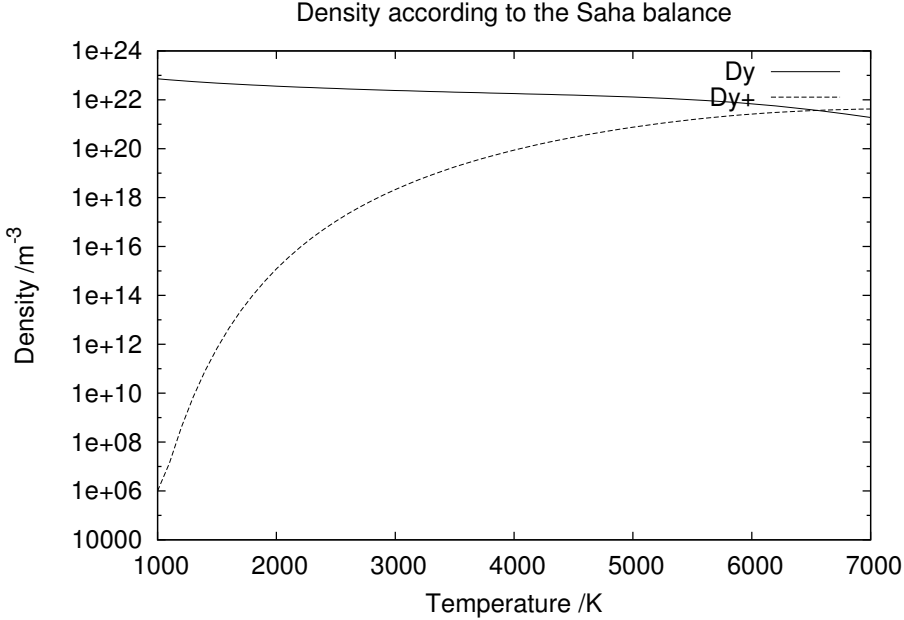$$T(r) = T_{wall} + T_A \left(1 - (r/R)^2 \right). \tag{5.19}$$

Figure 5.6: Densities from the Saha balance as a function of temperature, using the data from [44] to calculate the partition functions. The total dysprosium pressure is 1000 Pa.

is imposed on a cylinder with a radius $R = 5$ mm and a length of 10 mm. The coefficients are $T_{wall} = 1200$ K, $T_A = 4800$ K, The cylinder has an exponentially decaying dysprosium pressure in the vertical direction given by

$$p = p_0 \exp(-z/\Lambda), \tag{5.20}$$

with $p_0 = 150$ Pa and $\Lambda = 9.0$ cm.

The net radiated power is then calculated using two effective transitions, and the complete set of data from [44]. In all cases full two dimensional ray-tracing is used, with three frequency points for the open lines and one hundred frequency points for each mercury line. On a standard desktop computer the calculation with the full data set takes close to one hour. As part of an iterative method this is unacceptable as full calculations would take years to complete.

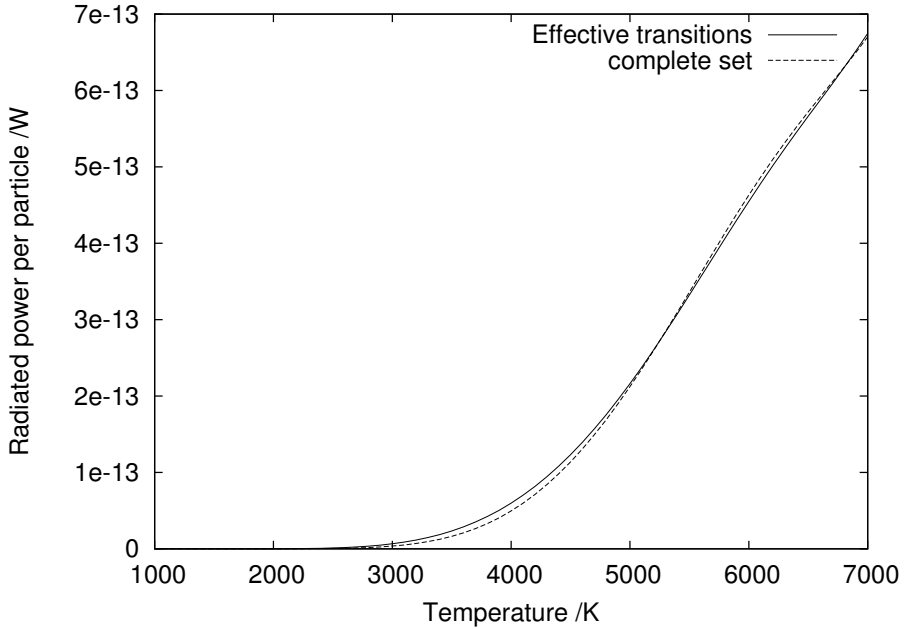The results with the full data set and the effective transitions are shown

Figure 5.7: Radiated power per particle as a function of temperature for two systems, Dy I and Dy II. The distribution of dysprosium over the two systems is determined by the Saha balance using $n_e = n_{DyII}$. The radiation emitted was then calculated using the full set of data from [44] and by effective transitions for the atoms and ions. The energy radiated away has been divided by the total number of particles in the system.

in figure 5.9. As may be expected, agreement, though still reasonable, is not as good as in the previous more artificial examples. The mercury vapour may absorb radiation emitted by the dysprosium atoms or ions, and this has not been taken into account. The differences are small enough, however, to allow the use of the effective transitions to speed up calculations and generate a proper starting point for more accurate calculations if so desired. Alternatively, a number of transitions with frequencies that can be absorbed by the mercury vapour could be added.
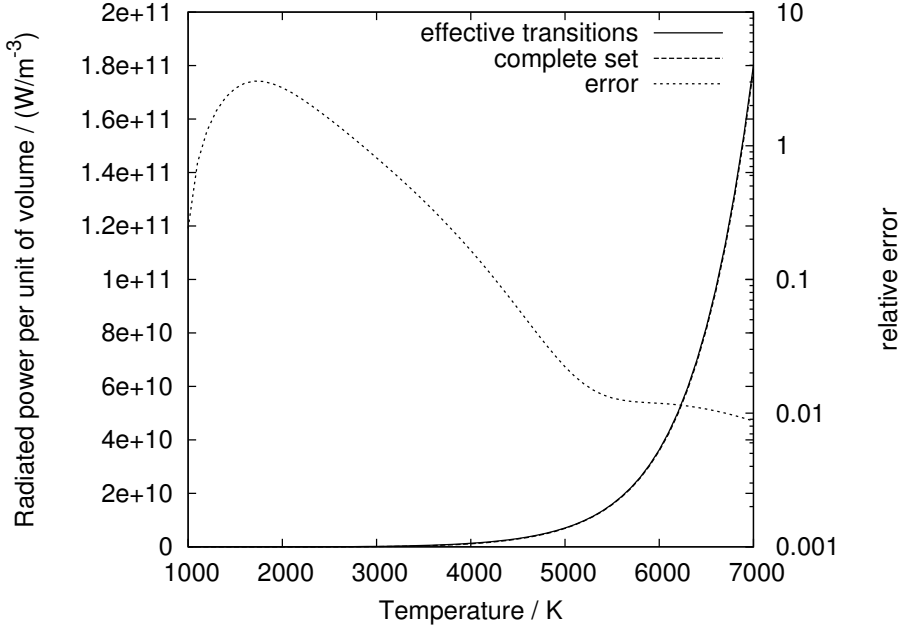
Figure 5.8: Net radiated power by a sphere containing 10 bar mercury and 10 mbar dysprosium in LTE. The solid line shows the result with the radiation emitted by dysprosium calculated through (5.17). The dashed line shows the result using 1 dimensional ray tracing with the data from [44]. As these two lines difficult to distinguish the relative error is also plotted with a dotted line. The relative error is very small at the higher temperatures.

5.5.5 Sensitivity analysis

The last test case was repeated with the values for the effective transition frequencies lowered and raised by fifty percent. As can be seen in the graph, the result is not particularly sensitive to the effective transition probabilities. Raising the transition probabilities for the ion system leads to more emission from the centre of the plasma.

Changing the effective energies has more effect. Figure 5.11 shows the effect of changing the effective transition energies by five percent. Fortunately, the transition energies for the complete system can be measured to an excellent
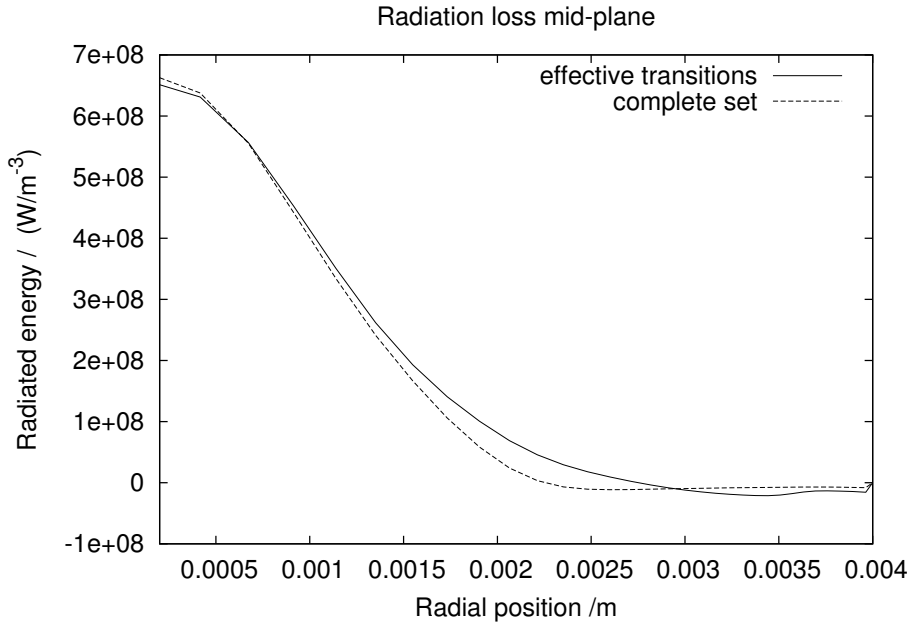
Figure 5.9: Radiative power Q_{rad} mid-plane as a function of the radial position for a cylinder filled with mercury and dysprosium. A radial parabolic temperature profile has been imposed as well as an exponentially decaying dysprosium abundance in the axial direction. Near the axis the match between the effective transitions and the complete calculations is good, but towards the walls where the temperature is lower a mismatch due to absorption becomes apparent.

degree of accuracy.

5.5.6 Choice of data set

As mentioned earlier, other data sets are also available. One of the most widely used, due to its easy availability online is the set from Gorschkov [51] available online via the Kurucz database. This set is much older than the set from Wickliffe et al [44]. We repeated the fitting procedure with the set from [51]. As can be seen in figure 5.12 the choice of data set has a large effect on the estimate of the radiation emitted. The set of lines in [51] is also larger than the set in

Figure 5.10: Radiative power Q_{rad} mid-plane for a cylinder filled with mercury and dysprosium. Three cases are shown: The straight line shows the result with effective transition probabilities determined earlier, the dashed line shows the result with the effective transition probability for the dysprosium atom system increased fifty percent, and the dotted line shows the result with the effective transition probability for the dysprosium ion system increased by fifty percent.

[44]. To test if the radiation in the latter is underestimated by not including many lines with smaller transition probabilities we selected the lines from [51] with a transition probability larger than $1 \times 10^7 \text{s}^{-1}$. As can be seen in figure 5.12 the influence of neglecting these lines is marginal. The difference between the two can only be attributed to differences in the transition probability of the most prominent lines.
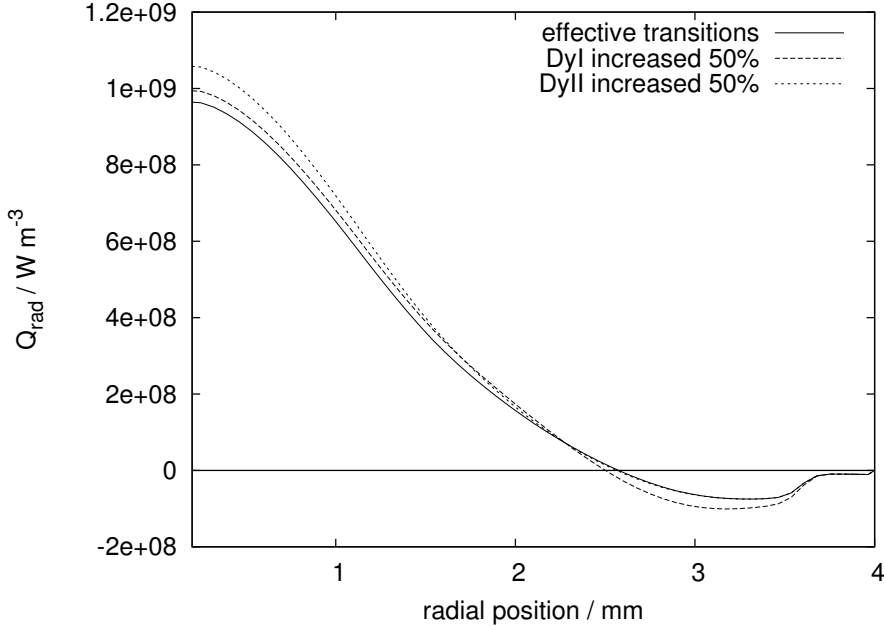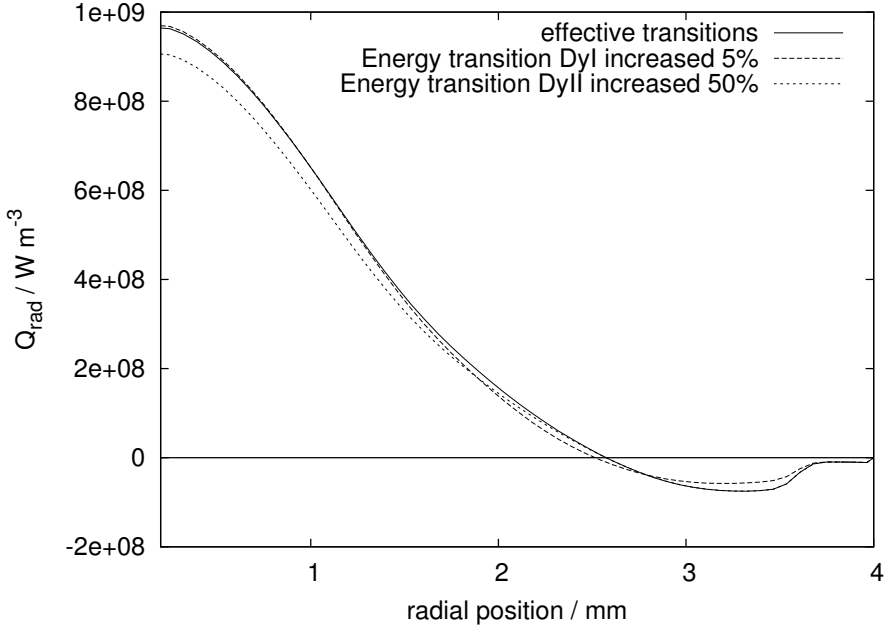
Figure 5.11: Radiative power Q_{rad} mid-plane for a cylinder filled with mercury and dysprosium. Three cases are shown: The straight line shows the result with effective transition probabilities determined earlier, the dashed line shows the result with the effective transition energy for the dysprosium atom system increased five percent, and the dotted line shows the result with the effective transition energy for the dysprosium ion system increased by five percent.

5.6   Results with a self consistent model

Now that we can estimate the RPP of DyI and DyII with a simple analytical expression we will use this expression in a complete self consistent model of the plasma. This allows us to examine the influence of the emitted radiation on the temperature profile, the convective flow and finally on the additive distribution.

The model was run with a total mercury filling of 10 mg, and a power input of 135 W using the effective transitions of [44] and [51].
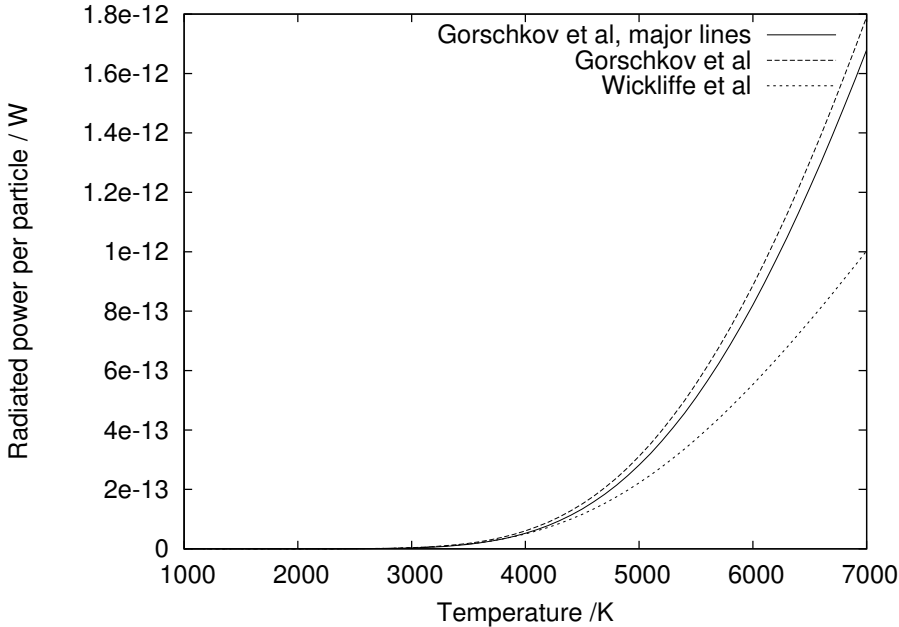
Figure 5.12: The influence of the choice of data set on the RPP. As the figure shows, the influence of the choice of data set is large. Selecting only transitions with a transition probability greater than $1 \times 10^7 \ \mathrm{s}^{-1}$. does not greatly influence the result.

5.6.1 Temperature profile

Radial temperature profiles for two different axial positions can be seen in figure 5.13. The choice of data set has a significant impact on the contraction of the discharge. The contraction is caused by radiative cooling of the flanks, where the largest concentration of excited atoms is found. The ions radiate less energy than the atoms. Additionally, mercury ions in the centre push the dysprosium ions aside, leaving the central region with very low concentrations of dysprosium. The mercury emits less radiation than the dysprosium leading to higher temperatures in the centre. The model fixes, as a real lamp ballast would, the electrical power input into the plasma. A strong arc contraction, therefore requires a higher central temperature to still allow the same current

to flow through the lamp. The difference in the degree of contraction is most pronounced near the bottom of the lamp where the concentration of dysprosium is greater. This is because there is very little dysprosium in the top of the lamp. The reason that the difference is not even greater lies in the strong temperature dependence of the radiated emission. A larger transition probability results in more emission, leading to stronger cooling of the centre of the discharge. This stronger cooling results in a lower temperature to reach a steady state. Because the emission depends exponentially on the temperature, the temperature needs to be only slightly lower to reach a new balance.
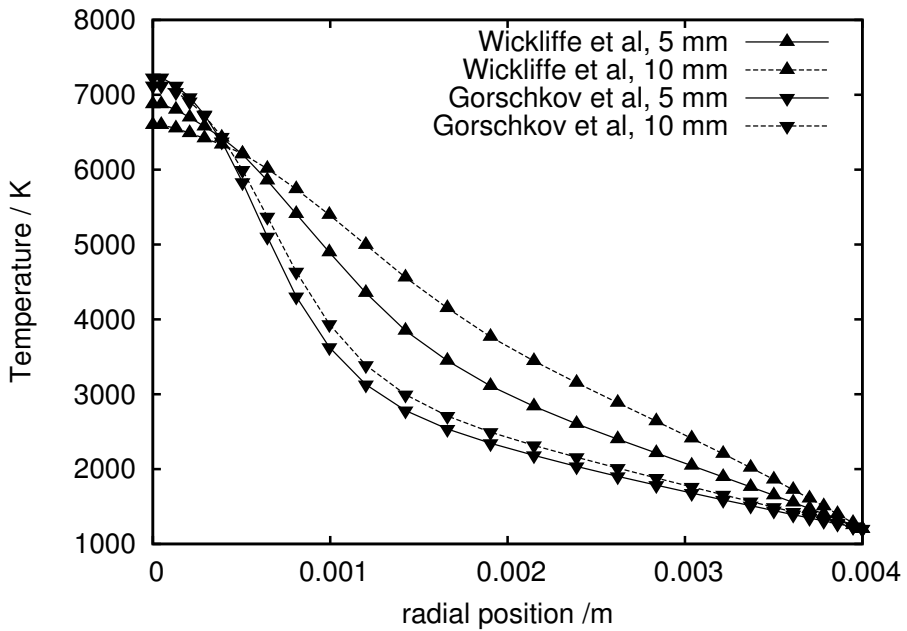

Figure 5.13:   Radial temperature profiles for two axial positions in the lamp: 5 mm from the bottom electrode and midplane. Note the strong contraction.

5.6.2   Additive distribution

The radiation emitted by the lamp primarily effects the temperature distribution. The temperature distribution, in turn, drives the convection in the lamp.

This convection affects the distribution of additives. As is shown in figure 5.14, the effect of the choice of data set on the additive distribution is significant. The use of the data by Gorschkov et al leads to less axial segregation. The radial segregation is also effected, where the model result based on the Gorschkov data shows a local maximum, a local minimum is predicted with the data by Wickliffe et al.

5.7   Conclusion

By using effective transitions for the radiation emitted by dysprosium the model of an MH lamp containing a mixture of sodium and mercury has been modified to simulate a lamp containing dysprosium additives. The effective transitions give an estimation of the radiated power per particle. The accuracy of this estimation is primarily determined by the accuracy of the input data. Errors introduced by this approach are much smaller than the accuracy of the input data. The choice of data set from different literature sources has a large effect on the emission at a fixed temperature. The effect on the predicted temperature is smaller but still significant. Using the more recent data from [44] leads to lower predicted contraction than the older data from [51]. There is an important secondary effect on the distribution of additives; the smaller contraction leads to larger axial segregation with the data from [44] than with the data from [51].
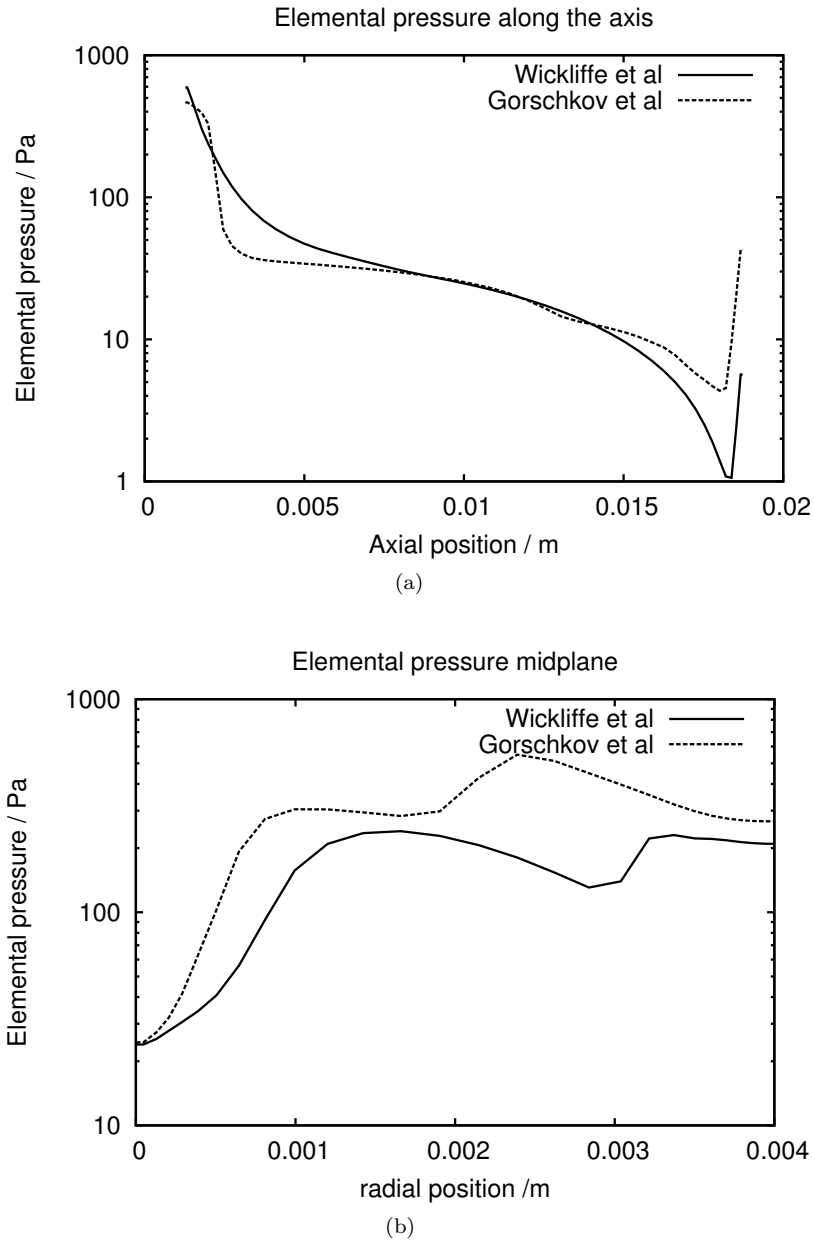
(a)

(b)

Figure 5.14: Elementary dysprosium pressure along the axis (a) and midplane (b) for the two data sets of [44] and [51].

Chapter 6

Comparison with microgravity experiments

Abstract.

The results from optical emission spectroscopy experiments of metal halide lamps under the microgravity conditions on board the international space station are compared with the results of a numerical LTE model constructed with the platform Plasimo. At microgravity there is no convection which allows for easier modelling and for a separate study of the diffusion-induced radial segregation effect, undisturbed by convection. The plasma parameters that were experimentally determined and compared to the model were the Dy atom and ion density, the Hg ion density and the temperature.

The model and experiments applied to a reference lamp burning on a plasma mixture of DyI$_3$ and Hg were found to be in reasonable agreement with each other. The cross-section for electron-Hg collisions was studied, it was found that the Rockwood values give the correct results. Experimental results guided a sensitivity analysis of the model for the Langevin cross-sections. The ratio of the ion densities $n(Hg^+)/n(Dy^+)$ was found to be extremely sensitive for the cross section of the elastic interaction $\sigma(Hg, Dy^+)$ between the Dy ion and the Hg atom. The sensitivity analysis suggests that equating $\sigma(Hg, Dy^+)$ to a value that is 10% higher than the Langevin cross section is the best choice. We also found deviations from LTE in the outer regions of the plasmas for relative radial positions of r/R > 50%.

This chapter is based on a publication submitted on invitation to a J Phys. D. Special issue as *"Metal-halide lamps in microgravity, experiment and model"* with co-authors T. Nimalasuriya, W. W. Stoffels and J. J. A. M. van der Mullen.
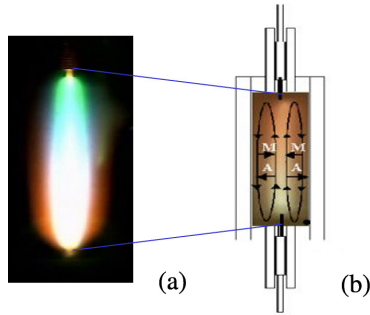
Figure 6.1: (a) Colour separation in an MH lamp burner. (b) Schematic view of an MH lamp; diffusion and convection of atoms (A) and molecules (M) are indicated by arrows.

6.1   Introduction

The metal halide (MH) lamp [25, 52, 53] combines the high luminous efficacy and good colour rendering of the fluorescent lamp with the compact and high-power characteristics of the high-pressure Hg lamps. The lamp contains a rare gas for starting and a Hg buffer gas plus a small amount of metal-halide additives such as DyI_3, TlI, or NaI. Even though the additive density is much less than the mercury density, most light is emitted by the metals in the visible region, which results in a very high power efficiency (up to 40%). However, despite the clear advantages, the growth of the MH lamp has been hampered by a number of limitations. One of these is the segregation of colours [5] caused by the non-uniform distribution of the additives over the lamp due to the competition between diffusive and convective processes, see figure 6.1.

To be able to unravel the complex interaction between convection and diffusion, experiments under microgravity conditions have been performed at the international space station. In absence of gravity, convection is eliminated, so that the effect of diffusion can be studied exclusively and the problem is greatly simplified. The MH lamp in microgravity is therefore easier to model. By comparing the model results to the experiments we can gain insight into the complex transport phenomena in the MH lamp. The experiments verify the model results, whereas the model aids the interpretation of the experimental results. The experiments are part of a poly-diagnostic study [54, 55, 11, 12, 21, 21] of

the MH lamp.

In this paper we present the comparison between the experiments performed on MH lamps under microgravity conditions and a numerical model. The experiments were performed in the microgravity environment of the international space station (ISS). The lamp was investigated by means of optical emission spectroscopy, which yields line intensities of the species Hg, Dy and Dy^+. From the calibrated Hg line intensity measurements we constructed radial temperature profiles. By combining the temperature profile with the calibrated line intensities for Dy we obtained absolute radial density distributions of the Dy and Dy^+ systems. All measurements were done for different powers ranging from 70 to 150 W. The results were reported in [12].

Metal halide lamps come in various shapes and sizes. To be able to compare results of experiments done on MH lamps and to compare the results from models to the experiments a reference lamp has been defined within the framework of the European project COST-529 [9]. The lamp was filled with an Hg buffer gas and one salt, i.e. DyI_3. This lamp has a relatively simple salt system and therefore the results are easier to compare with the results of the numerical model. We base our models on this lamp geometry. The simulation platform used to construct this model is called Plasimo and is described in previous chapters. The model simulated the lamp operating with the following conditions: an electrode distance of 18 mm, a power of 130 W and a Hg pressure of 12 bar.

There are a number of input-parameters that are not well known, such as the vapour pressure of the metal-halide salt at the cold-spot position, the transition probabilities and the cross-sections for the elastic collisions between charged and neutral particles. The latter is found to be determinative for the segregation phenomenon. The sensitivity of the model results for the elastic collisional cross-section for the Dy ion and Hg atom were tested. Because the cross-sections for the elastic collisions between the Dy ion and the Hg atom are unknown, the Langevin cross-section was used. The sensitivity of this approximation is investigated.

This article is organised as follows. Section 6.2 describes the segregation phenomenon. Section 6.3 gives an account of the experiment. Section 6.4 illustrates the model. Results from both experiment and model are presented and discussed in section 6.5. These results include the comparison between model and experiment of the radial profiles of the arc temperature and absolute atomic and ionic densities of Dy. Finally, section 6.6 offers conclusions and recommendations for future work.
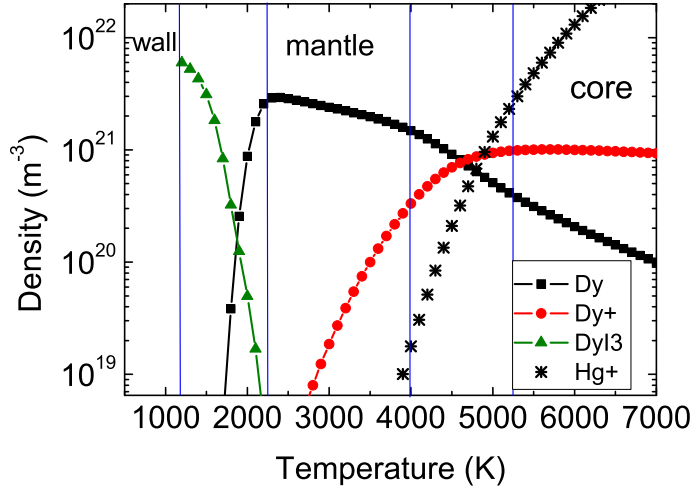
Figure 6.2: Theoretical density distribution of Dy atoms, ions and molecules, and Hg ions as a function of temperature at the midplane of a MH lamp. For clarity, DyI_2 and DyI have been omitted.

6.2 Demixing

When the MH lamp is operated, the Hg is entirely vapourised forming the buffer-gas, whereas the few milligrammes of DyI_3 additive do not evaporate completely, leaving a liquid salt pool at the coldest spot at the burner wall. The additive molecules diffuse from the relatively cool wall (~ 1200 K) toward the hot region (~ 6000 K) of the arc where they dissociate. At the centre the atoms are ionised and excited. As Dy atoms diffuse back to the wall they encounter I atoms in the cooler gas near the walls and recombine back to molecules [52].

Three principal regions can therefore be identified within the radial density distribution of elemental Dy [21] (see Figure 6.2). These are 1) the region near the wall where DyI_3 molecules are predominant, 2) the mantle region between the wall and the arc core where Dy atoms predominate, and 3) the core where the Dy is almost completely ionised in the form of Dy^+. The molecule DyI is

relatively unstable and does not have a dominant presence in any region of the discharge.

When burned vertically, the discharge emits light that is non-uniform in colour along its axis. This colour segregation, is caused by the interplay between convection and diffusion which ultimately determines the distribution of the plasma species. Let's first consider the radial distribution. The temperature profile, which is high in the centre and rapidly decreases towards the wall, leads to a hollow profile for the mass density distribution due to the ideal gas law. Another mechanism that influences the radial distribution of elemental Dy is diffusion. The atoms and molecules have different diffusion velocities. The smaller and lighter Dy atoms diffuse faster outward than the larger and heavier molecules (DyI, DyI_2, DyI_3) diffuse inward. This difference in diffusion velocity results, in steady-state, in an even more hollow profile of the elemental density of Dy; this effect is called radial segregation [5]. Ambipolar diffusion [33], in particular, causes the ions to diffuse out of the core faster than neutral atoms or molecules diffuse inwards.

The axial distribution of the species is dominated by convection, which causes the hot gas to move upwards in the hot centre of the arc and downwards along the cool wall of the lamp. This movement of the bulk gas drags the high concentration of elemental Dy near the wall downwards, whereas the lower concentration of Dy in the centre, caused by the radial segregation, is dragged upwards. As a consequence, a high density of elemental Dy accumulates at the bottom of the arc, a phenomenon which is known as axial segregation [5]. The combination of radial and axial segregation is shown in figure 6.1(b). The latter obviously only occurs in presence of convection. Since there is no convection under microgravity conditions axial segregation does not occur, but radial segregation does.

6.3 The experiment

In the ISS experiment, emission spectroscopy was performed on a MH lamp [9], which is as mentioned above a reference lamp. The lamp consists of a quartz burner of 20 mm in length and 8 mm in inner diameter and a transparent quartz outer bulb. The space between the outer and inner bulbs is vacuum. The burner is made of quartz in order to make the arc optically accessible. The distance between the electrodes is approximately 18 mm. The lamp is driven by a 150 W Philips Dynavision DALI ballast with a 83 Hz square wave current profile, and operated at different input powers ranging from 70 to 150 W in steps of 20 W. In
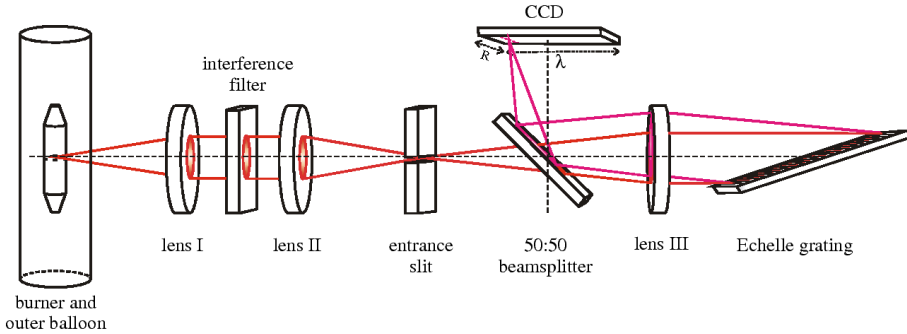
Figure 6.3: Setup used for the ISS measurements. It is an Echelle type spectrometer in Littrow configuration, the imaging lens (III) is used for the collimation of both the undispersed beam of light as well as the reflected dispersed beam of light.

a commercial lamp, the burner is often made of PCA (poly-crystalline alumina). PCA can withstand much higher temperatures, allowing the temperature of the discharge, wall and salt pool to be higher than for a discharge contained by a quartz burner. Therefore, more Dy is expected to be in the discharge in a PCA burner than is the case for burners made of quartz.

An Echelle-type spectrometer was used as there is need for a robust and compact setup with no moving parts for the experiments at microgravity. The downside is that only a few lines could be analysed. A schematic of the Echelle-type spectrometer is shown in figure 6.3 [12]. Its main components are an Echelle grating with a high blaze angle ($74°$), an interference filter for the selection of the desired wavelength interval and a CCD camera for imaging. This spectrometer was used to measure the absolute intensity of three lines of three different systems. These are the 579.07 nm line of the atomic Hg system, and the 642.19 nm and the 402.44 nm line of the atomic and ionic Dy system respectively; shortly denoted by the Dy and Dy^+ system. The Hg line is used for the determination of the radial temperature distribution, and combined with the lines of Dy and Dy^+ the densities of the Dy and Dy^+ systems can be determined.

The procedure is as follows, first the transition-integrated intensity of the line emitting species is determined as a function of lateral position. After Abel

inversion this gives the radiant power of the transition

$$U_{pq}(r) = n_p(r)A_{pq}h\nu_{pq} \tag{6.1}$$

from which, $n_p(\text{r})$, the radial distribution of the radiating level can be determined since the transition probability A_{pq} and the photon energy $h\nu_{pq}$ of the transition are known. The density of the system to which the radiating level belongs can now be determined using the Boltzmann relation

$$n_S(r) = \frac{U_{\text{pq}}(r)Q(T(r))}{g_{\text{p}}A(p,q)h\nu_{pq}} \exp\left(\frac{E_{\text{p}}}{kT(r)}\right), \tag{6.2}$$

where n_S is the system density of an emitting atom or ion, g_{p} the statistical weight of upper level p, $A(p,q)$ is the transition probability of the transition, $h\nu_{pq}$ the energy of the emitted photon, E_p the excitation energy of the radiating level, k the Boltzmann constant and T is the temperature. $Q(T)$ is the partition function of the considered atomic or ionic system. U_{pq} is the radiant power and is determined experimentally, while $Q(T)$, g_p and A can be found in literature [44, 51].

In case of the 579 nm transition of Hg this expression can be used to find the radial distribution of the temperature $T(r)$. This is done by replacing the left-hand-side of equation 6.2 by $p/kT(r)$ which is justified since the atomic Hg system delivers by far the most particles in the lamp so that Dalton's' law, $p = \sum nkT$, reduces to $p = n_{Hg(r)}kT(r)$. This bulk pressure can be assumed constant over the lamp. Since $U_{pq}(r)$ is known as function of radial position we can use equation 6.2 to determine the temperature as a function of radial position provided the pressure is known. Since this is not known we follow an iterative procedure. First a guessed value of p is inserted which gives, using the measured $U_{pq}(r)$, a radial $T(r)$ distribution. In the second step we determine $n_{Hg}(r) = p/kT(r)$ which, integrated over the whole volume, gives the total number of mercury atoms N_{Hg} in the discharge. In the last step this number, multiplied with the mass of a Hg atom, thus $N_{Hg}m_{Hg}$, is compared to the filling mass M_{Hg}. The mismatch $M_{Hg}/N_{Hg}m_{Hg}$ is used to correct the pressure. With this new pressure-value we can repeat steps 1 till 3 again. This is done until convergence is reached.

Calculation of the radial density profiles is as follows. First the emission of the line of interest is measured as a function of lateral position. This profile is then Abel inverted into a radial intensity profile. The next step depends on the species of which the emission line is measured.

In case of the 579 nm line of Hg, the intensity is calibrated and then the absolute radial intensity profile is used to numerically determine the temperature

profile. In case the atomic or ionic lines of Dy are measured, the temperature profile is combined with the calibrated radial intensity profile of the additive into an absolute radial system density profile using equation 6.2.

6.4 The model

A description of the model has been published in [40] and [56], reprinted in chapters 2 and 3 where it has been applied to a MH lamp based on a mixture of Hg and NaI. This model was modified to a simulation of a mixture of Hg and DyI_3, as discussed in chapters 4 and 5. One aspect of the model not discussed so far is the calculation of transport coefficients. This section will repeat the transport equation for the elements and discuss the calculation of the transport coefficients in the model.

6.4.1 Particle transport

Since we assume LTE, the particle densities may be described by the local temperature, pressure and elemental composition. Elemental pressure is defined as the pressure that contains all molecular, atomic and ionic contributions of a particular element. The elemental pressure p_α for the element α can be written as

$$p_\alpha = \sum_i R_{i\alpha} p_i, \tag{6.3}$$

with p_i the partial pressure of the species i, and $R_{i\alpha}$ the stoichiometric coefficient [32]. We solve a conservation equation for the elemental pressure

$$\nabla \cdot \left(\frac{D_\alpha}{kT} \nabla p_\alpha + \frac{p_\alpha}{kT} \vec{c}_\alpha \right) = 0, \tag{6.4}$$

with an effective diffusion coefficient D_α [32]

$$D_\alpha = p_\alpha^{-1} \sum_i R_{i\alpha} D_i p_i \tag{6.5}$$

and a pseudo convective velocity c_α [32].

The diffusion coefficient D_i is calculated from the binary diffusion coefficients D_{ij} by

$$D_i = \left(\sum_{j \neq i} (p_i/p) / D_{ij} \right)^{-1}. \tag{6.6}$$

The binary diffusion coefficient for the diffusion of species i through species j is given by [30, page 486] and depends on the differential cross-section.

In-situ measurements of the elemental pressure at the walls under microgravity conditions are not possible, therefore we assume a Dy elemental pressure at the wall of 517 Pa and an I elemental pressure of 4268 Pa. These vapour pressures were determined with x-ray induced fluorescence measurements at 1g [21]. These are assumed to give a good estimation of the vapour pressure at the walls and are used to fix the boundary conditions.

6.4.2 The selection of cross-sections

In the conservation equations which form the model, important roles are played by various transport coefficients, such as the diffusion coefficients D_i, the thermal conductivity λ_c and the electrical conductivity σ_{el}. These transport properties are calculated from collision integrals that are based on differential cross sections [42].

Ideally, one would like differential cross-sections for every possible collision between particles in the plasma. In practice such data is difficult to gather or calculate since for only a few interactions energy-dependent integral cross-sections σ_{ij} are available. When available these are used in the model. For collisions for which such data cannot be found approximations have to be used. The collisions can be classified along the following categories:

1. Charged - charged collisions; in this case the shielded Coulomb cross-sections is a good and generally applicable approach [33, page 55],

2. Neutral - neutral collisions; there where dedicated cross-section values are not available these interactions are described as hard sphere collisions,

3. Charged - neutral collisions; this category is the most complicated since, in principle, a full quantum mechanical (QM) treatment is needed in which, for instance, the effect of the Ramsauer minimum has to be taken into account. For each pair of interacting particles the QM aspects are different. If results of experiments or QM calculation are not available the use of the Langevin cross-section is the only option. The formula for the Langevin cross section reads

$$\sigma_{ij} = \sqrt{\frac{\pi \alpha_p q^2}{\mu_{ij} \epsilon_0 \left(|\vec{v}_i - \vec{v}_j| \right)}}, \tag{6.7}$$

with α_p the dipole polarisability of the neutral species, q the charge of the charged species, ϵ_0 the permittivity of free space and μ_{ij} the reduced mass $\mu_{ij} = m_i m_j/(m_i + m_j)$ of the system of colliding particles.

When considering the influence of the cross-section on the values of the transport coefficients D_i, λ_c and σ_{el} it is important to note that Hg atoms form the most dominant species in the discharge; all other species are present in small concentrations.

We begin with the electrical conductivity σ_{el} that is mainly determined by the elastic interactions between electrons with Hg atoms. This electron-Hg interaction is of the third category but fortunately the corresponding cross-section is well known and it is generally expected that the values from Rockwood [57] are correct within a few percent. We studied whether this is indeed the case by comparing the results using Rockwood values and Langevin cross-sections. As the value of this cross-section determines the lamp resistance and the ohmic dissipation we calculated the voltage drop over the lamp when the ohmic dissipation equals 110 W. This was done for two cases, one based on the Rockwood values and the other on the Langevin cross-section. Using the Rockwood values the model predicts a voltage drop of 99 V, which is consistent with the measured value. The calculations done with the Langevin cross-section, however, produces a voltage drop of 71 V, which is much too low. We may therefore conclude that the model gives a good description of the potential distribution over the lamp and the corresponding ohmic heating by using the Rockwood values.

Next we study the influence of the choice of cross-section for the thermal heat conductivity λ_c. Due to the low elemental concentration of Dy and I we can neglect the heat generation that is liberated in the formation of DyI_x molecules. The reactive part of heat conductivity can therefore be neglected and only the frozen part remains (see [42]) which is determined by the collisions of Hg atoms mutually. These Hg-Hg collisions are of the second category and experimental results given in [30] confirm that the hard sphere approach is valid here.

The diffusion of Dy containing species is determined by the collisions with Hg atoms. In case of the neutral species we deal with the second category for which the hard sphere approach can be used. Much less clear are the collisions between Hg atoms and Dy ions. These are of the third category and since there are no QM or experimental results available we have to use the expression of the Langevin cross-section. However, it is known from literature that this is not always a good approximation and errors in the order of 30% or more [58] are frequently reported. To study the impact of the $\sigma(Hg, Dy^+)$-value on the model results we performed two sets of calculations, one with the Langevin

cross-section σ_{LV} and one with a value that is 20% larger, i.e. 1.2 * σ_{LV}. In this way we can determine the importance of this Hg-Dy$^+$ cross section and test the possible errors introduced by the approximation.

6.5 Results and discussion

The experiment and the model results are compared in this section. Both model and experiments were done for a lamp in microgravity, so without convection, operating at 130 W (of which 110 W dissipated in the discharge and 20 W spend on electrode losses) and containing 10 mg Hg and 4 mg DyI$_3$. The sensitivity of the model result for the choice of $\sigma(Hg, Dy^+)$ is examined. To that end two different cross-sections were used for the model, namely the Langevin cross-section σ_{LV} and 1.2 σ_{LV}. This discussion will follow the line of the theory presented in section 6.3 where the three atomic systems were introduced, namely the Hg atom, the Dy ion and Dy atom. The Hg-system is used for the determination of the temperature, and the atomic and ionic Dy system for the spatial distribution of Dy atoms and ions and the radial Dy segregation.

The temperature profile as deduced from the Hg line is given in figure 6.4 and shows that the model based on the Langevin cross-section is in good agreement with the experiment. Both profiles have an axis temperature of 6000 K and nearly the same shape. If we take $\sigma(Hg, Dy^+) = 1.2 \, \sigma_{LV}$ this results in a broader temperature profile with a lower axis temperature. The reason why the higher $\sigma(Hg, Dy^+)$ value influences the temperature profile is the following. By increasing $\sigma(Hg, Dy^+)$ the ambipolar diffusion in the central region is being hampered which causes the Dy particles to be accumulated in the centre. The temperature then decreases slightly as Dy has a lower ionisation potential than Hg (5.93 eV versus 10.43 eV). However, the change in the temperature distribution remains in the error margin of 10% [12] so that no conclusions can be drawn about the optimum value for $\sigma(Hg, Dy^+)$ from the temperature value.

Figure 6.5 shows the total absolute density of atomic Dy for both the experiment and two model results: one for with the original cross section $\sigma(Hg, Dy^+)$ and one with $\sigma(Hg, Dy^+)$ increased by a factor 1.2. Both numerical and experimental curves have a steep slope at nearly the same radial position (about 3.3 mm) where the Dy atom associates into the DyI$_3$ molecule, see figure 6.2. The experimental curve has a steep slope, partially because in order for the Abel fit to yield physical results, the fit was forced to zero near the edges of the lateral profile [12]. It shows that the experimental and theoretical values of the maximum of the atomic Dy system agree with each other within 20%.
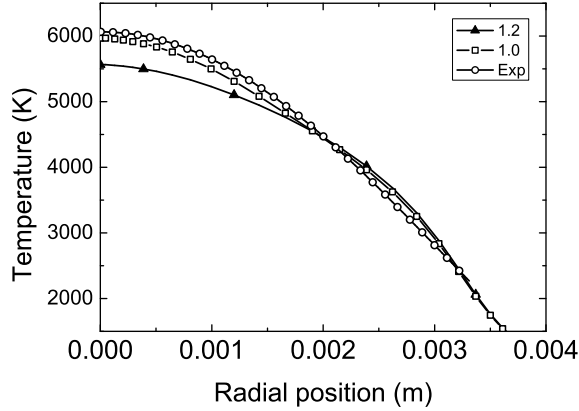
Figure 6.4: Radial temperature profile for a lamp containing 10 mg Hg and 4 mg DyI$_3$ at the midplane of the lamp. The numbers 1.0 and 1.2 refer to the two Langevin cross-sections that were used, the normal Langevin cross-section σ_{LV} and 1.2 σ_{LV}. Exp denotes the experimental results.

This is in fairly good agreement in view of the fact that the uncertainty of the transition probability from which the density is determined is in the order 20%. Also important is the uncertainty related to the cold spot temperature. A small change in this temperature will lead to a significant variation of the elemental Dy density.

By dividing the Dy atom density by the Hg atom density distribution (which is the bulk species) the atomic Dy concentration is found, see figure 6.6. The atom concentration gives an indication of the radial segregation. The concentration profile clearly shows radial segregation for both experiment and model. Compared to the experiment, the model predicts more profound radial segregation. However, by increasing the cross-section from σ_{LV} to 1.2 σ_{LV} we see that the theoretical central Dy concentration increases drastically; with more than a factor of 8. This implies that the amount of radial segregation is diminished and becomes much smaller than what is found experimentally. By increasing the cross-section, the diffusion is reduced, resulting in a decreased
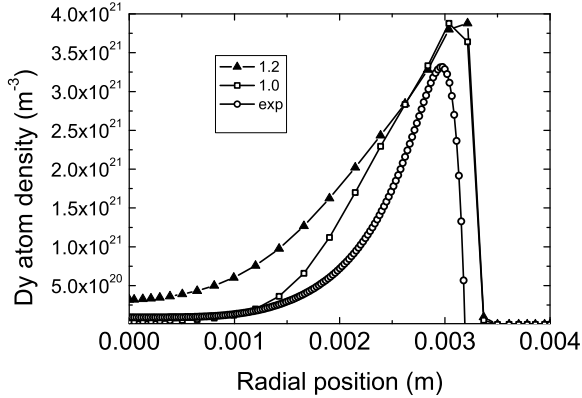
Figure 6.5: Total radial Dy atom density profile for a lamp containing 10 mg Hg and 4 mg DyI$_3$ at the midplane of the lamp. The numbers 1.0 and 1.2 refer to the two Langevin cross-sections that were used, the normal Langevin cross-section σ_{LV} and a value that is 20% larger:1.2 $\cdot\sigma_{LV}$. Exp refers the experimental results.

radial segregation.

The above clearly shows that the atom concentration at the centre is very sensitive to the choice of the cross-section; an increase of the cross section by 20% leads to an increase of the central atomic density of a factor of 8.2 and the figure suggests that $\sigma(Hg, Dy^+)$ will have a value somewhat larger than σ_{LV} but smaller than $1.2 \cdot \sigma_{LV}$. However, care should be taken with this theory-experiment comparison since the experimental values result from an Abel inversion which is quite sensitive for errors at the centre of a hollow profile.

The comparison of the model and experiment with respect to the Dy ion density is given in figure 6.7. We first focus on the central region where we find that, just as the Dy atom density, the theoretical value of central ion density is very sensitive to the value of $\sigma(Hg, Dy^+)$. The change from σ_{LV} to $1.2 \cdot \sigma_{LV}$ leads to an increase of the central density with a factor 5.4. This is smaller than in the atomic case where a ratio of 8.2 is found.

The reason that both the Dy atom and ion density increase is that, as a
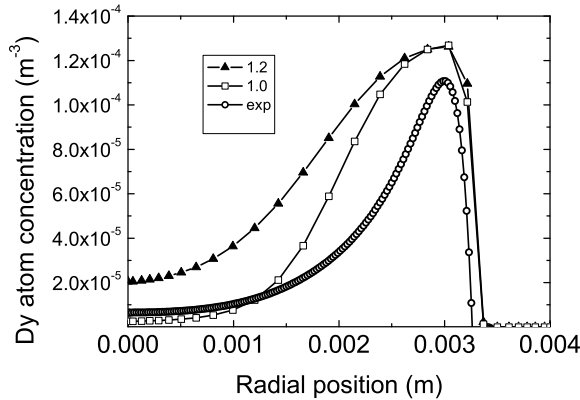
Figure 6.6: The atomic Dy concentration obtained by dividing the Dy atom density by the Hg density. The lamp contains 10 mg Hg and 4 mg DyI$_3$ at the midplane of the lamp. The numbers 1.0 and 1.2 refer to the two Langevin cross-sections that were used, the normal Langevin cross-section σ_{LV} and 1.2 ·σ_{LV}. Exp denotes the experimental results.

consequence of the decrease in the ambipolar diffusion coefficient, the amount of Dy is more easily 'trapped' in the centre. This causes the temperature in the centre of the discharge to become lowered (as shown in figure 6.4) which as a result will cause the Saha balance between the atomic and ionic system to shift with respect to the atomic system. This is why the atomic Dy increases more strongly than the Dy ion as $\sigma(Hg, Dy^+)$ is being increased.

Leaving the central region and moving outwards we see that the experimental Dy ion density in figure 6.7 has a much steeper slope than what the model predicts. In part this is caused by the Abel fitting as mentioned before. However, a more important aspect is the validity of LTE away from the centre. The experimental Dy ion density as shown in figure 6.7, denoted by "exp Boltzmann", is based on the application of the Boltzmann balance (equation 6.2) in the ionic system; this gives the Dy ion system density using the emission of a Dy ion line. However, since the charge of the core of the ion system ($Z = 2$) is twice as large as that of the atom system ($Z=1$), we can expect that the transi-
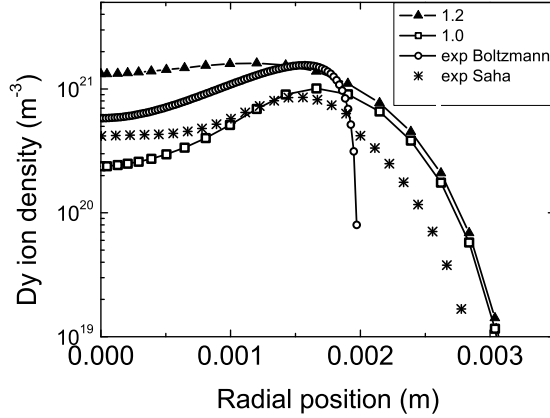
Figure 6.7: Radial Dy ion density profile for a lamp containing 10 mg Hg and 4 mg DyI$_3$ at the midplane of the lamp. The numbers 1.0 and 1.2 refer to the two Langevin cross-sections that were used, the normal Langevin cross-section σ_{LV} and 1.2 $\cdot\sigma_{LV}$. Exp denotes the experimental results. The experimental value for the Dy ion density was determined by either Boltzmann, denoted as exp Boltzmann; or by Saha, then denoted by exp Saha.

tion frequency induced by electron collisions will be smaller (this scales as Z^{-2}) [59] whereas the radiative decay transition (scaling as Z^4)[59] will be higher than in a comparable atomic system. This means that as n_e decreases (in the direction toward the wall) the electron-ruled Boltzmann balance of excitation and de-excitation will no longer be in equilibrium. The spontaneous emission will then become the most dominant depopulation process and the level is in the so-called Corona balance [59]. This causes the density of radiating states to decline. This implies that the ionic system density as deduced from these levels will decline as well.

We first investigate a possible departure from equilibrium by calculating the ion density using the Saha relation between the atomic and ionic system. This density is in fact based on the atomic radiation and thus the atomic system. For this system we can expect that, due to the lower Z value (Z=1), it will not

easily be effected by a drop in n_e. The Saha relation between n_i, the system density ion stage, and n, the density of Dy atoms, reads

$$\frac{n_e \, n_i}{n} = 2\frac{Q_i}{Q} \left(\frac{2\pi m_e kT}{h^2}\right)^{3/2} e^{-I/kT} \tag{6.8}$$

where Q is the partition function for the neutral species and Q_i the partition function for the ion, m_e the electron mass, T the temperature, I the ionisation potential of the atomic ground state, k the Boltzmann and h the Planck constant. The density of the Dy ion system can be found by inserting in this equation for n_e the sum of the Hg ion and the Dy ion density. For the atom density n the measured Dy atoms as shown in figure 6.5 are used.

The result of this equation, given in figure 6.7 denoted with "exp Saha", show a much better agreement between the calculated ion density using Saha's equation and the model results in the outer region. In contrast to the curve found by employing the Boltzmann relation (equation 6.2), the Saha value of the ion system density declines more gradually in the outer region. There is a factor of 2 difference between the Saha calculation and the model results. This may be caused by a number of factors. First, there is more atomic Dy in the model than in the real lamp as was shown in figure 6.5. Second, there may be an error in the transition probability, leading to an error in the atom density calculated with equation 6.2. Finally, an error may be introduced by the Abel inversion.

As stated above in dealing with the Saha equation, we have to take n_e equal to the sum of the Hg ion and the Dy ion density. In contrast to commercial lamps with PCA tubes for which the Dy vapour pressure is higher than in our model lamp used in the experiments we can not neglect the contribution of the Hg ions. In fact it was found experimentally from the Hg/Dy ion ratio [12] that the Hg ions dominate in the centre, see figure 6.8 where the experimental values of the $n(Hg^+)/n(Dy^+)$ ratio are given. Two ratios are shown, one of which the Dy ion calculation is based on Boltzmann (cf. equation 6.2) the other of which the calculation is based on Saha (cf. equation 6.8). These are compared to two model results based on $\sigma(Hg, Dy^+) = \sigma_{LV}$ and $\sigma(Hg, Dy^+) = 1.2 \cdot \sigma_{LV}$.

It is clear the model predicts the ratio $n(Hg^+)/n(Dy^+)$ to be high for a normal Langevin cross-section. At higher cross-section ($1.2 \cdot \sigma_{LV}$) this ratio is much lower, as there are more Dy ions in the centre (cf. figure 6.7). A higher cross-section causes Dy ions to be accumulated in the centre so that the central temperature will decrease. This will radically reduce the number of Hg ions, as they have a much higher ionisation potential.
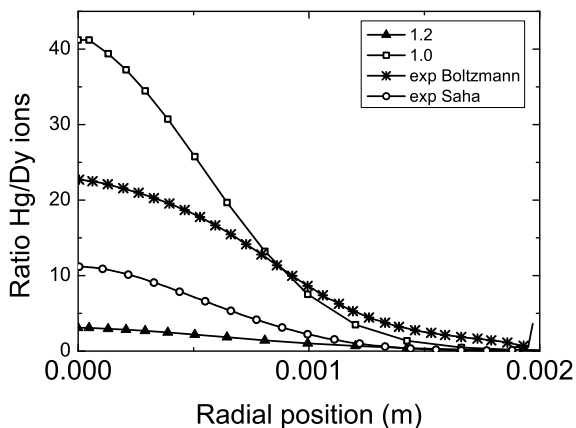
Figure 6.8: The Hg ion and Dy ion ratio for a lamp containing 10 mg Hg and 4 mg DyI$_3$ at the midplane of the lamp. The numbers 1.0 and 1.2 refer to the two Langevin cross-sections that were used, the normal Langevin cross-section σ_{LV} and 1.2 $\cdot \sigma_{LV}$. Exp denotes the experimental results. The ratio is calculated from either the measured Dy ion density (calculated from Boltzmann) or from the measured Dy atom density (calculated from Saha).

It can be concluded from the above that the Hg/Dy ion ratio is the most effective parameter for finding the optimum value of $\sigma(Hg, Dy^+)$ when comparing the results of the model with that of the experiment. An advantage of using the ion ratio is that the Abel inversion is more reliable for the Dy ion than for the atom as the latter contains a hollow structure. Figure 6.8 suggests that the best value of the $\sigma(Hg, Dy^+)$ will in the order of $1.1 \cdot \sigma_{LV}$.

6.5.1   Departure from LTE

We now return to the topic of the rapid decay in the Dy$^+$ density at r=0.002 m as shown in figure 6.7, which was found using Boltzmann's law. The Dy ion system density is determined by that of an excited Dy ion state which decreases rapidly due to the sudden decrease of the electron density. This underpopulation
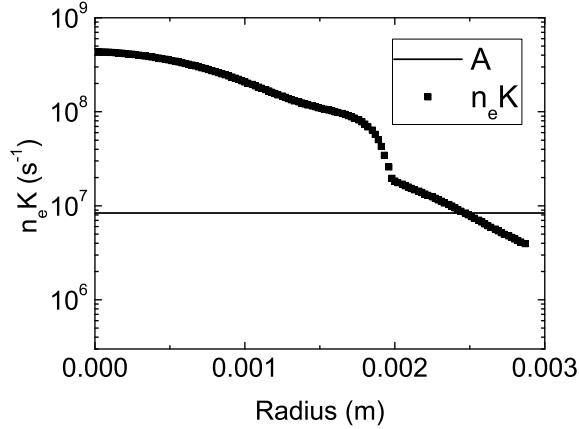
Figure 6.9: The collision frequency $n_e K$ compared to the radiative frequency which is represented by the transition probability A.

of the excited Dy ions has been previously reported [11] and is, as mentioned before, expected near the wall where the number of electrons is dramatically reduced. This causes the Boltzmann balance to shift to a Corona balance and this leads to a departure from LTE. A deviation from LTE in the outer region of the discharge has already been observed for the high pressure sodium lamp [60].

The transition from the Boltzmann-Saha balance to the Corona balance, happens when the collision frequency $n_e K_p$ is about equal to the radiative frequency (i.e. transition probability) A_p.

$$n_e K_p \simeq A_p \tag{6.9}$$

where A_p and $n_e K_p$ are the rates for total radiative and collisional destruction. We estimate the collision frequency by treating the Dy ion as hydrogen-like. The collision rate can then be written as [59]

$$K_p = 4\pi a_0^2 (p/Z)^4 \left(\frac{3kT}{m_e} \right)^{1/2} \tag{6.10}$$

where a_0 is the Bohr radius, Z the charge number of the core (which is 2 for the ion) and m_e the electron mass. The effective principal quantum number p of the level in question is calculated from $Z\sqrt{Ry/E_p}$ with Ry the Rydberg energy and E_p the ionisation potential of the level in question (thus in this case the energy needed for Dy^{2+} formation) [59]. For A_p we use the radiative transition probability of $A_p = 8.4 \cdot 10^6$ s^{-1} as used in the experiment.

The results are depicted in figure 6.9. It shows that the assumption of a Boltzmann distribution for the excited ion state is no longer valid after r= $/approx$2 mm corresponding to half of the radius of the inner bulb. This results in the excited Dy ions to be underpopulated. An underpopulation of the excited states with respect to Boltzmann means that equation 6.2 will underestimate the density of the ions. Thus we have found deviations from LTE. However, this departure from LTE only has a limited effect on the main plasma parameters such as the temperature and the electron density. It will also not change the spectrum emitted by the plasma substantially. This means that using an LTE model is justified to describe the phenomena in this type of lamp. When we calculate the threshold in equation 6.9 for the Dy atom we find that the Boltzmann balance still holds.

It should be realized that in the way we employ equation 6.9 a hydrogen-like system is assumed and we thus ignore the fact that the Dy ion has much more lower lying levels that will facilitate step-wise excitation instead of direct excitation from the ground level. For a proper description of the experimental results a full collisional radiative model would be needed which is beyond the scope of this work.

6.6 Conclusions

There is a reasonable agreement between model and experiment. The model is, however, very sensitive to the elastic scattering cross sections between minority species and the background Hg gas. The following cross sections are used: the electrical conductivity is based on the electron-Hg cross-section from Rockwood, the thermal conductivity is determined from hard-sphere collisions and the Hg-Dy$^+$ collisions are determined from the Langevin cross-sections. The temperature profiles are in good agreement but sensitive to the Langevin cross-section used for the Hg-Dy$^+$ collisions. The comparison between the experiment and model results for the Dy atom concentration shows that the model predicts more profound radial segregation. Both the atomic and ionic density distribution are very sensitive to the choice of cross-section.

The ratio Hg^+/Dy^+ was found to be extremely sensitive for the cross-section of the elastic interaction $\sigma(Hg, Dy^+)$ between Dy^+ and Hg atom. The sensitivity analysis reveals that equating $\sigma(Hg, Dy^+)$ to a value that is 10% higher than the Langevin cross section is the best choice. There is a clear discrepancy between experiment and the LTE-based model for the Dy ion density profiles. The experiment shows the Dy ion density to decrease much more rapidly. Further analysis showed deviations from LTE in the outer regions of the plasmas for relative radial positions of r/R > 50%. These deviations are manifest in the excited part of the Dy^+ system that for relatively low n_e is ruled by the Corona rather than by the Boltzmann balance. However, this departure of LTE only has a limited effect on the main plasma parameters which means that using an LTE model is justified.

Chapter 7

Comparison with centrifuge experiments

Abstract.
The effect of the competition between convection and diffusion on the distribution of metal halide additives in a high pressure mercury lamp has been examined by placing COST reference lamps with mercury fillings of 5 mg and 10 mg in a centrifuge. The resulting distribution of the additives, in this case dysprosium iodide, has been studied by numerical simulations and by measurements of the density of dysprosium atoms in the ground state using imaging laser spectroscopy. The competition between axial convection and radial diffusion determines the degree of axial segregation of the dysprosium additives. By subjecting lamps to different accelerational conditions the convection speed of the mercury buffer gas is altered while the diffusion speeds remain constant. The competition between axial convection and radial diffusion is best characterised by the dimensionless Peclet number. The degree of demixing is quantitatively characterised by the segregation depth.

This chapter is based on a publication submitted on invitation to a J Phys. D. Special issue as *"Competition between convection and diffusion in a metal halide lamp, investigated by numerical simulations and imaging laser absorption spectroscopy"* with co-authors A. J. Flikweert, T. Nimalasuriya, W. W. Stoffels and J. J. A. M. van der Mullen.

7.1 Introduction

In previous chapters a numerical model was developed to study the the distribution of additives in a Metal Halide (MH) lamp. In chapter 2 the basic theoretical framework was derived from kinetic theory. Chapter 3 then extended this model to cover the case of electrodes protruding into the plasma. Subsequently, in chapters 4 and 5 the model was overhauled to allow for comparison with experiments done on lamps containing dysprosium tri-iodide. This model was compared with results under microgravity conditions in chapter 6. In this chapter we will further compare the model with experiments as well as focusing on the influence of convection on the distribution of additives in the lamp.

In chapters 2 and 3 it was found that increasing the pressure increases the convection in the lamp. Results from the model showed that there is an optimum pressure at which the axial segregation is most pronounced. In chapter 4 it was found that this occurs when the convective and diffusive processes are in the same order of magnitude. In the two limiting cases, when there is no convection, or when there is extremely high convection, little to no axial segregation is present. Increasing the pressure increases the rate of convection while decreasing the rate of diffusion.

The rate of convection can also be influenced by placing the lamps under different accelerational conditions. In the previous chapter we compared the results from the model with experiments done under microgravity, where convection is absent. This enabled us to study the effect of diffusion on the phenomenon of radial segregation in isolation. In this chapter we will compare results from the numerical model with experiments under hypergravity conditions to enhance convection. To create these hypergravity conditions the lamps were placed in a centrifuge. The design of these experiments are outlined in previous publications [61, 62, 22, 13, 12, 63]. The metal-halide lamp that is investigated in the centrifuge is again a COST lamp [9]. It contains 4 mg DyI_3 as salt additive, which is partially evaporated when the lamp is burning. In the centrifuge setup, the ground state Dy density distribution is measured by means of Imaging Laser Absorption Spectroscopy (ILAS) [13]. These experimental results are compared with the model.

7.2 Experiment

A centrifuge was built as a tool to investigate MH lamps [9] under hypergravity conditions up to $10g$ and vary the convection speed in this way. In the next

section the results will be compared with the results from the model.

7.2.1 Measurement technique

The experiment has been described before [13]; a summary will be given for clarity. The centrifuge shown in figure 7.2 consists of a pivot, an arm connected to the pivot and at the end of the arm a gondola that contains the lamp and diagnostic equipment. The total diameter at maximum swing-out of the gondola is close to 3 m. The total acceleration vector is always parallel to the lamp axis.

The measurement technique that is used in the centrifuge is Imaging Laser Absorption Spectroscopy (ILAS). By using this technique, the 2D density distribution of the ground state Dy atom can be obtained. The principle is as follows. A laser beam is expanded so that it illuminates the full lamp burner. When the lamp is switched on, part of the laser light is absorbed by Dy atoms in the ground state. Behind the lamp, the light that is transmitted by the lamp burner is detected. By comparing the detected laser intensity with and without absorption, the line-of-sight ground state atomic dysprosium density is obtained for each position in the lamp burner.
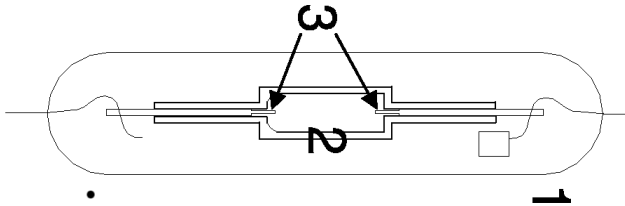

Figure 7.1: Schematic picture of the lamp, (1) outer bulb; (2) burner with height 20 mm and diameter 8 mm; (3) electrodes, distance between both electrodes ∼18 mm [9].

7.2.2 The lamp

The investigated lamps are COST lamps [9], see figure 7.1. The lamps are 20 mm in height (18 mm electrode distance) and 8 mm in diameter. They contain either 5 mg Hg or 10 mg Hg. Furthermore they contain 4 mg DyI_3 as salt additive and 300 mbar Ar/Kr^{85} as a starting gas. The input power is 148 W; the acceleration a is varied from 1 g to 10 g.
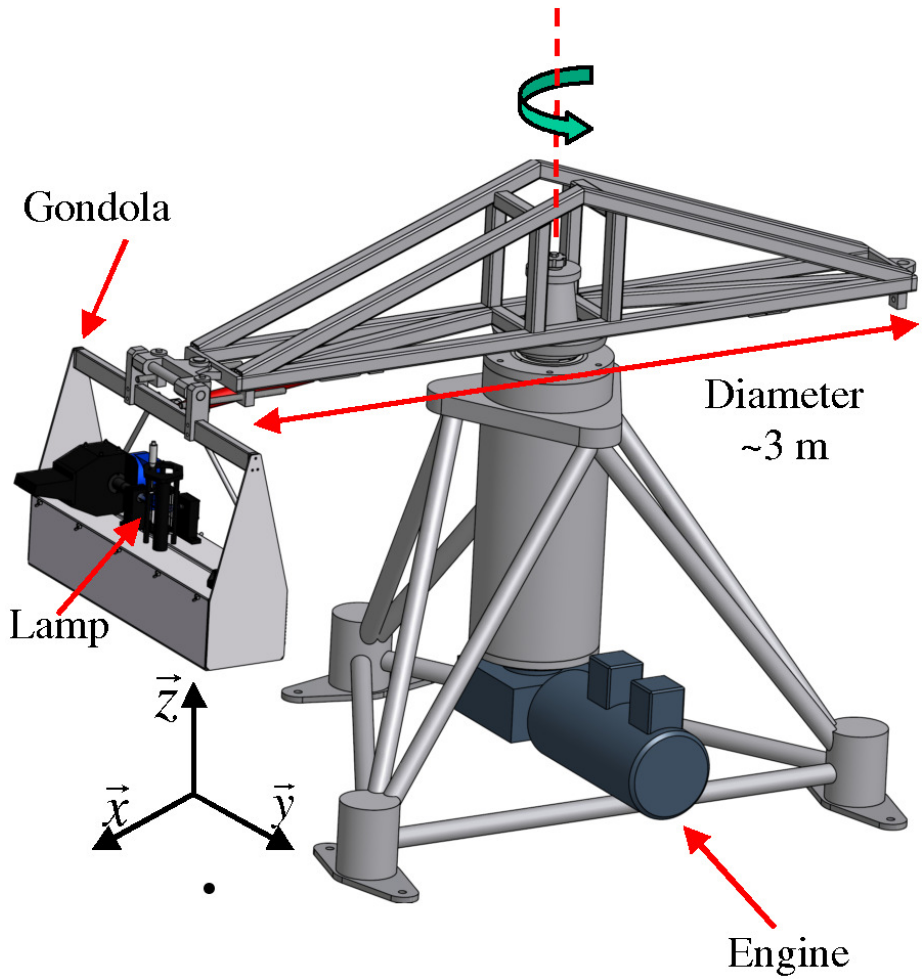
Figure 7.2: Schematic representation of the centrifuge. The coordinate system shown is that of the lamp in the gondola; this is a co-moving system such that $\vec{z}$ is always parallel to the lamp axis [13].

7.3 Results

The model described in chapters 4 and 5 was run for a set power P_S of 135 W and compared with experimental results using a 148 W ballast. The difference of 13 W is an estimation of the electrode losses which are not accounted for in the model. Experiments were done with lamp fillings of 5 mg and 10 mg Hg. The model was run with lamp fillings ranging from 3 mg to 20 mg Hg. To fix the boundary conditions for the elemental pressure we assume the existence of a cold spot at the bottom corner of the lamp, where the elemental pressure is derived from the x-ray induced fluorescence measurements at 1 g of the elemental density of Dy and I at the cold spot [21]. Everywhere else the flux through the wall is zero.

Direct measurements of the elemental pressure at the walls are not possible for the lamps in the centrifuge, therefore we assume a Dy elemental pressure at the wall of 517 Pa and an I elemental pressure of 4268 Pa. These vapour pressures were determined with x-ray induced fluorescence measurements at 1 g [21]. These are assumed to give a good estimation of the vapour pressure at the walls and are used to fix the boundary conditions. Note that there is an excess of iodine in the cold spot. This excess occurs because dysprosium is absorbed by the walls of the lamp.

The density of dysprosium atoms was measured with the ILAS technique described in the previous section. The lamp underwent centripetal acceleration in the centrifuge from 1 g to 10 g. The measurement technique yields the column density of dysprosium atoms in the ground state along the line of sight. The model yields many more results, of which only a minor part can be directly correlated to the experiment. We will present some of the model results separately to further insight into the mechanisms behind what is observed experimentally.

The model solves differential equations for the total pressure, the velocity, the temperature, the electric potential and the elemental pressures. From these a number of derived quantities are obtained, notably the species densities and the radiation intensity. We will first present the elemental pressures at different lamp pressures and under different accelerational conditions.

7.3.1 Elemental pressure

The elemental dysprosium pressure at 1 g and 2 g with 10 mg of mercury is given in figure 7.3 clearly shows both axial and radial segregation. The amount of dysprosium in the top of the lamp increases with increasing centripetal acceleration.
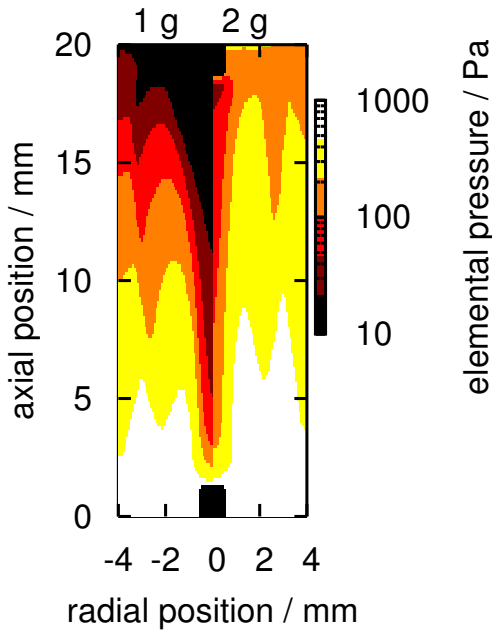
Figure 7.3: Simulated elemental dysprosium pressure for a lamp with a 10 mg
mercury filling at 1 g (left) and 2 g (right).

When one examines figure 7.3 carefully, local minima and maxima can be
seen in the elemental dysprosium pressure. These are shown more clearly in the
profiles for a total mercury content of 5 mg shown in figure 7.4. These local
minima and maxima are not present if convection is switched off in the model, as
is shown in figure 7.5. For more results comparing this model with microgravity
experiments we refer to [14]. In figure 7.6 the axial convection speed is plotted.
The axial speed is greater in the centre of the lamp than at the edges, due to the
lower density and the smaller cross sectional area in the centre. Consequently,
the elemental dysprosium concentration in the center rises as the acceleration
increases. The radial position where the axial velocity crosses through zero does
not show the same increase in elemental dysprosium. The result is that with
the increase in convection more dysprosium enters the discharge and that the
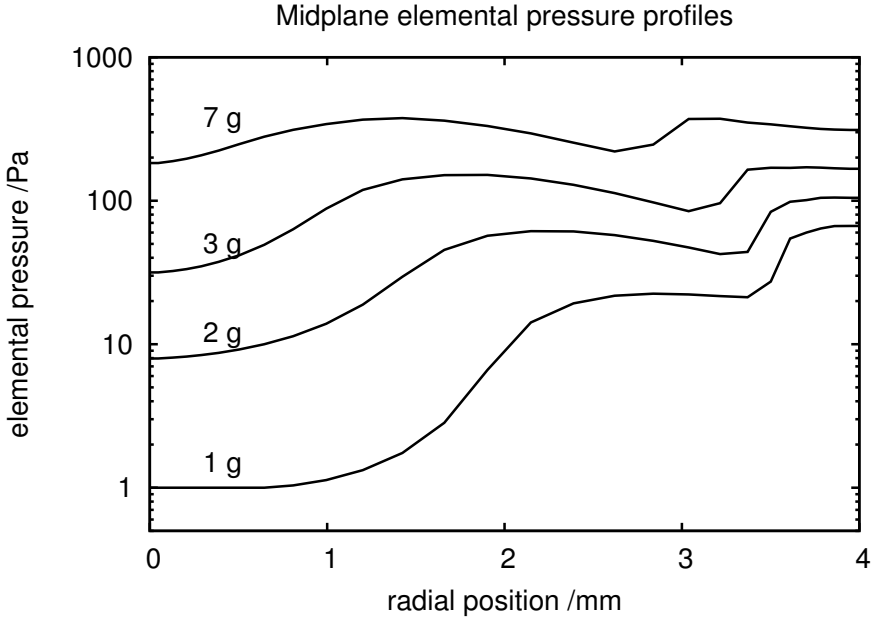
step like radial profile is disturbed.

Figure 7.4: Simulated midplane elemental dysprosium pressure profiles for accelerational conditions ranging from 1 g to 7 g for a lamp with 5 mg of mercury filling. At low convection speeds the radial profiles have a shape comparable with the microgravity situation.

7.3.2 Atomic dysprosium density

The experiment measures the column density of dysprosium atoms in the ground state. The model calculates the dysprosium atom density from the elemental pressure, total pressure and temperature. An example of the calculated dysprosium density is shown in figure 7.7. As is evident in this figure, the dysprosium atom density decreases towards the top of the lamp. Increasing the convection speed by increasing the acceleration causes better mixing.

To compare with the experiments column densities have been calculated. These are shown in figure 7.8. For comparison, figure 7.9 shows the measured
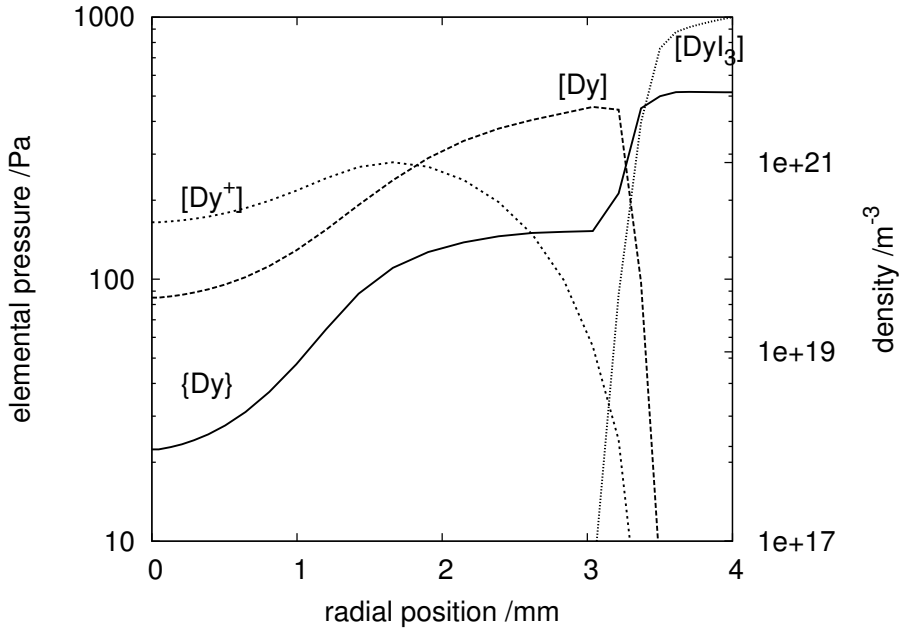
Figure 7.5: Simulated elemental dysprosium pressure (Dy in the figure) with convection switched off (corresponding to microgravity). The discharge shows no axial segregation in this case. For comparison, the densities of the dysprosium ions, atoms and DyI_3 molecules are plotted (denoted with square brackets).

column densities of dysprosium atoms in the ground state. A qualitative comparison of these graphs shows a number of features present in both model and experiment. Most notable are the heart shaped regions near the bottom of the lamp, where the dysprosium atoms are concentrated. Under higher accelerational conditions these regions move up slightly and become more elongated, this feature is present in both the model and the experiment.

For a more quantitative comparison, cross sections of the results from both the model and the experiment at an axial position of 5 mm from the bottom of the lamp are show in figure 7.10. As before, the results are for a lamp containing 10 mg of mercury under 1 g and 2 g acceleration in the centrifuge. The position of the maximum atom density in the simulations correspond well with the maximum absorption in the experiment. The absolute values, however, do
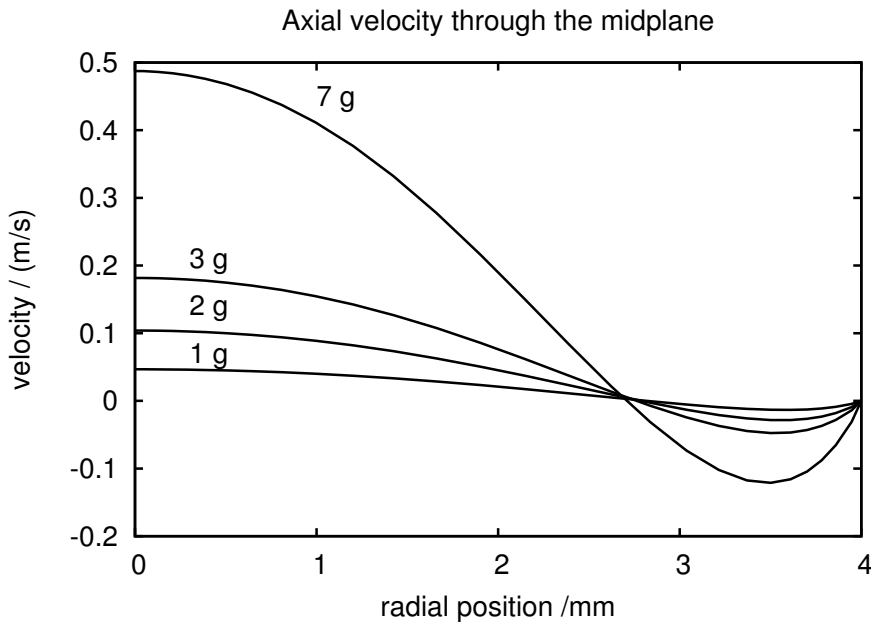
Figure 7.6: Simulated axial velocity through the midplane for accelerational conditions ranging from 1 g to 7 g in a lamp with 5 mg of mercury filling.

not agree. Figure 7.11 compares the measured atomic ground state density with the simulated atomic densities along the axis, and 2 mm off-axis. These results show good qualitative agreement between the simulation and the experiment. In particular, the position of the maximum density shows good agreement. The densities in the simulation are generally much larger. A possible reason might be the assumed cold spot vapour pressure. The cold spot vapour pressure depends exponentially on the temperature, as shown in figure 7.12. During the lifetime of the lamp, however, dysprosium migrates into the quartz walls. The individual lamps also differ. A change in the temperature of just 10 K leads to a 30 % increase in the vapour pressure just above the cold spot.
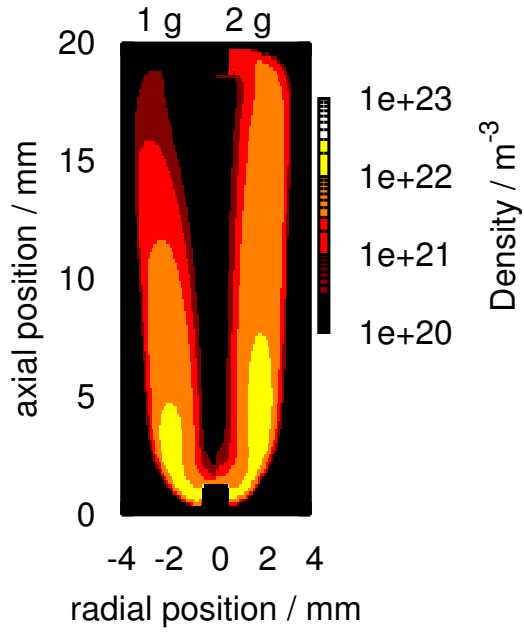
Figure 7.7: Simulated atomic dysprosium density for a lamp containing 10 mg of mercury at 1 g and 2 g simulated accelerational conditions. The 1 g result is shown mirrored (negative radial positions) and the 2 g result is shown on the right half of the graph.
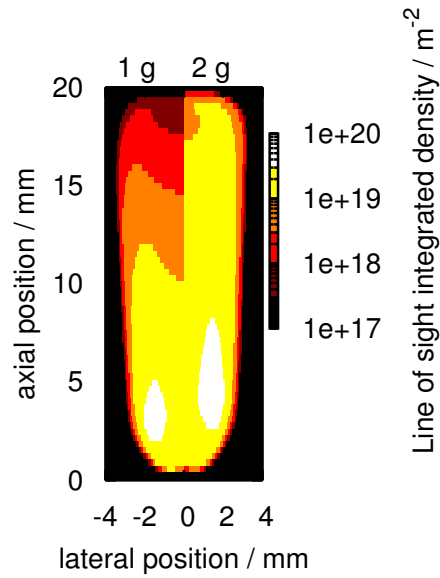
Figure 7.8: Simulated column densities of dysprosium atoms for a lamp containing 10 mg of mercury at 1 g and 2 g simulated accelerational conditions. As in the previous graphs the 1 g results are shown mirrored with negative lateral positions.
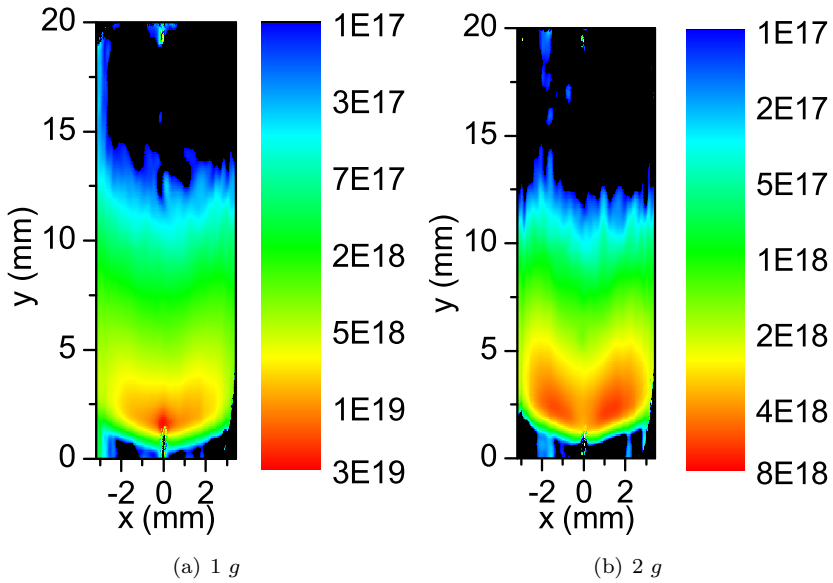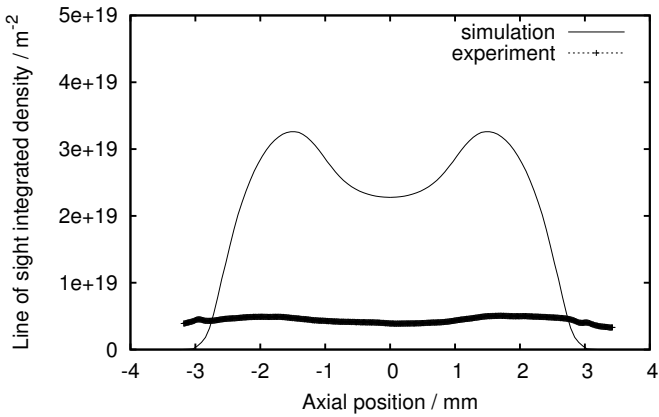
(a) 1 g

(b) 2 g

Figure 7.9: Experimental results for the ground state column densities of dysprosium atoms at 1 g and 2 g for a lamp containing 10 mg of mercury. Note that negative and positive lateral positions correspond to the left and the right side of the lamp respectively.
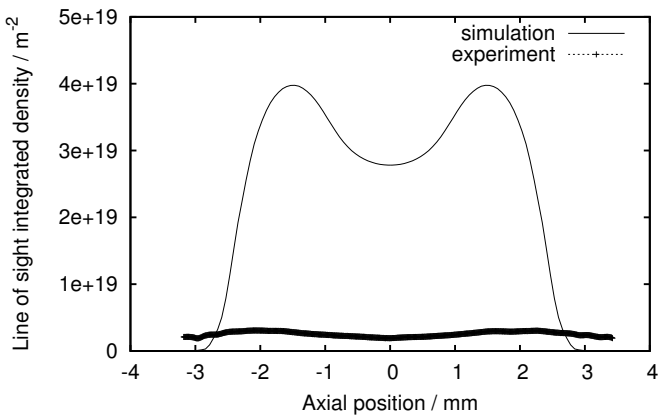
(a) 1 g

(b) 2 g

Figure 7.10: Experimental results for the ground state column densities of dysprosium atoms at 1 g and 2 g for a lamp containing 10 mg of mercury compared with the simulations. Results shown are at an axial position of 5 mm from the bottom of the lamp.
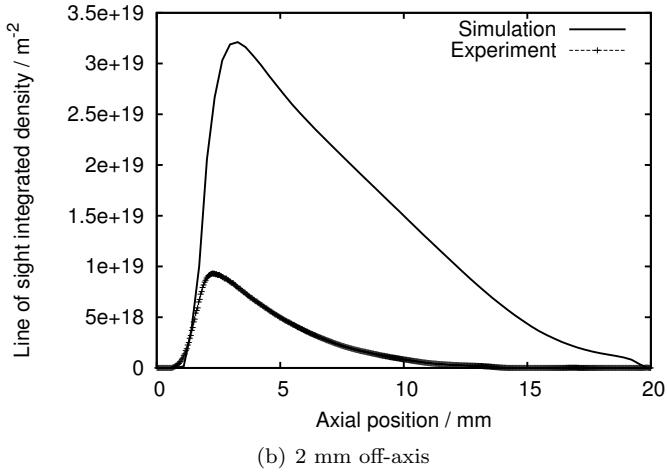
(a) along the axis
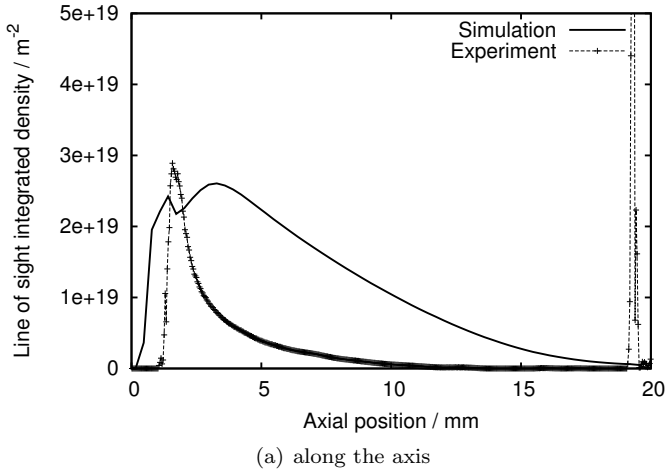

(b) 2 mm off-axis

Figure 7.11: Experimental results for the ground state column densities of dysprosium atoms at 1 *g* for a lamp containing 10 mg of mercury compared with the simulations. Results shown are along the axis, and 2 mm off-axis.
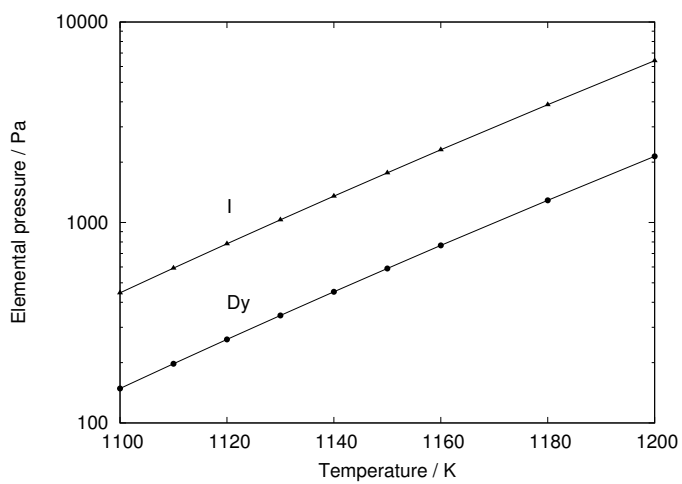
Figure 7.12: Elemental vapour pressure of dysprosium and iodide, as calculated by Gibbs minimisation for temperatures between 1100 K and 1200 K.

7.4 Cold spot vapour pressure

To further investigate the dependence on the cold spot vapour pressure different
the model was rerun with dysprosium vapour pressures of 100 Pa to 400 Pa
in steps of 50 Pa. This study revealed that a dysprosium vapour pressure of
150 Pa, corresponding with a temperature of 1100 K gave the closest match with
experimental results. Figure 7.13 shows the ground state line-of-sight-integrated
densities of the dysprosium atoms at 5 mm from the bottom electrode for vapour
pressures between 100 Pa and 250 Pa compared with experimental results. The
results with the 150 Pa vapour pressure also match well at other distances from
the electrodes as shown in 7.14 which compares lateral ground state densities
as predicted by the model with a cold spot vapour pressure of 150 Pa with
experiments along a line 2 mm off-axis. A line 2 mm off-axis is chosen as it
offers the largest signal, and hence the best signal-to-noise ratio.

Figure 7.13: Experimental results for the ground state column densities of dys-
prosium atoms at 1 *g* for a lamp containing 10 mg of mercury compared with
the simulations at vapour pressures from 100 Pa to 250 Pa. Results shown are
at an axial position of 5 mm from the bottom of the lamp.

Varying the cold spot vapour pressure also allows us to study the effect of
the radiation emitted by the additive. In the limit that the cold spot vapour
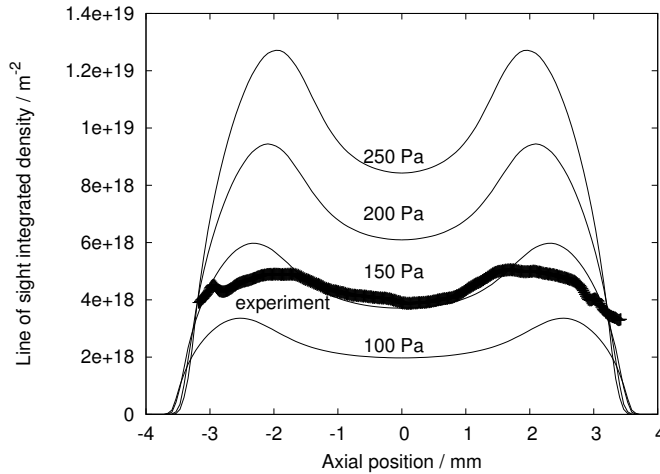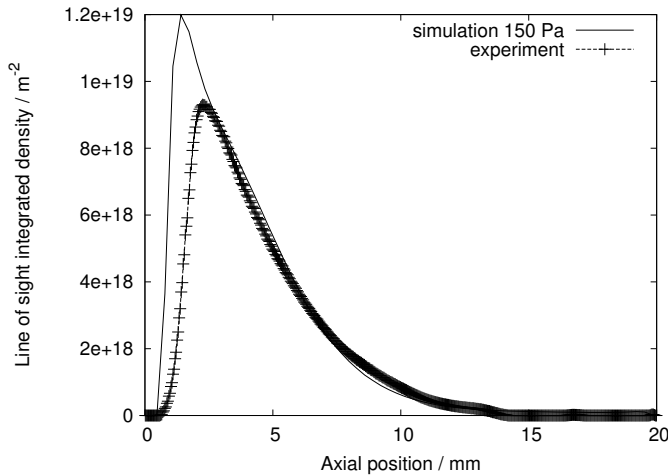
Figure 7.14: Experimental results for the ground state column densities of dysprosium atoms at 1 g for a lamp containing 10 mg of mercury compared with the simulations at a vapour pressure of 150 Pa.

pressure of dysprosium approaches zero the lamp becomes a pure mercury lamp again. Figure 7.15 shows the resulting temperature profiles in the midplane between the electrodes. From this figure it becomes evident that increasing the dysprosium elemental vapour pressure increases the contraction of the arc. This finding is in line with earlier findings in chapter 5 and is due to the radiation emitted by dysprosium. In chapter 5 the radiation emitted was increased in the model by increasing the transition probabilities of the radiation emitted by dysprosium atoms and ions. Here it is increased by simply adding more dysprosium to the discharge. The net effect is very similar and due to radiative cooling. The greatest concentration of emitting species is found just off-centre. The radiation emitted by dysprosium is optically open and not reabsorbed near the walls. Thus the radiation cools down the plasma on the flanks. To still allow sufficient current to pass through the plasma the centre has to become hotter. Hence, the observed contraction of the arc.

The hotter centre also results in increased convection, as is shown in figure 7.16. This is simply due to the larger temperature difference. The larger temperature difference translates directly into larger density gradients, which drive
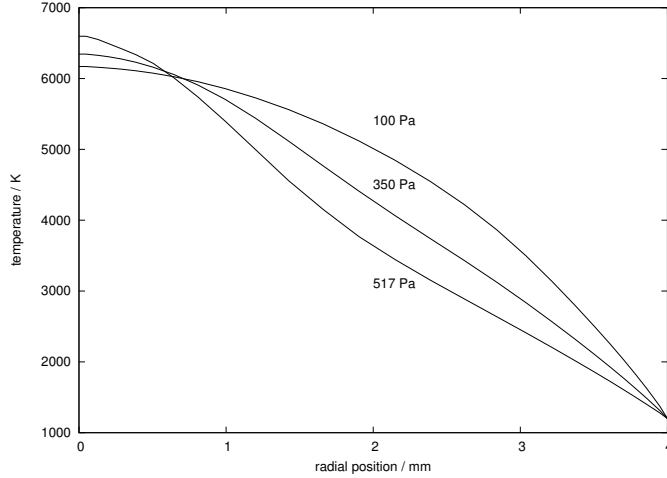
Figure 7.15: Midplane temperature profiles for three different cold spot vapour pressures: 517 Pa, 350 Pa and 150 Pa. Adding more dysprosium clearly increases the contraction of the arc.

the convective flow.

7.4.1   Demixing

We studied the demixing by defining the average segregation depth τ_α of element α as

$$\tau = \frac{1}{V} \int_V \tau_L dV, \tag{7.1}$$

with τ_L given by

$$\tau_L = \frac{L}{p_\alpha} \left(\frac{\partial p_\alpha}{\partial z} \right), \tag{7.2}$$

If τ is much smaller than unity the element is homogeneously distributed. Axial demixing occurs if τ is greater than unity.

To compare results with different lamp fillings we examine the segregation as a function of the Peclet number as defined in (1.1). We use the velocity on the axis halfway between the electrodes. The elemental diffusion coefficient is taken from the same spot. The model was run with a number of different
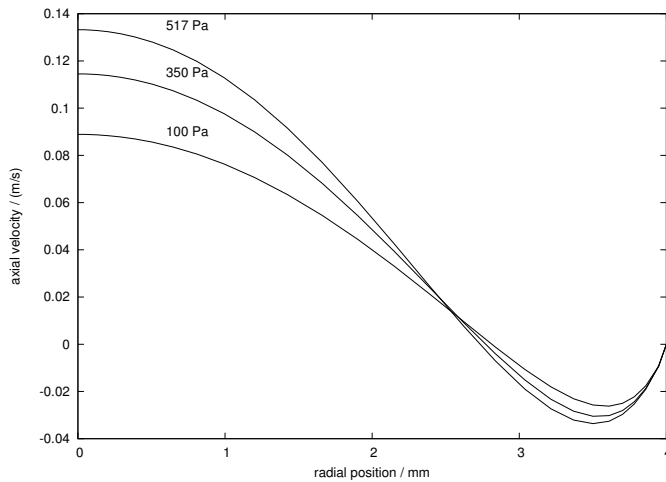
Figure 7.16: Midplane axial velocity profiles for three different cold spot vapour pressures: 517 Pa, 350 Pa and 150 Pa. Adding more dysprosium increases the contraction of the arc and thereby increases the axial velocity through the midplane.

pressures and simulated accelerational conditions. If we plot τ as a function of Peclet number a single curve emerges along which all results lie. The maximum point on this curve lies at $Pe = 1$.

Figure 7.17: Segregation depth as a function of the Peclet number as defined by 1.1 obtained from the model. Lamp fillings between 3 mg and 20 mg and accelerational conditions between 1 g and 10 g are shown. Each lamp filling leads to a line in the figure. Note that τ has a maximum at $Pe = 1$. Iodine shows much less demixing than dysprosium.

Figure 7.18: Dysprosium elemental pressure along the axis for the original grid (marked "1 ×") and a grid with double the number of cells in each direction (marked "2 ×").
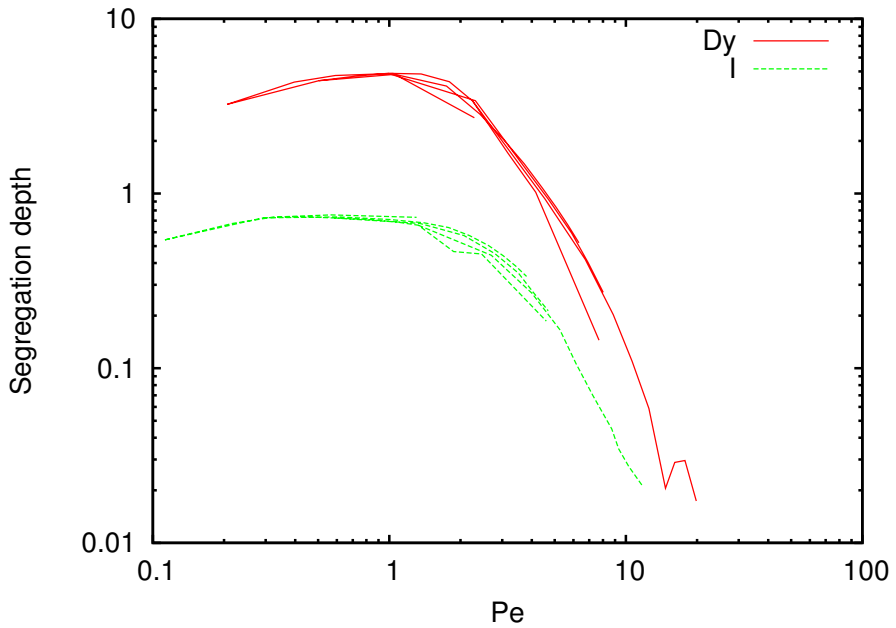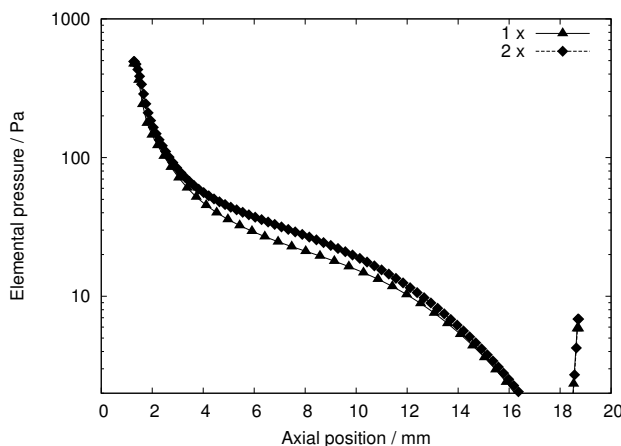
7.4.2   Discretization errors

In the numerical models described in this chapter a coarse finite volume grid was used with 66 by 28 cells in the the axial and radial directions, respectively. The use of such a coarse grid is possible because the flow is laminar and the size of the features studied are large in comparison with the size of the lamp. Grid stretching is used to reduce the size of the cells near the walls where the gradients in the temperature and the elemental pressure are larger. The hybrid scheme [15, page 88] used by Plasimo should work well with relatively coarse grids. To get an idea of the influence of discretization errors on the results one of the calculations was repeated with a grid with double the number of cells in each direction. The result is shown in figures 7.18 through 7.21. The conditions shown are with a cold spot vapour pressure of 350 Pa, 1 g acceleration and a lamp filling of 10 mg. As with the other models in this chapter the lamp power is 135 W.

The largest differences are observed in the elemental dysprosium pressures. These are shown in figure 7.18 and 7.19 which show the elemental pressure along the axis and midplane, respectively. The coarser grid does not sufficiently
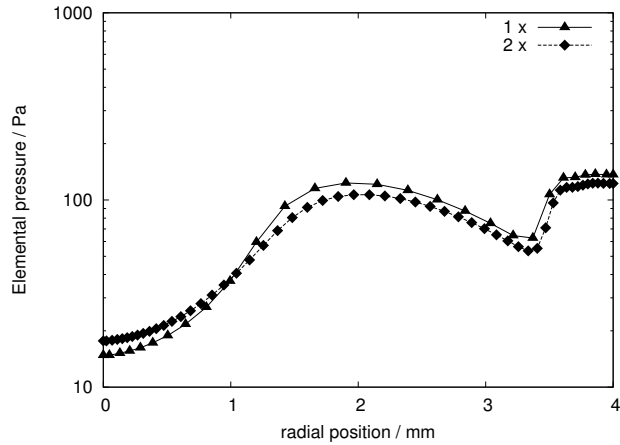
Figure 7.19: Dysprosium elemental pressure midplane for the original grid (marked "1 ×") and a grid with double the number of cells in each direction (marked "2 ×").
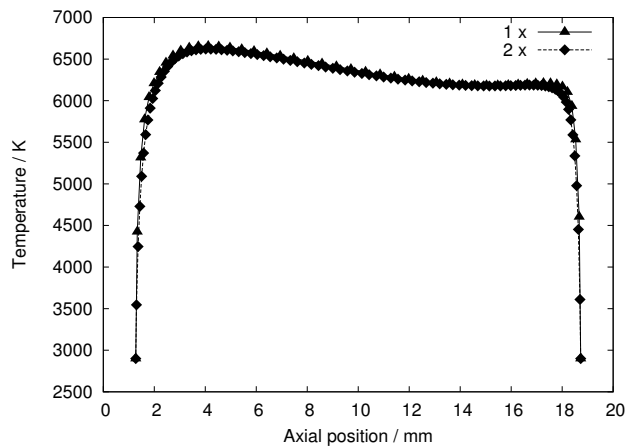
Figure 7.20: Temperature along the axis for the original grid (marked "1 ×") and a grid with double the number of cells in each direction (marked "2 ×").
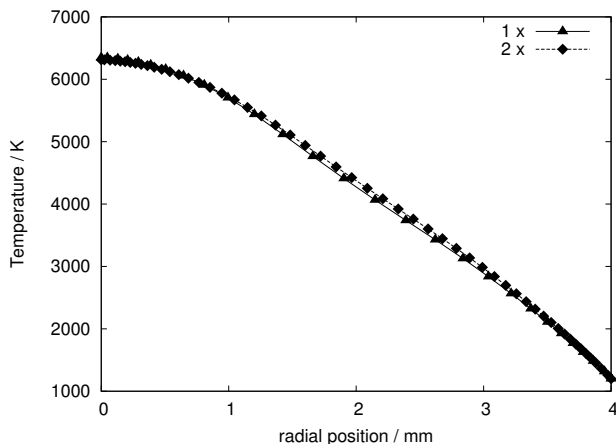
Figure 7.21: Temperature midplane for the original grid (marked "1 ×") and a grid with double the number of cells in each direction (marked "2 ×").

resolve the large gradients near the bottom electrode resulting in overshoot and slightly lower values between 4 mm and 10 mm from the bottom electrode. A similar overshoot is witnessed in figure 7.19 where the coarse grid does not resolve the steep transition between atoms and molecules as well as the finer grid. The differences are small, however and do not alter the conclusions drawn in this chapter. The effect on the temperature is smaller yet, as shown in figures 7.20 and 7.21 which show the temperature along the axis and midplane between the electrodes, respectively.

7.5 Conclusions

A metal halide lamp with the COST geometry has been placed in a centrifuge to study the effect of the competition between convection and diffusion on the distribution of additives in the lamp. Using the plasma modelling platform Plasimo, we have simulated the same lamp under different accelerational conditions. The density of dysprosium atoms in the ground state has been measured using the ILAS technique for different lamp fillings and accelerational conditions. These ground state densities show good qualitative agreement with the dysprosium atom densities predicted by the model.

The quantitative agreement between the model and experiments are not as good. One possible reason is the cold spot vapour pressure of the elements. This cold spot vapour pressure depends exponentially on the cold spot temperature. Increasing the temperature by 10 K is enough to raise the vapour pressure 30%. Using a vapour pressure of 150 Pa rather than the value of 517 Pa measured by X-Ray Fluorescence (XRF) by Nimalasuriya et al [21] on similar lamps yields a better quantitative match between model and experiment.

The study with different vapour pressures also gives insight into the effects of the radiation emitted by the dysprosium additives. Increasing the partial pressure of dysprosium atoms and ions increases the radiation emitted by these species. Most of this radiation is emitted just off-centre from the axis. The radiative cooling by dysprosium causes the arc to contract. Increasing the amount of dysprosium in the discharge increases arc contraction.

The competition between convection and diffusion can be understood quantitatively by introducing a Peclet number defined as the ratio between the rate of radial diffusion and axial convection. A Peclet number of unity leads to the greatest axial segregation. Increasing the convection speed by increasing the acceleration changes the radial profiles from a step like profile to a more erratic profile with local minima and maxima. Obtaining a homogeneous distribution of additives in the lamp can be achieved by designing a lamp such that the Peclet number is much greater or much smaller than unity.

Chapter 8

Convection in MH Lamps

8.1   Introduction

In earlier chapters the competition between convection and diffusion in metal halide lamps was studied through numerical modelling. In chapter 4 a simple scaling law was found that can predict the conditions for which the lamp is most strongly demixed. This simple scaling law relates the average segregation depth τ with the Peclet Pe number. The Peclet number is given by the ratio of the axial convection and radial diffusion rates. In terms of the effective diffusion coefficient of the element D_α and the axial convection speed V_z it is equal to:

$$Pe = \frac{R^2 V_z}{L D_\alpha},\tag{8.1}$$

with L the length and R the radius of the lamp. In this chapter a simple model will be derived to estimate V_z. This simple model will be compared with the results of the more self-consistent numerical models presented in previous chapters.

8.2   A simple flow model

In this section a basic scaling law for the convection of metal halide lamps will be derived from the Navier Stokes equation and a greatly simplified energy balance. The approach is similar to Elenbaas [64], but with the emphasis on deriving an

analytical expression. Elenbaas used a graphical method to get a more accurate estimation of the convection speed in high pressure mercury lamps.

Let us examine a cylinder with a large aspect ratio filled with an inert gas. The walls of the cylinder are held at a fixed temperature T_w. The effect of ohmic heating is modelled with a uniform heat source S. A schematic representation of the lamp is given in figure 8.1.
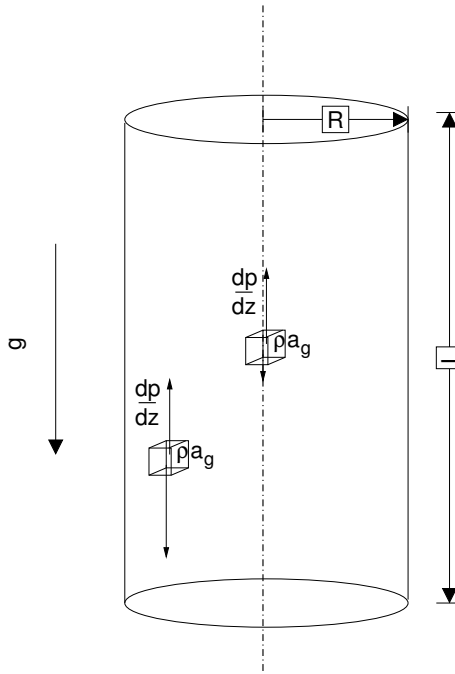
Figure 8.1: The simplified geometry used to examine convection in the lamp. The forces due to gravity and the pressure gradient on a volume element on the axis and close to the walls are shown with arrows. Close to the walls the density is greater and the net force is directed towards the bottom of the lamp. In the centre the pressure gradient is identical but the density is much lower and the net force is directed toward the top of the lamp.

The walls of MH lamps need to be relatively cool to avoid damage. For MH lamps with quartz walls this means a temperature of approximately 1200 K, ce-

ramic MH lamps can sustain temperatures of 1500 K. The centre of the discharge must be hot enough to excite the light emitting species and partially ionise the gas. In practice the temperature in the centre is approximately 6000 K.

The temperature difference between the hot centre and colder walls will cause a density difference, with the centre of the discharge being less dens than the gas near the wall. This density difference gives rise, under the influence of gravity, to a buoyancy force. This buoyancy force, in turn, is balanced by viscous forces and drives the convection flow.

8.2.1 The temperature profile

In this subsection a simple approximation for the temperature profile is sought. The effects of radiation, chemistry and non uniform power input will be ignored in order to arrive at an analytical expression. Neglecting the influence of convection on the temperature balance one may write:

$$-\frac{1}{r}\frac{\partial}{\partial r}\left(r\lambda\frac{\partial T}{\partial r}\right) = S,$$

where λ is the heat conductivity. As stated before, we assume the heat source S is uniform and independent of the temperature. Solving the equation under the boundary conditions that $T(R) = T_w$ and using $r\left.\frac{dT}{dr}\right|_{r=0} = 0$ yields:

$$T = T_w + \hat{T}\left(1 - \left(\frac{r}{R}\right)^2\right), \tag{8.2}$$

with $\hat{T} = SR^2/4\lambda$.

8.2.2 Velocity

The Navier Stokes equation for the gas in the cylinder is given by:

$$\frac{\partial \rho \vec{u}}{\partial t} + (\rho \vec{u} \cdot \nabla)\,\vec{u} = -\nabla p + \nabla \cdot (\mu \nabla \vec{u}) + \rho \vec{a}_g, \tag{8.3}$$

with ρ the density, $\vec{u}$ the velocity, t the time, p the pressure, μ the dynamic viscosity and $\vec{a}_g$ the gravitational acceleration.

As the aspect ratio of the cylinder is large, a number of simplifications are possible. Away from the ends, the temperature depends solely on the radial position ($T = T(r)$). The velocity through the midplane is axially directed and also solely radially dependent ($\vec{u} = u(r)\vec{e}_z$). The time dependency is ignored

as we are looking for a stationary solution. It is also assumed that the viscous forces are much larger than the inertial forces (the Reynolds number is low). To further simplify the equations constant viscosity is assumed.

Using the above simplifications the Navier Stokes equation reduces to:

$$\frac{\partial p}{\partial z} = \frac{1}{r}\frac{\partial}{\partial r}\left(\mu r \frac{\partial u}{\partial r}\right) - \rho a_g, \tag{8.4}$$

$$\frac{\partial p}{\partial r} = 0 \text{ and} \tag{8.5}$$

$$\frac{\partial p}{\partial \phi} = 0. \tag{8.6}$$

The equation above shows that the pressure is independent of the radial and azimuthal position. If the aspect ratio is large enough, the pressure gradient will also be independent of the axial position.

The equation above is made dimensionless by introducing a dimensionless position $x = r/R$, the dimensionless density $\rho^* = \rho/\rho_0$, with ρ_0 the density in the centre, and the dimensionless velocity u^* given by

$$u^* = \frac{\mu}{\rho_0 a_g R^2} u. \tag{8.7}$$

Equation (8.4) then becomes

$$\frac{1}{x}\frac{d}{dx}\left(x\frac{du^*}{dx}\right) = \rho^* + A, \tag{8.8}$$

with A the dimensionless pressure gradient,

$$A = \frac{1}{\rho_0 a_g}\frac{dp}{dz}. \tag{8.9}$$

By integration we obtain:

$$x\frac{du^*}{dx} = \int_0^x \rho^* x' dx' + \frac{1}{2}Ax^2 + C_1,$$

with $C_1 = 0$ since $x\frac{du^*}{dx} = 0$ for $x = 0$. Integrating a second time yields:

$$u^*(x) = \int_0^x \frac{1}{x'}\left(\int_0^{x'} x''\rho^* dx''\right) dx' + \frac{1}{4}Ax^2 + u_0, \tag{8.10}$$

with u_0 the convection speed on the axis to be determined by the boundary conditions. As the lamp is closed the net flux through the midplane must be zero ($\int_0^R \rho(r)u(r)rdr = 0$). This condition will be used to find the parameter A.

Substitution of the temperature profile

With the temperature profile found in the previous section one can now evaluate the integral in equation (8.10). With the use of the ideal gas law and 8.2 one may obtain:

$$\rho^* = \left(1 - x^2 \hat{T}/T_0\right)^{-1},\tag{8.11}$$

with T_0 the temperature on the axis. Substitution into (8.10) results in:

$$u^*(x) = u_0 + \frac{1}{4}Ax^2 + Li_2\left((\hat{T}/T_0)x^2\right),\tag{8.12}$$

with $Li_2(x)$ the dilogarithm:

$$Li_2(x) = \int_x^0 \frac{\ln(1-y)}{y}dy.\tag{8.13}$$

Using the no-slip condition on the wall ($u^*(1) = 0$) one may derive:

$$u^*(x) = \frac{1}{4}A(x^2 - 1) + Li_2\left((\hat{T}/T_0)x^2\right) - Li_2\left(\hat{T}/T_0\right).\tag{8.14}$$

To obtain the value of A that satisfies $\int_0^R \rho(r)u(r)rdr = 0$ a numerical technique is required. Using the Levenberg-Marquand algorithm the value for A has been calculated for different ratios of $\hat{T}/T_0$. The result is shown in figure 8.2. A typical MH lamp has a ratio $\hat{T}/T_0$ between 0.7 and 0.8 resulting in a value of $A \approx -20$. From this result the dimensionless velocity $u^*(x)$ may be calculated. An example is shown in figure 8.3. Note that this dimensionless velocity depends only on the ratio $\hat{T}/T_0$.

8.2.3 Comparison with grand numerical model results

The velocity predicted by the simple flow model with a near analytical result may now be compared with the more complex, two dimensional model with a non-constant viscosity. Such a comparison is shown in figure 8.4, for a lamp with a mercury pressure of 10 bar, a central temperature of 6000 K, and a wall temperature of 1200 K. In the numerical model the viscosity has been calculated by Wilke's formula [36]. For comparison, a viscosity of 4×10^{-4}Pas has been chosen in the analytical expression. The velocity predicted by the analytical expression is greater in magnitude than that predicted by the more complex numerical model. The profile is remarkably similar, however.
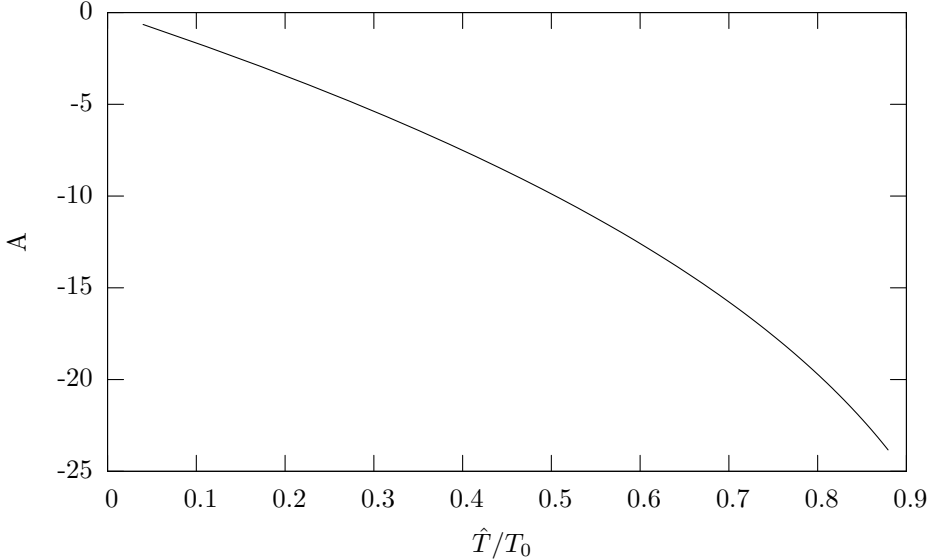
Figure 8.2: Value of A so that the equation $\int_0^R \rho(r)u(r)r\,dr = 0$ is satisfied. Typical MH lamps have a ratio $\hat{T}/T_0$ between 0.7 and 0.8.

To obtain an analytical expression a constant viscosity has been assumed. The viscosity is, however, anything but constant, as is shown in figure 8.5. Furthermore, an infinite aspect ratio has been assumed. In reality the aspect ratio of the lamp under study is only 5. To get a better estimate the non-constant viscosity needs to be taken into account. To correct for the smaller aspect ratios a two dimensional model is required. In either case, the convection flow can only be solved numerically.

We may, however, use the scaling parameter in (8.7) to find a scaling law for discharges with a similar temperature profile. The dimensionless velocity $u*$ only depends on the ratio $\hat{T}/T_0$. For discharges with the same temperature profile we have:

$$u \propto \frac{\rho_0 a_g R^2}{\mu}. \tag{8.15}$$

Thus the velocity is

- proportional to the square of the radius,
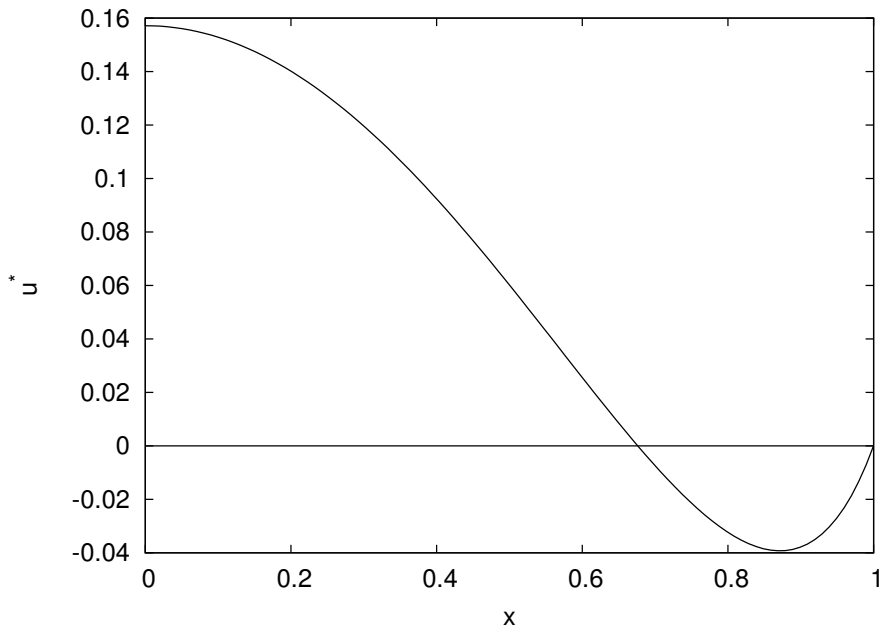
Figure 8.3: The dimensionless velocity u^* for $\hat{T}/T_0 = 0.8$.

- proportional to the density at the centre,

- proportional to the gravitational acceleration and

- inversely proportional to the viscosity.

Using the ideal gas law one may rewrite this as

$$u \propto \frac{m_{Hg}pa_gR^2}{\mu kT_0},\qquad(8.16)$$

with m_{Hg} the mass of the mercury atom. Thus the velocity also increases linearly with the total pressure. In the next two sections the validity of these scaling laws will be examined using the results from more complex numerical models. In particular the dependance an the pressure, the radius and the gravitational acceleration are examined.
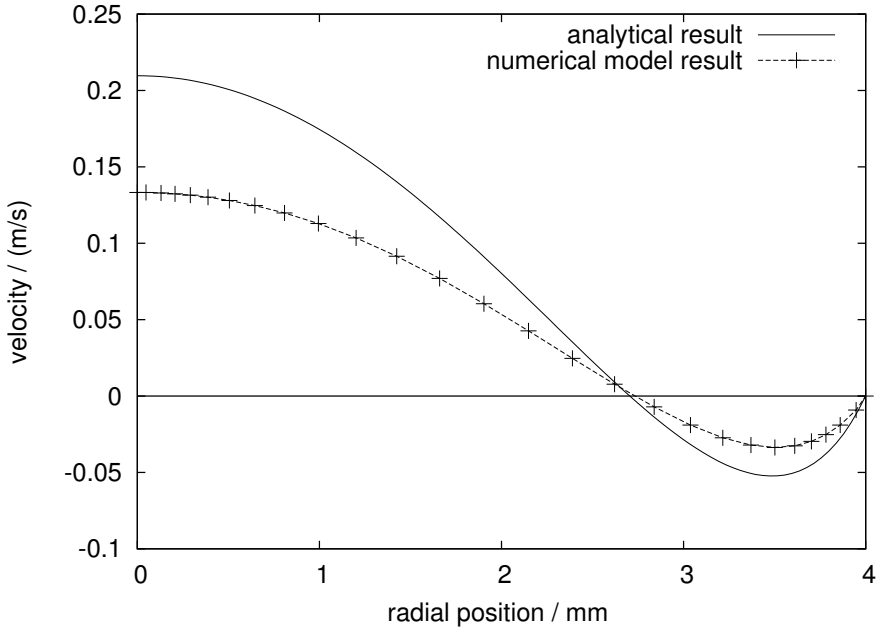
Figure 8.4: Axial velocity as calculated from (8.10) compared with results from the MH lamp model. To get the velocity from the analytical model a value of 4×10^{-4}Pas has been chosen for the viscosity.

8.3   Mercury lamp

The additives in MH lamps significantly improve the colour rendering of these devices as compared with lamps containing pure mercury. The impact on the convection patterns is much smaller and indirect. We examine the convection with numerical experiments of a lamp containing pure mercury. The model of this lamp is identical to the model for the mercury lamp described in chapter 4. The total pressure is varied by increasing the lamp filling.

Equation (8.16) predicts a linear relationship between the velocity and the pressure. The assumptions of a uniform power input is not valid in lamps of this type as most of the power is deposited on the axis close to the electrodes. The viscosity and thermal conductivity are also temperature dependent. The temperature profiles are also effected by the pressure. Nevertheless, as figure
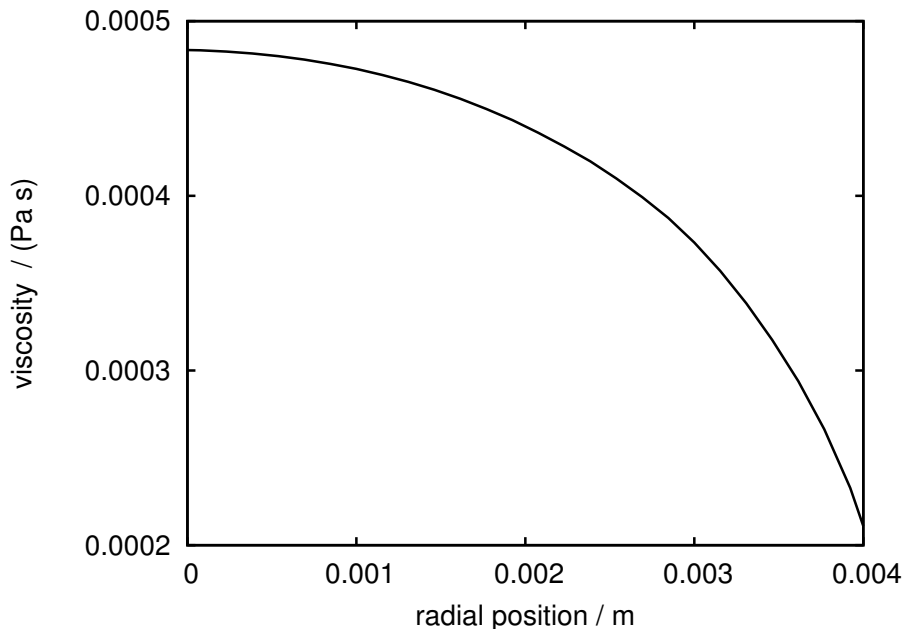
Figure 8.5: Viscosity from the MH lamp model calculated by the Wilke formula [36].

8.6 shows, the velocity does show a linear dependence on the pressure.

The dependence on the square of the radius has also been investigated by examining two lamps with the same volume and input power but with two different radii: 2 mm and 4 mm respectively (with lengths of 80 mm and 20 mm). According to (8.16) the velocity should increase with the square of the radius. The dimensionless velocity u^* should be independent of the radius and the total lamp pressure. Figure 8.7 shows the dimensionless velocity midplane on the axis as a function of the pressure for models of lamps with a radius of 2 mm and 4 mm compared. The lamp with the longer aspect ratio has a greater dimensionless velocity. There is also a weak dependence on the pressure.
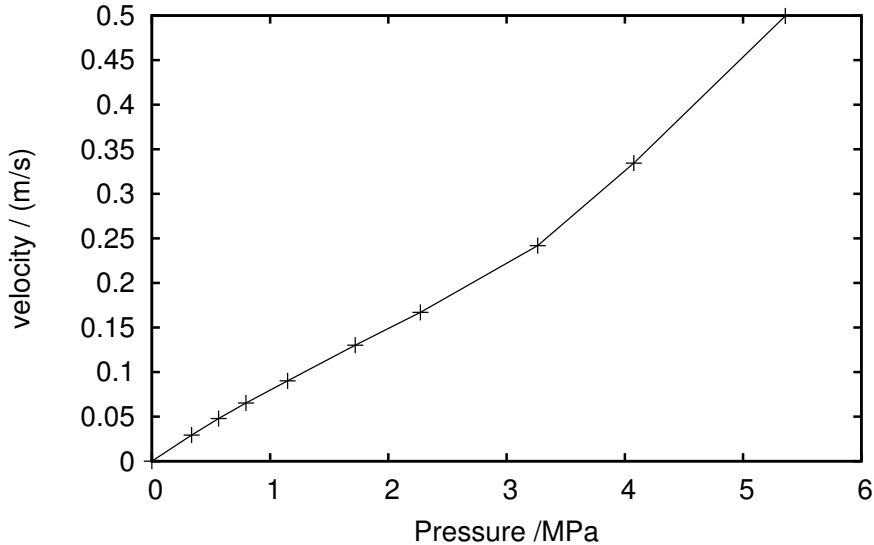
Figure 8.6: The axial velocity on the axis halfway between the electrodes in a pure mercury lamp for different pressures corresponding to lamp fillings between 3 mg and 60 mg.

8.4   Metal halide lamp

We examined the velocity on the axis halfway between the electrodes as calculated by the metal halide lamp model in chapter 7. To compare with results of experiments in a centrifuge we used different values for a_g ranging from 1 g to 10 g. The model was also run with different lamp fillings from 3 mg to 20 mg. The simple flow model derived earlier predicts a linear dependence on the product of the pressure and the acceleration a_g. Figure 8.8 shows that such a linear dependence is a good approximation. This in spite of the non-constant power input, changing temperature profiles for different pressures and the dependence of the viscosity and thermal conductivity on the temperature.
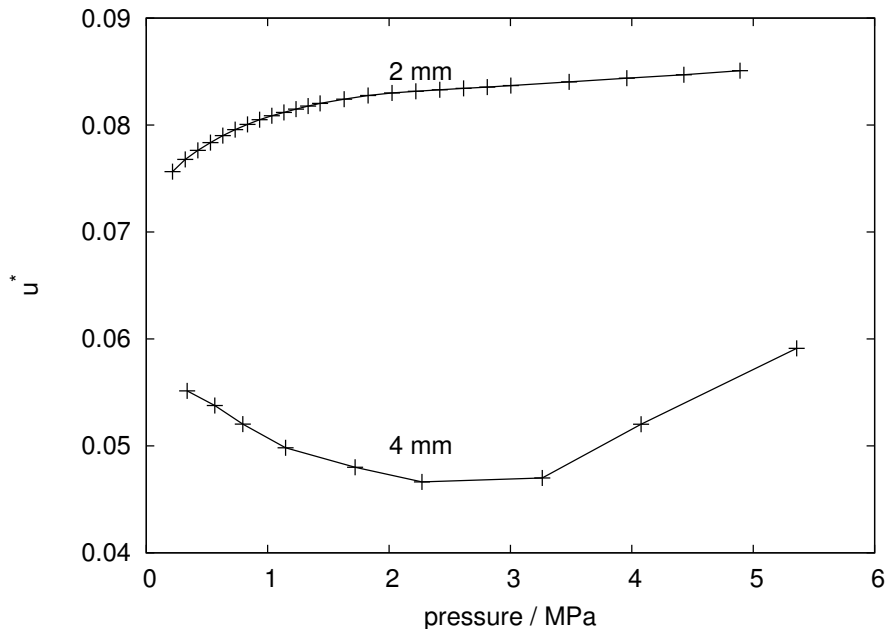
Figure 8.7: The dimensionless axial velocity in a pure mercury lamp. Results are shown for different pressures corresponding to lamp fillings between 3 mg and 60 mg and lamp radius of 2 mm and 4 mm compared. According to (8.16) one would expect a single horizontal line in this graph.

8.5 Conclusion and discussion

A simple semi-analytical expression has been derived for the axial velocity in a metal halide lamp. The derivation is not completely analytical as one of the parameters needs to be determined numerically. This numerical procedure however, is much less time-consuming than the full numerical models consisting of many coupled non-linear differential equations, ray-tracing and the determination of the chemical equilibrium via Gibbs minimisation. Furthermore, this parameter A, representing the dimensionless pressure gradient, depends only on the temperature difference between the centre and the wall of the discharge. Comparing the velocity with full numerical model results shows, however, that it gives only a rough approximation of the axial velocity.
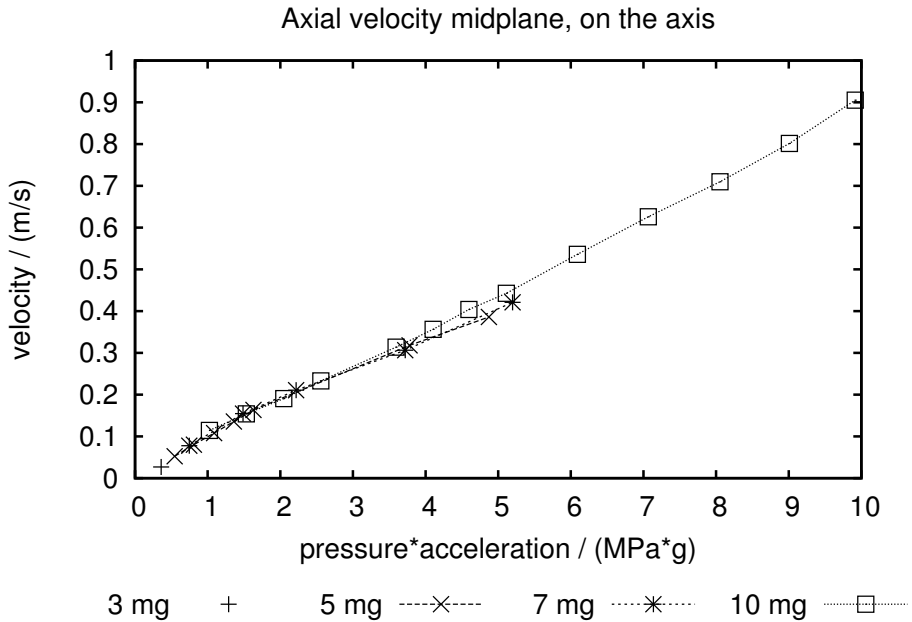
Figure 8.8: The axial velocity on the axis halfway between the electrodes for different lamp fillings under different accelerational conditions.

   The scaling law derived is more useful, it shows a linear dependence of the axial velocity on the pressure. Looking at the results from numerical models of a pure high pressure mercury lamp and a metal halide lamp shows that this is indeed a good approximation. The dependence on the gravitational acceleration has also been examined. This is of interest for the estimation of the axial velocity in experiments conducted in a centrifuge, such as those in chapter 7. Results from the metal halide lamp modelled in this chapter show that the predicted linear relationship between the gravitational acceleration and the axial convection holds to good approximation. The scaling law also predicts that the velocity is proportional to the square of the radius of the discharge. This scaling law does not hold if the aspect ratio is also changed, as demonstrated by a numerical model of a pure mercury discharge.

Chapter 9

General conclusion

The plasma simulation platform PLASIMO has been used to develop a numerical model of the additive distribution in vertically burning metal halide lamps. The model assumes axial symmetry, a steady laminar flow and the presence of LTE. Two different transport modes were used. The balances of mass, momentum and energy and the conservation of elements were solved using the control volume approach, the radiation transport is treated by means of ray tracing. The input of this model is the set of control parameters, such as the fill chemistry, driving power and vessel shape. The output is formed by plasma properties; such as the voltage over the lamp electrodes, the production of heat and the emission of radiation. Along the way many more plasma properties are calculated: the distribution of the elements over the lamp and the fields of the temperature, the velocities and the pressure. The model attempts to calculate these parameters in a self consistent manner from first principles. There is no place for fudge parameters. At the same time the model must be as simple as possible; approximations that can be made should be made.

Using this model numerical simulations have been performed of lamps containing mercury with sodium iodide and dysprosium iodide (Na and Dy lamps). Initial studies were carried with Na as the simulation of the Na lamps is relatively easy. The chemistry is rather simple and only a few Na lines have to be taken into account in the ray tracing procedure. The modelling of the Dy lamp is more complicated; a proper chemical description needs to include more species and an enormous number of radiative transitions have to be dealt with. There was no choice, however; we had to construct a model for the Dy lamp since the experimental validation of a Na lamp is not easy.

The central aim of the numerical studies was to come to a basic understanding of the transport of additives in MH lamps. To this end model calculations were done for many different conditions, that is to say, for different pressures, accelerations and chemical compositions. Additionally, the studies were carried out on the influence of the cold spot vapour pressure, the elastic scattering cross section between dysprosium ions and mercury atoms and the choice of data set for the transition probabilities of dysprosium atoms and ions. Results from these calculations were classified by looking at the output; in particular at the distribution of additives, the temperature, the velocity and the density of the radiative species. The main results can be classified by the introduction of two dimensionless parameters: the segregation depth of the lamp τ and the Pe number. Together these describe the axial segregation in the lamp.

9.1   Axial segregation

Axial segregation was shown to be the result of the competition between axial convection and radial diffusion. This competition is best expressed by the dimensionless Peclet number. When the Peclet number is approximately equal to unity axial segregation is strongest. The degree of axial segregation is best expressed by the dimensionless segregation depth τ. The largest value of τ depends on the element under study and on the position in the discharge where the molecules dissociate to form ions. This position, in turn, depends on the temperature profile and on the dissociation energy of the molecule.

The Peclet number depends on the diffusion coefficient, the lamp geometry and the axial convection speed. The diffusion coefficient can be estimated from the total lamp pressure and the elastic cross sections of the additives with the background mercury gas. In chapter 8 a scaling law was derived for the dependence of the convection on the pressure and (in the case of a centrifuge) on the accelerational conditions. It was shown that the convection depends linearly on the pressure and the acceleration. The convection speed also depends on the density gradients, and is thereby related to the temperature profile.

9.2   Temperature profile

In chapter 4 it was found that adding dysprosium to the discharge causes the temperature profile to contract. The temperature along the flanks is decreased, when compared to a pure mercury discharge, by radiation from dysprosium

atoms. To still allow the same ohmic dissipation the temperature along the axis has to increase. This arc contraction is in agreement with experimental results found in X-Ray absorption measurements [65]. In chapter 5 it was found that the degree of contraction predicted by the model depends on the choice of data set for the transition probabilities. In chapter 7 it was also found that the cold spot vapour pressure directly influences the degree of contraction. The sodium discharges have a lower temperature along the axis due to the lower ionisation potential. Additionally, sodium has a number of optically thick lines which heat up the edges of the discharge. Dysprosium has a spectral grass field of lines, most of which are optically open. In chapter 5 it was found that, for the purpose of calculating the temperature profile, the spectral grass field can be approximated by two effective transitions.

9.3 Comparison with experiments

The results of the model for the Dy lamp were compared to that of experiments. In chapter 6 we dealt with microgravity conditions whereas chapter 7 was devoted to lamps in a centrifuge. Both studies show that the model is capable to predict main trends. However, precise quantitative agreement can only be obtained if experimental techniques are available that make it possible to determine the cold spot temperature with high precision. This temperature is very important in the determination of the vapour pressure of the Dy containing molecules above the salt pool and thus for the number of Dy containing components that enter the plasma phase.

Better input data is also needed for the elastic scattering cross sections between the Dy containing species and the mercury atoms which vastly outnumber all other species. In chapter 6 the influence of the choice of elastic scattering cross sections between dysprosium ions and the background mercury gas was studied. The ratios of dysprosium to mercury ions in the centre of the discharge appeared particularly sensitive to the choice of cross section. Thus, measuring this ratio could help to validate elastic scattering cross section data. The measurements would have to be performed in lamps with low convection speeds. A low cost alternative to taking lamps to the international space station would be to use lamps with a long aspect ratio and relatively small mercury dosings (approximately 5 mg for a lamp equal in volume to the COST reference lamp). As is shown in chapter 8 such conditions would also lead to low Peclet numbers.

9.4 Outlook

To keep both the model and the experiments as simple as possible only lamps with a single salt additive have been considered. Commercial lamps typically have more additives. The model that has been developed alows for more than one salt additive, however. The number of additives is limited only by the amount of computer memory required for the look-up table with the species densities as a function of the elemental abundance, temperature and pressure. Currently, these lookup tables are around 28 MiB in size. Adding one or two more additives lies well within the possibilities. Adding as many as six different additives to fully simulate the mixture in a commercial lamp would require an overhaul of the look-up tables from the current linear interpolation scheme to a smarter interpolation scheme. Studying mixtures with two or three additives would also be of interest to study the effect of additives on each other.

A related topic that is of utmost interest is how the combination of radiative cooling and the association/dissociation position will facilitates instabilities. Due to radiative contraction the wall stabilisation will be lost. Moreover self-generated magnetic fields might be able to excite helical instabilities. The helical instabilities would require a full three-dimensional time dependent model. Other types of instabilities that can be present are those initiated by acoustic resonances. These also require a time dependent model. There are certainly plenty of challenges left in the study of metal halide lamps.

Bibliography

[1] M. Gendre. Two centuries of electric light source innovations. available online: http://www.einlightred.tue.nl/lightsources/history/.

[2] P. Flesch, editor. *Light and Light Sources, High-Intensity Discharge Lamps.* Springer, Berlin, 2006.

[3] C. P. Steinmetz. Us patent no. 1025932 means for producing light, 1902.

[4] A. D. Jackson, III R. G. Gibson, S. A. Carleton, S. Wu, L. N. Kowalczyk, T. Steere J. J. Palmer, J. C. Alderman, Sr. J. E. Conrad, and K. L. Collins. United states patent 6833677 150w-1000w mastercolor ceramic metal halide lamp series with color, 2004.

[5] E. Fisher. Axial segregation of additives in mercury-metal-halide arcs. *J. Appl. Phys.*, 47:2954, 1975.

[6] D. E. Work. Chemistry of metal halide lamps: a review. *Light. Res. Tech.*, 13:143, 1987.

[7] J. T. Dakin, Jr. T. H. Rautenberg, and E. M. Goldfield. Anatomy of a vertical metal halide discharge. *J. Appl. Phys.*, 66:4074–4088, 1989.

[8] R. J. Zollweg. Reducing additive segregation in metal halide high-intensity discharge lamps. *J.I.E.S*, 4:12–18, 1975.

[9] W. W. Stoffels, A. H. F. M. Baede, J. J. A. M. van der Mullen, M. Haverlag, and G. Zissis. Definition of a high intensity metal halide discharge reference lamp. *Meas. Sci. Technol.*, 17:N67–N70, 2006.

[10] M. Käning, B. Schalk, and H. Schneidenbach. Experimental determination of parameters for molecular continuum radiation of rare-earth iodides. *J. Phys. D: Appl. Phys.*", 40:3815–3822, 2007.

[11] T. Nimalasuriya, N. B. M. Pupat, A. J. Flikweert, W. W. Stoffels, M. Haverlag, and J. J. A. M. van der Mullen. Optical emission spectroscopy of metal-halide lamps: Radially resolved atomic state distribution functions of dy and hg. *Journal of Applied Physics*, 99:053302, 2006.

[12] T. Nimalasuriya, A. J. Flikweert, M. Haverlag, P. C. M. Kemps, G. M. W. Kroesen, W. W. Stoffels, and J. J. A. M. van der Mullen. Metal halide lamps in the international space station ISS. *J. Phys. D*, 39:2993–3001, 2006.

[13] A. J. Flikweert, T. Nimalasuriya, G. M. W. Kroesen, and W. W. Stoffels. Imaging laser absorption spectroscopy of the metal-halide lamp in a centrifuge (1-10*g*). *Plasma Sources Sci. Technol.*, 16:606–613, 2007.

[14] T. Nimalasuriya, M. L. Beks, A. J. Flikweert, W. W. Stoffels, M. Haverlag, and J. J. A. M. van der Mullen. Metal-halide lamps in micro-gravity, experiment and model. *J. Phys. D: Appl. Phys."*, 2007. submitted.

[15] S. V. Patankar, editor. *Numerical Heat Transfer and Fluid Flow*. New York: McGraw-Hill, 1980.

[16] http://plasimo.phys.tue.nl/.

[17] M. S. Benilov and M. D. Cunha. Bifurcation points in the theory of axially symmetric arc cathodes. *Phys. Rev. E.*, 68(5):056407, Nov 2003.

[18] M. S. Benilov, M. D. Cunha, and G. V. Naidis. Modelling current transfer to cathodes in metal halide plasmas. *J. Phys. D: Appl. Phys."*, 38:3155–3162, 2005.

[19] T. Nimalasuriya, J. J. Curry, C. J. Sansonetti, E. J. Ridderhof, A. J. Flikweert, W. W. Stoffels, M. Haverlag, and J. J. A. M. van der Mullen. X-ray induced fluorescence measurement of the density distribution of Dy and Hg in a metal-halide lamp. *XXVIIth International Conference on Phenomena in Ionized Gases*, 2005.

[20] T. Nimalasuriya, G. M. Thubé, A. J. Flikweert, M. Haverlag, G. M. W. Kroesen, W. W. Stoffels, and J. J. A. M. van der Mullen. Axial segregation in metal-halide lamps under varying gravity conditions ranging from 1 to 10 g. *J. Phys. D*, 40:2839–2846, 2007.

[21] T. Nimalasuriya, J. J. Curry, C. J .Sansonetti, E. J. Ridderhof, S. D. Shastri, A. J. Flikweert, W. W. Stoffels, M. Haverlag, and J. J. A. M. van der Mullen. X-ray induced fluorescence measurement of segregation in a dyi$_3$-hg metal-halide lamp. *J. Phys. D*, 40:2831, 2007.

[22] A. J. Flikweert, M. van Kemenade, T. Nimalasuriya, M. Haverlag, G. M. W. Kroesen, and W. W. Stoffels. Axial segregation in metal halide lamps under varying conditions during parabolic flights. *J. Phys. D: Appl. Phys."*, 39:1599–1605, 2006.

[23] D. A. Larson, H. D. Fraser, W. V. Cushing, and M. C. Unglert. Higher efficiency light source through use of additives to mercury discharge. *Illuminating Engineering*, 58:434, 1963.

[24] M. Sugiura. Review of metal-halide discharge-lamp development 1980-1992. *Science, Measurement and Technology, IEE Proceedings A*, 140:443–449, 1993.

[25] G. G. Lister, J. E. Lawler, W. P. Lapatovich, and V. A. Godyak. The physics of discharge lamps. *Rev. Mod. Physics*, 76:542–598, 2004.

[26] S. Hashiguchi, K. Hatase, S. Mori, and Tachibana. Numerical simulation of metal-halide lamp using a time-dependent two-dimensional model. *J. Appl. Phys.*, 92:45–53, 2002.

[27] D.A. Benoy. *Modelling of thermal argon plasmas.* PhD thesis, Eindhoven University of Technology, The Netherlands, 1993.

[28] J. van Dijk. *Modelling of Plasma Light Sources — an object-oriented approach.* PhD thesis, Eindhoven University of Technology, The Netherlands, 2001.

[29] S. Chapman and T. G. Cowling, editors. *The Mathematical Theory of Non-Uniform Gases, 3rd ed.* Cambridge University Press, 1974.

[30] J. O. Hirschfelder, C. F. Curtiss, and R. B. Bird, editors. *Molecular Theory of Gases and Liquids.* (New York: Wiley & Sons), 1964.

[31] H. van der Heijden. *Modelling of Radiative Transfer in Light Sources.* PhD thesis, Eindhoven University of Technology, The Netherlands, 2003.

[32] A. Hartgers, H. W. P. van der Heijden, M. L. Beks, J. van Dijk, and J. A. M. van der Mullen. An elemental diffusion description for LTE plasma models. *J. Phys. D: Appl. Phys.*, 38(18):3422–3429, 2005.

[33] M. Mitchner and C. H. Kruger, editors. *Partially Ionized Gases.* (New York: Wiley & Sons), 1973.

[34] C. W. Johnston. *Transport and equilibrium in molecular plasmas - the sulfur lamp.* PhD thesis, Eindhoven University of Technology, The Netherlands, 2003.

[35] J. N. Butler and R. S. Brokaw. Thermal conductivity of gas mixtures in chemical equilibrium. *J. Chem. Phys.*, 26(6):1636, 1956.

[36] C. R. Wilke. A viscosity equation for gas mixtures. *J. Chem. Phys.*, 18:517–519, 1950.

[37] S. Paolucci. The differentially heated cavity. *Sadhana*, 19:619–647, 1994.

[38] H. G. Hülsman and J. Mentel. The helical magnetic instability of arcs in an axial magnetic field treated by a linear time dependent theory. *Phys. Fluids*, 30:2266–2273, 1987.

[39] W. W. Stoffels, F. van den Hout, G. M. W. Kroesen, M. Haverlag, and R. Keiser. Helical instabilities in metal halide lamps under micro and hyper-gravity conditions. *App. Phys. Lett.*, 88:091502, 2006.

[40] M. L. Beks, A. Hartgers, and J. J. A. M. van der Mullen. Demixing in a metal halide lamp, results from modelling. *J. Phys. D: Appl. Phys.*, 39:4407, 2006.

[41] H. van der Heijden and J. J. A. M. van der Mullen. General treatment of the interplay between fluid and radiative transport phenomena in symmetric plasmas: the sulfur lamp as a case study. *J. Phys. D: Appl. Phys."*, 35:2112–2125, 2002.

[42] C. W. Johnston, H. van der Heijden, G. Janssen, J. van Dijk, and J.A.M. van der Mullen. A self consistent lte model of microwave driven high pressure sulfur lamp. *J. Phys. D: Appl. Phys."*, 35:342–351, 2002.

[43] Private communications a.h.f.m. baede.

[44] M. E. Wickliffe, J. E. Lawler, and G. Nave. Atomic transition probabilities for dy i and dy ii. *J. Quant. Spectrosc. Radiat. Trans.*, 66:363–404, 2000.

[45] W. G. Vincenti and C. H. Kruger Jr. *Introduction to Physical Gas Dynamics*. John Wiley and Sons, Inc., 1965.

[46] M. Čenskýa, L. Hnědkovskýa, and V. Majerb. Heat capacities of aqueous polar aromatic compounds over a wide range of conditions. part i: phenol, cresols, aniline, and toluidines. *Journal of Chemical Thermodynamics*, 37:205–219, 2005.

[47] W. R. Smith and R. W. Missen. *Chemical Reaction Equilibrium Analysis: Theory and Algorithms*. Krieger publishing company, 1991.

[48] C. W. Bale, P. Chartrand, S. A. Degterov, G. Eriksson, K. Hack, R. Ben Mahfoud, J. Melonçon, A. D.Pelton, and S. Peterson. CALPHAD, 26:189–228, 2002.

[49] http://gttserv.lth.rwth-aachen.de/ cg/software/chemapp/cal-doc/cal84.html.

[50] S. Chandrasekhar. *Radiative transfer*. Dover Publications Inc. New York, 1960. Revised edition.

[51] N. V. Gorschkov, V. A. Komarovski, A. L. Osherovich, N. P. Penkin, and R. Khefferlin. *Opt. Spectrosc.*, 48:362–4, 1980. data availabe online from the Harvard Smithsonian Center for Astrophysics Kurucz Atomic Line Database http://cfa-www.harvard.edu/amdata/ampdata/kurucz23/sekur.html.

[52] J. Waymouth. *Electric discharge lamps*. MIT press, Cambridge, 1971.

[53] J. R. Coaton and A. M. Marsden. *Lamps and Lighting 4th edition*. Arnold, London, 1997.

[54] X. Zhu. *Active spectroscopy on HID lamps, Exploration of various methods*. PhD thesis, Eindhoven University of Technology, The Netherlands, 2005.

[55] A. J. Flikweert, T. Nimalasuriya, C. H. J. M. Groothuis, G. M. W. Kroesen, and W. W. Stoffels. Axial segregation in high intensity discharge lamps measured by laser absorption spectroscopy. *Journal of Applied Physics*, 98:073301, 2005.

[56] M. L. Beks, J. van Dijk, A. Hartgers, and J. J. A. M. van der Mullen. A study on the effects of geometry on demixing in metal halide lamps. *IEEE Transactions on Plasma Science*, Volume: 35:1335–1340, 2007.

[57] S. D. Rockwood. *Phys. Rev. A*, 8:2348–58, 1973.

[58] C. L. Chen and M. Raether. *Phys. Rev.*, 128:2679, 1962.

[59] J. J. A. M. van der Mullen. *Phys. Rep.*, 191:109, 1990.

[60] J. de Groot and J. van Vliet, editors. *The high pressure sodium lamp*. Philips technical library, kluwer technische boeken, Deventer, Antwerpen, 1986.

[61] W. W. Stoffels, P. C. M. Kemps, J. Beckers, G. M. W. Kroesen, and M. Haverlag. Light emission of metal halide lamps under micro- and hypergravity conditions. *Appl. Phys. Lett.*, 87:241501, 2005.

[62] W. W. Stoffels, A. J. Flikweert, T. Nimalasuriya, J. J. A. M. van der Mullen, G. M. W. Kroesen, and M. Haverlag. Metal Halide Lamps: gravitational influence on color separation. *Pure Appl. Chem.*, 78:1239–1252, 2006.

[63] M. van Kemenade. Axial segregation in high intensity discharge lamps. Master's thesis, Eindhoven University of Technology, 2004.

[64] W. Elenbaas, editor. *The High Presure Mercury Vapour Discharge*. North Holland Publishing Company, Amsterdam, 1951.

[65] T. Nimalasuriya et al. to be submitted. *J. Phys. D: Appl. Phys."*, 2008.

Dankwoord

Bijna zes jaar geleden kwam ik bij Eddie van Veldhuizen op de kamer op zoek naar een afstudeeropdracht. Deze bracht mij in contact met Joost van der Mullen die mij verder introduceerde bij de groep EPG (Elementaire Processen in Gasontladingen) en het Plasimo team. Tijdens mijn afstuderen vroeg Joost van der Mullen of ik wou blijven om te promoveren. Dit wou ik, en na mijn afstuderen ging ik gelijk aan de slag. Niet aan lage druk extreem ultraviolet bronnen zoals tijdens mijn afstudeeronderzoek maar aan een lampje dat gewoon zichtbaar licht uitstraalt. Dat met een lampje interessante wetenschap valt te bedrijven heb ik de afgelopen vier jaar wel ondervonden. Ik dank dan ook mijn promotor en begeleider Joost van der Mullen van harte voor de ondersteuning en de inspiratie die nodig waren om tot dit proefschrift te komen.

Dat lampjes een interessant onderwerp voor wetenschappelijk onderzoek zijn was natuurlijk al langer bekend bij mijn tweede promotor: Marco Haverlag. Ik ben dan ook dankbaar voor zijn hulp en de discussies die ik met hem gevoerd heb. Ook wil ik mijn overige commissieleden bedanken voor hun nuttige bijdragen en correcties aan het proefschrift.

De numerieke modellen in dit proefschrift maken gebruik van het Plasimo platform, oorspronkelijk geschreven door Dany Benoy. Door vele bijdragen van afstudeerders en promovendi is deze code van een plasma simulatie model met twee toepassingen geëvolueerd in een simulatie platform met vele mogelijke toepassingen op plasma gebied. Ik ben daarbij in het bijzonder Jan van Dijk, Harm van der Heijden en Bart Hartgers dank verschuldigd. Jan van Dijk voor de algemene ondersteuning en ontwikkeling van Plasimo en Harm van der Heijden en Bart Hartgers voor de stralingscode. Bart Hartgers is ook in het begin stadium van mijn onderzoek zeer behulpzaam geweest in het aan de praat krijgen van modellen. Verder dank ik mijn voormalige kamer-genoot Bart Broks voor de nuttige discussies en Tanya Nimalasuriya en Arjan Flikweert voor de prettige samenwerking, met name in het tot stand komen van hoofdstukken 6 en 7. Ten-

slotte wil bedank ik mijn vriendin Kim Peerenboom voor het nakijken van mijn proefschrift en het geduld met mij in de weken voor mijn promotie.

Curriculum Vitae

Born October 2nd 1975 in Bellingwolde

Education

1992-1994 International Baccalaureate. First year at the International School of Kenya in Nairobi, Kenya second year at Rijnland's Lyceum in Oegstgeest, The Netherlands.

1994-2003 Master of Applied Physics at the Eindhoven University of Technology.

2004-2008 Ph.D. research in numerical plasma physics at the Eindhoven University of Technology.

Traineeships

April 1996 - December 1996 Internship with the Low Temperature Physics group of the faculty of applied physics under supervision of prof. dr. A. T. A. M. de Waele and ir. R.M.S. Knops. Title of the report: "Turbulentie bij een diameterovergang in de resonator van een thermo-akoestische koeler."

September 1999 - May 2000 Trainee with Fymaz and FEV in Aken (Germany). Under supervision of dr. ir. A.P.J. Voncken and dr. H.J.H. Clercx. Title of the report "Modeling Dynamically Loaded Cylindrical Bearings"

September 2002 - December 2003 Masters thesis at the group EPG of the faculty of applied physics (TUE). Supervisors: Dr. J.J.A.M. van der Mullen, ir. B.H.P. Broks and ir. W.J.M. Brok . Title of the report "Towards a Hybrid Fluid-Monte Carlo Model for Pulsed Hollow Cathode Discharges".

Experience

December 1996 - March 1998 Student tutor assisting with a practical class for mechanical engineering.

July 2000-July 2002 Modelling of the dynamic behaviour of electro magnetic valves for Fymaz in Stolberg (Germany).